

**LASER DEINSULATION OF PARYLENE-C
COATED UTAH ELECTRODE ARRAY**

by

Je-Min Yoo

A dissertation submitted to the faculty of
The University of Utah
in partial fulfillment of the requirements for the degree of

Doctor of Philosophy

Department of Electrical and Computer Engineering

The University of Utah

August 2013

Copyright © Je-Min Yoo 2013

All Rights Reserved

ABSTRACT

Implantable microelectrode arrays are biomedical devices used *in-vivo* serving as neural interfaces between the nervous system and external systems such as neuroprosthetics. They are designed to be chronically implanted in the central or peripheral nervous system and record or stimulate neural signals. The Utah electrode array (UEA) is a representative example of silicon-based neural interfaces. They are typically encapsulated with the USP Class VI biocompatible material, Parylene-C, on the inactive areas to insulate and encapsulate the electrodes and minimize damage to the neural tissue. In order to record or stimulate neural signals, the active electrode sites must be deinsulated. Tip deinsulation of Parylene-coated UEAs is typically performed by a reactive ion etching (RIE) process using an O₂ plasma, and an aluminum foil mask. This technique has limitations due to nonuniform tip exposure lengths contributing to large impedance variations ($\sigma > 0.5 \text{ M}\Omega$), and difficulty in controlling the magnitude of tip exposure, especially for tip exposures less than 40 μm , which are needed to increase its selectivity in recording or stimulating single or multiple neurons. Moreover, foil masks cannot be used for more complex electrode geometries, such as variable height electrodes.

In this work, excimer laser ablation of Parylene from a UEA using a tip metallization of iridium oxide (IrO_x) was investigated as an alternative deinsulation technique. A hybrid method of etching Parylene-C using a combination of laser ablation and the O₂ RIE was investigated in the efforts to minimize electrode damage and remove

carbonaceous residues. The median impedance for fine tip ($< 20 \mu\text{m}$) electrodes was $\sim 4.6 \text{ M}\Omega$ immediately after laser ablation. However, significant amounts of carbon residue on the exposed surface were removed, generating improved impedances to $\sim 0.7 \text{ M}\Omega$ by including a maskless RIE process using 1 minute O_2 RIE.

We also observed that reduction of IrO_x could occur at relatively mild ($> 180 \text{ }^\circ\text{C}$) temperatures in reducing ambients, resulting in dramatic changes to the structural and electrical properties of the tip metallization. The reduced IrO_x material was found to tolerate significantly more laser irradiation than the fully oxidized material. The median impedance, cathodal charge storage capacity (CSC_c), and charge injection capacity (CIC) for the reduced electrodes with $40 \mu\text{m}$ exposure were $\sim 25 \text{ k}\Omega$, $\sim 40 \text{ mC/cm}^2$, and $\sim 0.8 \text{ mC/cm}^2$, respectively. These results suggest that a hybrid laser ablation using an excimer laser and RIE is promising for deinsulation of UEAs.

To

My son, John
My wife, Hyun-Jin
&
My parents

TABLE OF CONTENTS

ABSTRACT.....	iii
LIST OF FIGURES.....	ix
ACKNOWLEDGMENTS.....	xiv
CHAPTERS	
1. INTRODUCTION.....	1
1.1 Neural Interfaces.....	1
1.2 Penetrating Silicon-Based Microelectrodes.....	2
1.3 Encapsulation and Tip Metallization Materials for Laser Deinsulation..	5
1.4 Hypothesis and Specific Aims.....	7
1.5 References.....	15
2. BACKGROUND AND STATE OF THE ART: TIP DEINSULATION AND HARGE INJECTION MATERIALS.....	20
2.1 Tip Deinsulation.....	20
2.1.1 Deinsulation Methods.....	20
2.1.2 Laser Beam Characteristics.....	21
2.1.3 Excimer Laser System.....	22
2.1.4 Laser Deinsulation.....	25
2.2 Electrochemistry of the Stimulating and Recording Microelectrode...	28
2.2.1 The Electrode-Electrolyte Interface.....	28
2.2.2 Double Layer Charging.....	29
2.2.3 Faradaic Charging.....	30
2.3 Electrochemical Characterization of Microelectrode.....	32
2.3.1 Cyclic Voltammetry.....	32
2.3.2 Electrochemical Impedance Spectroscopy.....	37
2.3.3 Potential Transient.....	39
2.4 Iridium Oxide as Electrode Material.....	41
2.4.1 Consideration in Material Selection.....	41
2.4.2 Iridium Oxide.....	43

2.5	References.....	47
3.	EXCIMER-LASER DEINSULATION OF PARYLENE-C COATED UTAH ELECTRODE ARRAY TIPS.....	51
3.1	Abstract.....	52
3.2	Introduction.....	52
3.3	Experiment.....	53
3.3.1	Fabrication of Planar Structures and Microelectrode Arrays.....	53
3.3.2	Excimer Laser System and Optical Layout Description.....	54
3.3.3	Surface, Chemical, and Electrical Characterization of Laser Deinsulated Electrodes.....	56
3.4	Results and Discussion.....	57
3.5	Conclusions.....	60
3.6	References.....	60
4.	HYBRID LASER AND REACTIVE ION ETCHING OF PARYLENE-C FOR DEINSULATION OF A UTAH ELECTRODE ARRAY.....	62
4.1	Abstract.....	63
4.2	Introduction.....	63
4.3	Experiment.....	64
4.4	Results and Discussion.....	66
4.5	Conclusions.....	70
4.6	References.....	70
5.	EXCIMER LASER DEINSULATION OF PARYLENE-C ON IRIDIUM FOR USE IN AN ACTIVATED IRIDIUM OXIDE FILM-COATED UTAH ELECTRODE ARRAY.....	71
5.1	Abstract.....	72
5.2	Introduction.....	72
5.3	Material and Methods.....	73
5.4	Results and Discussion.....	76
5.5	Conclusions.....	80
5.6	References.....	81
6.	REDUCTION OF IRIDIUM OXIDE FILM FOR LASER DEINSULATION OF UTAH ELECTRODE ARRAY.....	82
6.1	Abstract.....	83
6.2	Introduction.....	83

6.3	Material and Methods.....	86
6.4	Results and Discussion.....	88
6.5	Conclusions.....	100
6.6	References.....	101
7.	CONCLUSIONS AND FUTURE WORK.....	103
7.1	Conclusions.....	103
7.1.1	Excimer-Laser Deinsulation of Parylene-C Coated Utah electrode Array Tips.....	104
7.1.2	Hybrid Laser and Reactive Ion Etching of Parylene-C for Deinsulation of a Utah Electrode Array.....	105
7.1.3	Excimer Laser Deinsulation of Parylene-C on Iridium for Activated Iridium Oxide Film Coated Utah Electrode Array.....	106
7.1.4	Reduction of Iridium Oxide Films for Laser Deinsulation of Utah Electrode Array.....	107
7.1.5	Contributions.....	109
7.2	Future Work.....	110
7.3	References.....	113

LIST OF FIGURES

1.1 Scanning electron micrograph of (a) the UEA by secondary electrons and of (b) one electrode by back-scattered electrons. The UEA is encapsulated by an insulating Parylene-C layer, with the exception of the tip ($\sim 100 \mu\text{m}$) of the electrode which forms the active site for stimulation and/or recording of neural signals.....	4
1.2 Schematic view of the process flow for wafer-scale fabrication of UEA.....	5
1.3. UV transmission characteristics of a $3 \mu\text{m}$ -thick Parylene-C film. Parylene-C absorbs wavelengths shorter than 280 nm. KrF (248 nm) excimer lasers is effective for laser ablation of Parylene-C.....	8
1.4. Schematic cross-section of the aluminum foil masking process for (a) convex- and (b) concave-type electrode. The solid line represents the aluminum foil mask.....	10
1.5. Schematic cross-section of laser ablation process for individual electrode tip of Utah electrode array. The individual electrode of UEA is directly illuminated by laser beam.....	10
1.6. Diagram of the hybrid deinsulation method using a combination of laser ablation and O_2 RIE.....	12
2.1. Various patterns of TEM mode.....	23
2.2. Schematic potential diagram of KrF excimer laser. The upper level in the diagram is a bound state populated with Kr^+ , F^- . The excited dimer molecule; KrF^* collapses to the ground level; $\text{Kr} + \text{F}$ state with the occurrence of photon emission.....	24
2.3 A schematic diagram of the laser ablation system is presented that highlights the motion stage, beam steering optics, and mask components.....	27
2.4. The surface layers formed when a metal electrode is immersed in an aqueous ionic solution. Double layer is formed by excess charge at the electrode surface and space charges (oriented water dipoles and ions). Electrons can also be transferred directly across the interface during Faradaic reactions [23].....	30
2.5. Potential waveform used in cyclic voltammetry. V is a triangular wave between V_{max} and V_{min}	33

2.6. An example voltammogram with relevant features marked. As the voltage is swept from V_{min} to V_{max} and back again, the current follows the path with reduction and oxidation.....	34
2.7. Cyclic voltammograms of an Ir and AIROF are presented from planar electrodes with 300 μm diameter circle. The CSC_c of Ir and AIROF is 3.5 mC/cm^2 and 10 mC/cm^2 , respectively. The seep rate was 50 mV/s [28].....	36
2.8. An example of (a) equivalent circuit of one time constant, (b) Nyquist plot of circuit (a), and (c) Bode plot of circuit (a)	38
2.9. Equivalent circuit of the electrode-electrolyte systems. R_s is the electrolyte resistance, R_{ct} is the charge transfer resistance, and the CPE is a constant phase element.....	40
2.10. Potential transient of the SIROF planar electrode shows access voltage (V_a) and maximum cathodic (E_{mc}) potential excursions during a constant current biphasic pulse. The current pulse amplitude and width per phase is 1.2 mA and 500 μs , respectively.....	42
2.11. The unit cell of the Rutile structure of iridium oxide (IrO_2) is presented. The silver balls represent Ir, and the red balls represent oxygen.....	44
2.12. Faradaic reaction of iridium oxide film is presented with the equations of chemical reaction. The reversible Faradaic reaction involves reduction and oxidation as the valence transition between Ir^{3+} and Ir^{4+} state of the iridium oxide.....	45
3.1. The structure of Parylene-C.....	53
3.2. (a) Scanning electron micrograph of UEAs (left) and the backscattered image of the electrode array in detail (right), (b) Schematic view of the process flow for wafer-scale fabrication of the Utah electrode array.....	53
3.3. Schematics diagram of the laser ablation system.....	54
3.4. 30° tilted SEM (Scanning electron micrographs of the circles on a silicon substrate after laser ablation with 1000 mJ/cm^2 . (a) 10 pulses, (b) 20 pulses, (c) 30 pulses and (d) 100 pulses.....	55
3.5. (a) The etch depth of the Parylene as a function of the number of laser pulses, (b) the Parylene etch rate by as a function of the fluence.....	55
3.6. (a) SEM images (backscattering images) for films with three different thicknesses (0.4 μm , 0.8 μm , and 1.1 μm) exposed to a single laser pulse with 1680 mJ/cm^2 fluence for investigation of iridium oxide film fracture tendency. (b) SEM images for films with three different thicknesses (0.4 μm , 0.8 μm , and 1.1 μm) exposed to 100	

laser pulses with 1680 mJ/cm ² fluence. (c) SEM image of the laser ablated hole on a Parylene-coated iridium oxide film.....	56
3.7. SEM images (upper) and AFM images (bottom) of iridium oxide films before (left) and after (right) laser ablation.....	57
3.8. X-ray photoemission spectra of (a) the Parylene film (left) and laser ablated spot on Parylene coated iridium oxide film (right), (b) as deposited iridium oxide film (left) and Ir 4f peaks in high resolution scan (right) and (c) laser ablated spot on as deposited iridium oxide film (left) and Ir 4f peaks in high resolution scan (right)....	58
3.9. 30° tilted scanning electron micrograph using backscattered electron images of a Utah electrode tip having 1.1 μm thickness iridium oxide film after laser deinsulation by (a) 35, 100, and 200 pulses with the fluence of 1440 mJ/cm ² and (b) fluence of 1200, 1440, and 1680 mJ/cm ² with 150 laser pulses.....	59
3.10. Impedance values as a function of the tip exposure of laser deinsulated Utah electrode. The tip exposure lengths were measured by SEM at a 30° sample tilt angle. The solid line is the trend line with the equation $y=41.309x^{-1.406}$	59
4.1. (a) Photograph of a Utah electrode array with 10x10 electrodes, (b) SEM image of a Utah electrode tip fabricated by the oxygen plasma etching using an aluminum foil mask.....	64
4.2. Schematics of the laser ablation system.....	65
4.3. UV transmission characteristics of a 3 μm-thick Parylene-C film.....	66
4.4. (a) SEM image of a 200 μm diameter hole on an iridium oxide film after laser ablation of 3 μm thickness Parylene-C film with a fluence of 1 J/cm ² and a number of pulses of 100, (b) backscattered electron (BSE) image of (a), and (c) magnified image at the boundary between Parylene-C and iridium oxide film.....	66
4.5. X-ray photoemission spectra of (a) a Parylene film, (b) a laser ablated spot on an iridium oxide film, and (c) a laser ablated spot on an iridium oxide film with high resolution scan around the C 1s peak.....	67
4.6. (a) X-ray photoemission spectra of a laser ablated spot on an iridium oxide film after 1 minute oxygen plasma treatment, (b) a high resolution scan of (a) around the Ir 4d and C 1s peaks.....	67
4.7. Imaging XPS data for (a) the Ir 4f peak before oxygen plasma treatment, (b) the Ir 4f peak after 1 minute oxygen plasma treatment, (c) the C 1s peak before oxygen plasma treatment, (d) the C 1s peak after 1 minute oxygen plasma treatment.....	68

4.8. Scanning electron micrographs using backscattered electron imaging (a) after laser deinsulation using the fluence of 750 mJ/cm ² and the number of pulses of 200, (b) after laser deinsulation and 4 minutes oxygen plasma etching, (c) after laser deinsulation and 8 min oxygen plasma etching.....	68
4.9. (a) Thickness of the Parylene-C etched as a function of oxygen plasma etching time, (b) variation of the electrode tip exposures for electrodes with two different initial exposures of 11~13 μm and 17~19 μm as a function of the oxygen plasma etching time.....	69
4.10. (a) Impedance of electrodes with initial tip exposures of 11~13 μm and 17~19 μm as a function of the oxygen plasma etch time, (b) impedance of electrodes fabricated by laser ablation and 2 minutes oxygen plasma etching. The solid line is the trend line with the equation $y = 15.915x^{-1.66}$ and $R^2 = 0.97$	69
5.1. Faradaic reaction of activated iridium oxide film.....	73
5.2. (a) Planar view of the AIROF electrode, (b) Schematic process flow for the planar AIROF electrode fabrication.....	74
5.3. (a) Backscattered SEM images of iridium films with three different thicknesses (50 nm, 200 nm, and 600 nm) exposed to 100 laser pulses with 1920 mJ/cm ² fluence. (b) Backscattered SEM images of SIROF (600 nm) exposed to the different laser fluences (960, 720, and 480 mJ/cm ²).....	75
5.4. (a) The optical image of laser ablated spot (diameter of 100 μm) on a soda-lime glass. (b) Surface profiles of the edge of the circle ablated by different laser fluences (left) and after 2 minutes OPE treatment (right)	75
5.5. X-ray photoemission spectra of (a) C 1s peak of as-deposited Parylene-C, (b) Cl 2p peak of as-deposited Parylene-C, (c) C 1s peak of the laser ablated Parylene-C and (d) Cl 2p peak of the laser ablated Parylene-C.....	76
5.6. (a) SEM images of laser deinsulated holes on a Parylene coated iridium film before (left) and after (right) OPE treatment. (b) SEM images of iridium film (left) and AIROF film (right). (c) AFM images of iridium film (left) and AIROF film (right)	77
5.7. X-ray photoemission spectra showing (a) Ir 4f peak of the as-deposited iridium film, (b) O 1s peak of the as-deposited iridium film, (c) Ir 4f peak of the AIROF and (d) O 1s peak of the AIROF.....	78
5.8. (a) SEM images of AIROF by rectangular pulse levels of -0.85 and 0.95 V (left), -0.9 and 0.95 V (center), and -0.95 and 0.95 V (right). (b) magnified images of (a).....	78

5.9. Amplitude (upper) and phase (bottom) of impedance of planar electrodes with iridium active area formed by three different deinsulation conditions and with AIROF active area (area of the active region $\approx 70600 \mu\text{m}^2$).....	79
5.10. Cyclic voltammograms of the planar iridium and AIROF electrodes (area of the active region $\approx 70600 \mu\text{m}^2$). The electrode voltage was measured with respect to the Ag AgCl reference electrode.....	79
5.11. (a) SEM images of a laser deinsulated Utah electrode array tip with iridium film (left) and SIROF (right). (b) SEM images of as-deposited iridium film (left), AIROF activated by rectangular pulses with levels of -0.8 and 0.95 V (center), and AIROF activated by rectangular pulses with levels of -0.85 and 0.95 V (right).....	80
5.12. EIS (a) and CV (b) of AIROF Utah microelectrode (geometric surface area $\approx 6000 \mu\text{m}^2$).....	80
6.1. TGA of IrO_x by nitrogen and forming gas.....	88
6.2. XRD spectra of (a) as-deposited SIROF and (b) annealed SIROF according to four different temperatures (410, 310, 220, and 210 °C).....	90
6.3. SEM images (upper) and AFM images (bottom) of (a) as-deposited SIROF, (b) annealed SIROF, and (c) laser ablated annealed SIROF.....	91
6.4. Optical image of Ti/SIROF films on Si substrate after mechanically scratching is presented in (a). Three colors were disclosed as blue (1), silver (2) and dark gray (3). (b) is the imaging XPS for Ir 4f peak of the sample same to Figure 6.4 (a). Spots (1), (2) and (3) in Figure 6.4 (b) match to the numbers in Figure 6.4 (a).....	92
6.5. X-ray photoemission spectra of (a) spots (1), (b) spots (2), and (c) spots (3) in Figure 6.4.....	93
6.6. Electrochemical analysis of planar electrode is presented by (a) backscattered SEM image of laser deinsulated hole with 300 μm diameter, (b) Bode plot of different film stacks at particular annealing temperature (Ti/SIROF at 410 °C, Ti/Ir/SIROF at 410 °C and Ti/Ir/SIROF at 210 °C), (c) cyclic voltammograms of the same samples as (b), and (d) potential transient of two different structures (Ti/Ir/SIROF at 210 °C and Ti/SIROF at 410 °C).....	94
6.7. Electrochemical analysis of 3D UEA tip is presented by (a) SEM image of laser deinsulated Utah electrode array tip, and (b) impedance, (c) CSC_c and (d) CIC values of UEAs with Ti/Ir/SIROF film structure annealed at 210 °C as a function of their tip exposure fabricated by the laser deinsulation. The solid lines are a trend line with the equations, $y = 0.0817e^{-0.028x}$, $y = 91.525e^{-0.019x}$ and $y = 1.0246e^{-0.005x}$ for Figure (b), (c), and (d), respectively.....	98

ACKNOWLEDGMENTS

First of all, I would like to thank Dr. Florian Solzbacher, who gave me a big opportunity for my doctoral study in the University of Utah. His generous leadership and encouragement led me to become enthusiastic in research. This dissertation is the result of his guidance and persistent support.

I would like to thank Dr. Loren Rieth, who gave me invaluable inspiration and direction. Without his insightful advice and scientific discussion, this journey would not have been completed. I have learned a lot of academic and research lessons from him, which will be very helpful in my future career.

I would like to show my deepest appreciation to Dr. Jong-In Song in Gwangju Institute of Science and Technology. His unstinting trust and support motivated me to start my doctoral study. His thoughtful advice and encouragement were the source and base of my achievements.

My gratitude is extended to many fellows for providing a stimulating environment and their assistance. Special thanks to Prashant Tathireddy, Sandeep Negi, Rajmohan Bhandari, Mohit Diwekar, Rohit Sharma, Xianzong Xie, Tanya Abaya, and Ryan Coldwell. Appreciation is also extended to Dr. Brian van Devener and Brian Baker for the assistance on surface analysis, equipment training, and troubleshooting.

I would like to deliver my deepest gratitude to my wife, Hyun-Jin, for her unconditional understanding and love. It would be impossible for me to have this

dissertation without her devotion and sacrifice. My gratitude is also extended to my lovely son, John. Just his being makes me happiest in the world. Also, his babbling has always cheered me up.

Finally, I would like to thank my parents for their everlasting love, support, and encouragement throughout my life. Their prayer has led me in the right direction without the trials of life. I owe everything to my parents forever.

CHAPTER 1

INTRODUCTION

1.1 Neural Interfaces

Neural interfaces are devices designed to exchange information with the nervous system. These interfaces often use electrodes to record and/or stimulate neural signals. In recent years, their applications in neural prostheses have been rapidly developed by sophisticated modern microfabrication technologies, improvements in electronics and computer hardware, and advances in material sciences [1]. Applications include cochlear implants for recovering hearing [2-4], visual prostheses for restoring vision [5], and neural prosthetics for reanimating paralyzed limbs or controlling prosthetic limbs in patients with strokes, spinal cord injuries, or movement disorders [6]. Another currently available therapeutic neural interface is deep brain stimulation for essential tremor, Parkinson's disease, and dystonia, also being investigated for treating epilepsy, depression, and chronic pain [7-10].

One essential part in all these applications is the neural interface in which an electrode records and/or stimulates neural signals. A feature that distinguishes neural interfaces is how invasive the neural interface (or placement procedure) is. Noninvasive systems primarily exploit electroencephalograms (EEGs) from the surface of the skull to control computer cursors or other systems, such as the P 300 speller enabling patients to write through cortical EEG measurements [11]. It provides a simple communications tool

for paralyzed people. However, despite having the great advantage of not exposing the patient to the risks of neurosurgery, EEG-based techniques provide communication channels of limited capacity due to low spatial resolution (3 ~ 5 cm) and susceptibility to artifacts during acquisition of neural data. The low conductivity of the skull attenuates the neural signal transmitting from brain to scalp electrodes significantly [12, 13].

The next level for more invasive neural interfaces is surface and/or cuff electrodes, which need to be placed surgically, but do not penetrate the neural tissue. Electrocorticography (ECoG) strip electrodes are a partially invasive system which have more spatial resolution (0.5 ~ 1 cm) than EEG electrodes. The detected signals are composed of local field potentials (LFPs) directly from the surface of the cortex. However, it has less spatial resolution than penetrating electrodes. Penetrating electrodes are based on recordings from ensembles of neurons or on the activity of multiple neurons, including LFPs. These provide neural signals with high spatial resolution ($< 200 \mu\text{m}$). However, it carries surgical risks associated with penetrating it into the cortex [14-18].

1.2 Penetrating Silicon-Based Microelectrodes

The development and use of implanted Si-based electrode arrays dates back to the late 1950s [19]. One of the important types of penetrating neural interfaces are the wire-type microelectrodes. This type of technology continues to be widely used by many laboratories, including industry for electrophysiological recordings. However, a manual production process for wire-type microelectrodes makes it difficult to precisely control the electrode geometries and electrochemical properties for electrode sites.

Mass-fabricated microelectrodes were achieved by photolithographic and microfabrication methods to solve the difficulty in assembling reproducible wire-type

microelectrodes [19, 20]. Multiple types of microelectrodes can be produced at the same time on a substrate by multiple designs in a photolithographic mask, allowing for numbers of microelectrodes to be made with less production costs. It can also be used to make microelectrodes that incorporate multiple recording and/or stimulation sites with well-defined spatial arrangements for compatibility with the well-organized structures of the brain. The first substrate to produce multisite microelectrodes was silicon [21-29]. The capability of surface and bulk micromachining through chemical etching, etc., of the substrate is one of the key properties of silicon. Individual electrodes can be fabricated from a single substrate and small features such as channels in the substrate can be constructed. The semiconductor properties of silicon can be altered by doping. Silicon also plays host to fabrication of integrated circuits. It has many advantages, making it widely used as the basis for forming microelectrode arrays. Silicon-based microelectrode arrays can provide a solution for high reproducibility and the possibility of integration of components for signal processing and wireless telemetry. The Utah electrode array (UEA) is a prominent example of silicon-based microelectrode arrays that are used clinically in research [30, 31].

UEAs typically have 100 electrodes in a 10×10 grid, and were developed to provide an interface originally for visual prosthetics, and are now commonly used for motor prosthetics. Figure 1.1 shows a scanning electron micrograph (SEM) of a UEA. Individual microelectrodes extend 1.5 mm from the 10×10 mm planar substrate, as shown in Figure 1.1 (a). The tip of each electrode is metallized with sputter-deposited iridium oxide (SIROF) to facilitate electronic to ionic transduction. The conducting highly doped silicon shanks are insulated from each other using glass. The exterior of the array is

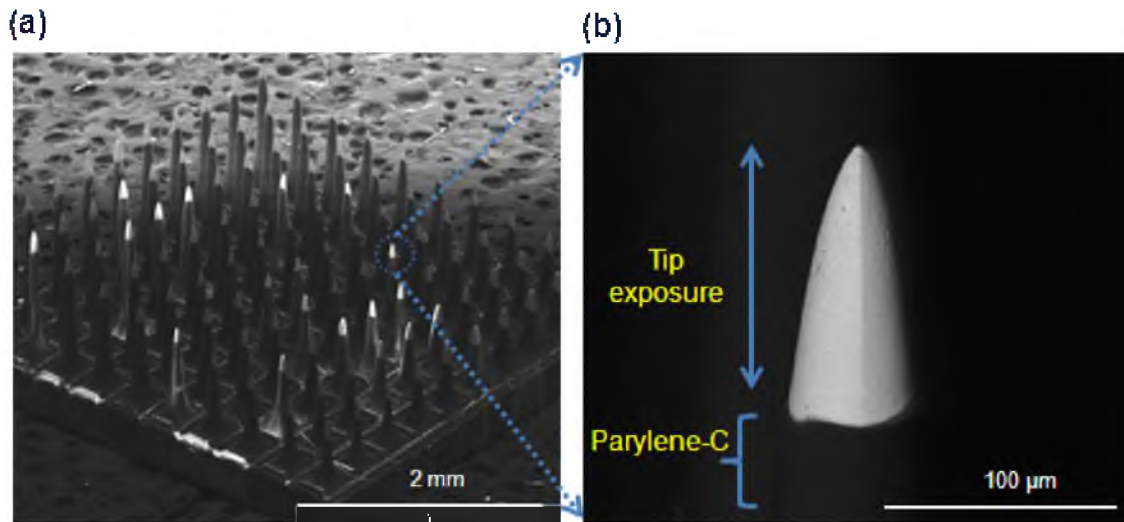


Fig 1.1 Scanning electron micrograph of (a) the UEA by secondary electrons and of (b) one electrode by back-scattered electrons. The UEA is encapsulated by an insulating Parylene-C layer, with the exception of the tip ($\sim 100 \mu\text{m}$) of the electrode which forms the active site for stimulation and/or recording of neural signals.

insulated using biocompatible Parylene-C, and each tip is deinsulated in order to record or stimulate neural signals. A higher magnification image of one electrode tip showing the exposed tip ($\sim 100 \mu\text{m}$) of the electrode which forms the active site (tip exposure), and the adjacent Parylene encapsulation, is presented in Figure 1.1 (b).

Figure 1.2 is the schematic view of the process flow for fabrication of UEAs. 2 mm thick, c-Si (100), *p*-type wafers with the resistivity of $0.01 \sim 0.05 \Omega\cdot\text{cm}$ and a diameter of 75 mm are used as substrates to make the UEAs. Back-side dicing, glassing, and grinding are used to create electrical isolation for the electrodes, and the back-side of the electrode is metallized as pads for wire bonding. Then, front-side dicing and wet etching are used to shape the electrodes. Finally, array singulation, tip metallization, and Parylene deposition after annealing are performed to finish the devices. Titanium and

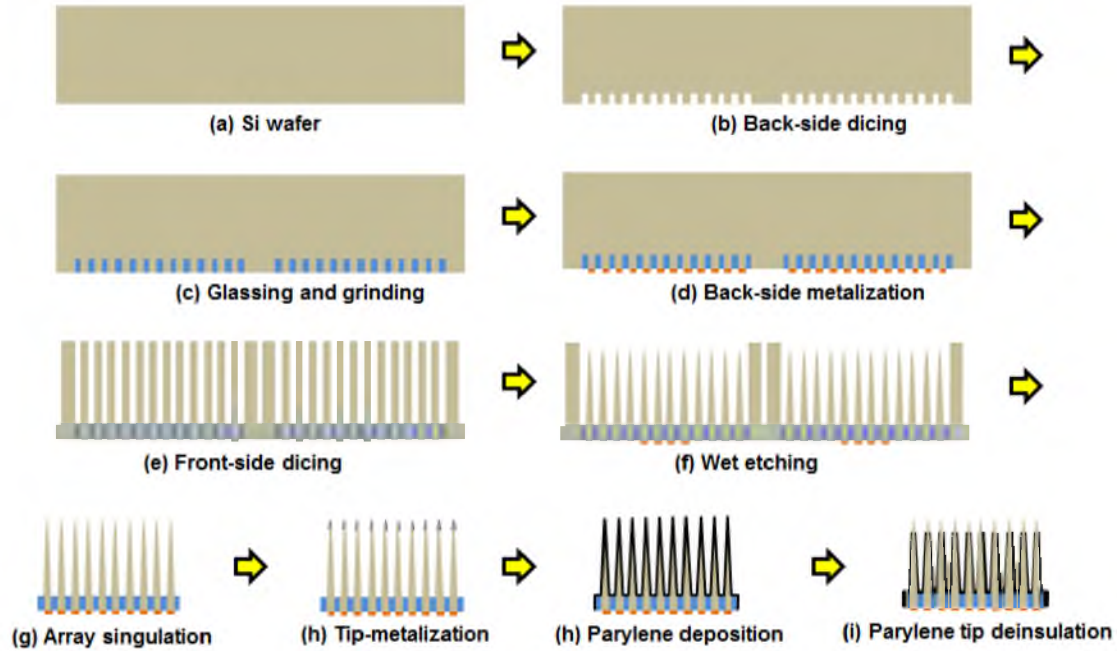


Fig 1.2 Schematic view of the process flow for wafer-scale fabrication of UEA

iridium oxide are deposited using DC and Pulsed-DC sputter deposition during the tip metallization, respectively, and annealed in forming gas (98% Ar and 2% H₂) for 45 minutes in 375 °C temperature. As the last step, tip deinsulation is carried out. The fabrication of UEAs is described elsewhere in detail [32, 33].

1.3 Encapsulation and Tip Metallization Materials for Laser Deinsulation

Microelectrode arrays need to be encapsulated by a biocompatible material to protect the device against the aggressive body fluids and the body tissue against corrosion products and nonbiocompatible materials. Parylene-C is one of the most highly use polymeric material for the insulation of neural interface devices [34]. It has good biocompatibility (USP Class VI polymer), chemical and biological inertness, good barrier

properties (the best within the parylene group), a slippery surface, and is an electrical insulator ($\rho = \sim 10^{15} \Omega \cdot \text{cm}$).

Parylene-C is deposited in a chemical vapor deposition (CVD) process to generate a thin layer (1 ~ 30 μm) which is highly conformal and can coat high-aspect ratio features [34]. It has advantages over other technologies like dip coating (silicones and epoxies), die casting (silicones and epoxies), or spin coating (polyimides and silicones), where the ability to penetrate small holes or to cover sharp edges with uniform thickness is limited.

Selection of the electrode material for tip metallization is critical for the performance of neural interface. The ideal electrode should be safe and effective. For safety, it needs to cause little damage to the surrounding tissue and have no adverse effects on the body. The electrode material should be biocompatible and mechanically stable during surgery and after implantation. Chronically implanted devices can remain in use for years, so the tip material needs to withstand insertion forces, resist corrosion, and be relatively biocompatible.

The charge should be effectively injected into the electrode material even with very small electrode area to selectively elicit action potentials. Materials with higher charge injection capacity (mC/cm^2) can allow higher stimulation current densities while operating within safe voltage limits that avoid the electrolysis of water and bubble formation, oxidation of organic and inorganic species, and material corrosion or dissolution. Also, since a higher CIC lowers the potential required for stimulation, this can decrease power consumption, which is critical for implanted stimulation systems. Iridium oxide is a popular material for electrode active sites due to the Faradaic reaction transduction mechanism. It also has the highest charge injection capacity range from 1 to

4 mC/cm². The reduction and oxidation in iridium oxide film is primarily from the valence change between Ir³⁺ and Ir⁴⁺ states [35, 36].

Laser is an attractive tool for micromachining due to the ability to generate high intensity of power for ablation. The directionality of laser enables it to make high-aspect ratio structures [37]. It is also appropriate for applications such as deinsulation. Laser ablation of Parylene has already been used since the early 90s in electrodes for recording neural signals [38]. Laser deinsulation has also been demonstrated to remove the Parylene from biomedical microelectrodes based on Pt tips [39, 40], and to ablate micron thick Parylene films from copper surfaces [41]. However, the laser power can easily damage the substrate during laser ablation of Parylene-C. When iridium oxide films are used under Parylene-C, damage by the laser irradiation must be minimized.

In this study, the encapsulation material, Parylene-C, was removed from the active electrode tips of the iridium oxide coated UEA using a laser. The ultraviolet light (248 nm) from the KrF excimer laser is strongly absorbed by Parylene-C. Parylene-C absorbs wavelengths shorter than 280 nm, as shown in Figure 1.3 [42]. The KrF excimer laser photon energy is high enough to break the chemical bonds of the Parylene-C, which makes this wavelength more efficient at ablating the films compared to lasers with longer wavelengths (> 300 nm), and results in less residual heat in the iridium oxide.

1.4 Hypotheses and Specific Aims

The goal of this study is to develop a laser ablation method to deinsulate Parylene from the tips of Utah electrode arrays, which have complex 3-D geometries. The UEA uses a 10×10 array sharp needle-type electrode array based on silicon and the pitch between electrodes is 400 μm with 1.5 mm length.

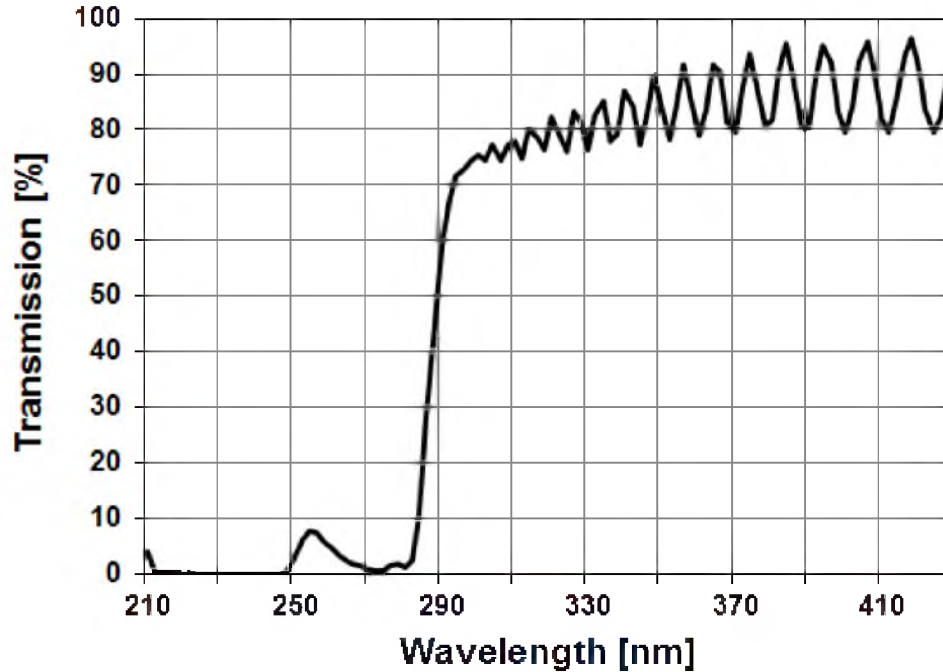


Fig 1.3. UV transmission characteristics of a 3 μm -thick Parylene-C film. Parylene-C absorbs wavelengths shorter than 280 nm. KrF (248 nm) excimer lasers is effective for laser ablation of Parylene-C.

In this study, we investigated a new deinsulation method using a hybrid approach that includes laser ablation and O_2 plasma etching, as an alternative to the conventional reactive ion etching process with an Al foil mask. Reactive ion etching (RIE) with an Al foil mask that has traditionally been used for fabrication of Utah electrode arrays is an effective method to remove the Parylene insulation compared with other methods, such as heating or high-voltage arcing methods [43, 44]. However, the method can result in nonuniform tip exposure and incurring variations in impedance across the array. Also, the method of using a foil mask in RIE deinsulation makes it difficult to deinsulate arrays with high density or complicated electrode geometries that have specific purposes in neural interface application. Figure 1.4 shows instances of the poked electrode array by aluminum foil mask for convex and concave type electrode arrays that

have nonlinear gradients of electrode heights and are useful for retina interfaces or peripheral nerve interfaces [45]. The tip exposure is nonuniform above the aluminum foil mask that results in difficulties to use the RIE deinsulation method in neural interface electrode. The laser ablation technique can be used to deinsulate an individual electrode tip to solve these issues, as shown in Figure 1.5. Laser deinsulation can be explored to get very fine tip exposure ($< 20 \mu\text{m}$) which increases selectivity in acquiring the neural signals as well. The selectivity is a capability to stimulate or record a small population of neural tissues without activating close tissues. A small tip exposure ($< 40 \mu\text{m}$) with improved spatial resolution needs to be designed to record/stimulate a small population of neuron for cortical neural interfaces [46, 47].

Two of the challenges faced in developing a laser deinsulation process were damage to the thin film tip metallization and redeposition of carbon by-products that can lead to variations in the electrode impedance and charge injection capacity [48]. Specific aims to address these challenges are 1) solving the laser-induced film damage issue through optimization of the fabrication process focused on laser parameters, 2) developing a new laser deinsulation method for solving the carbon residue issue, 3) developing an activated iridium oxide film (AIROF) tip metallization to expand the laser deinsulation process window, and 4) stabilizing an annealing process variation to acquire SIROF having both high electrochemical performance (in electrochemical impedance, charge storage capacity, and charge injection capacity) and film damage resistance against laser power. The objectives of each specific aim are as follows:

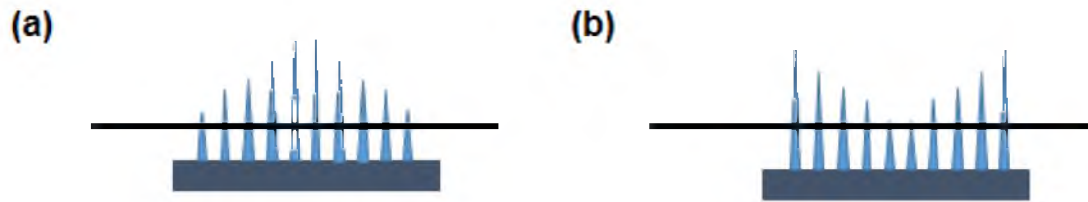


Fig 1.4. Schematic cross-section of the aluminum foil masking process for (a) convex- and (b) concave-type electrode. The solid line represents the aluminum foil mask.

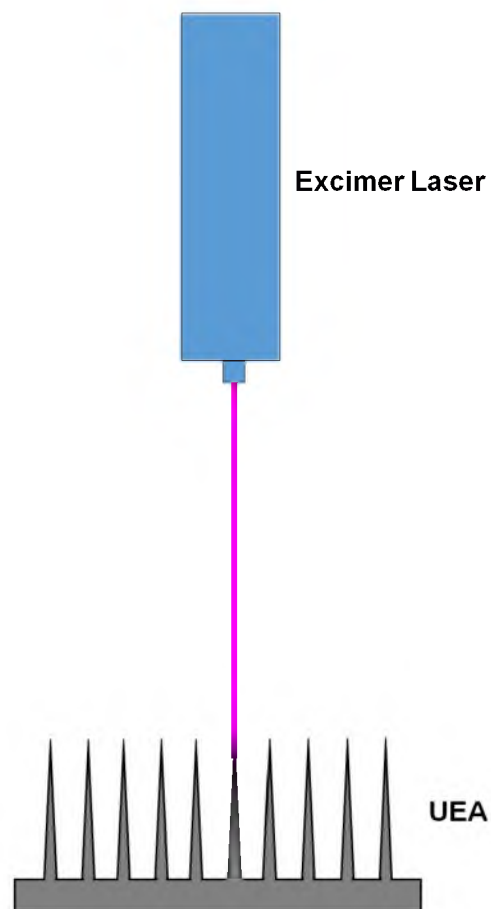


Fig 1.5. Schematic cross-section of laser ablation process for individual electrode tip of Utah electrode array. The individual electrode of UEA is directly illuminated by laser beam.

- (a)** Development and characterization of a laser ablation process to deinsulate the tips of Parylene encapsulated Utah electrode arrays (UEAs): The effect of laser beam fluence and number of pulse on the Parylene etch rate were evaluated in connection with the tip exposure of UEAs. The surface analysis, such as X-ray photoelectron spectroscopy (XPS) or atomic force microscopy (AFM), was performed using planar test structures. The properties and thickness of the SIROF tip metallization were optimized to understand and minimize the damage to the film from laser ablation.
- (b)** Development of a hybrid deinsulation method using a combination of laser ablation and O₂ RIE, as shown in Figure 1.6: Utah electrodes with fine tip exposures were developed by the hybrid deinsulation method to increase the selectivity for stimulating or recording a small population of neurons. The removal of carbon debris using an O₂ RIE process on the laser ablated active area in tips as well as the whole electrode structure was evaluated to increase the accuracy, reproducibility, and yield of tip exposure, and impedance in electrode array.
- (c)** Development of an AIROF microelectrode array that resists damage from laser irradiation: The damage of iridium and iridium oxide using a range of laser conditions was compared to determine the capability of laser deinsulation on iridium. Laser parameters were investigated to minimize carbon residue and complete removal of Parylene on the sidewall of the electrode tip using high fluence ($> 1.5 \text{ J/cm}^2$) with less number of pulses to improve tip reproducibility. Laser deinsulation of Parylene-C on iridium and

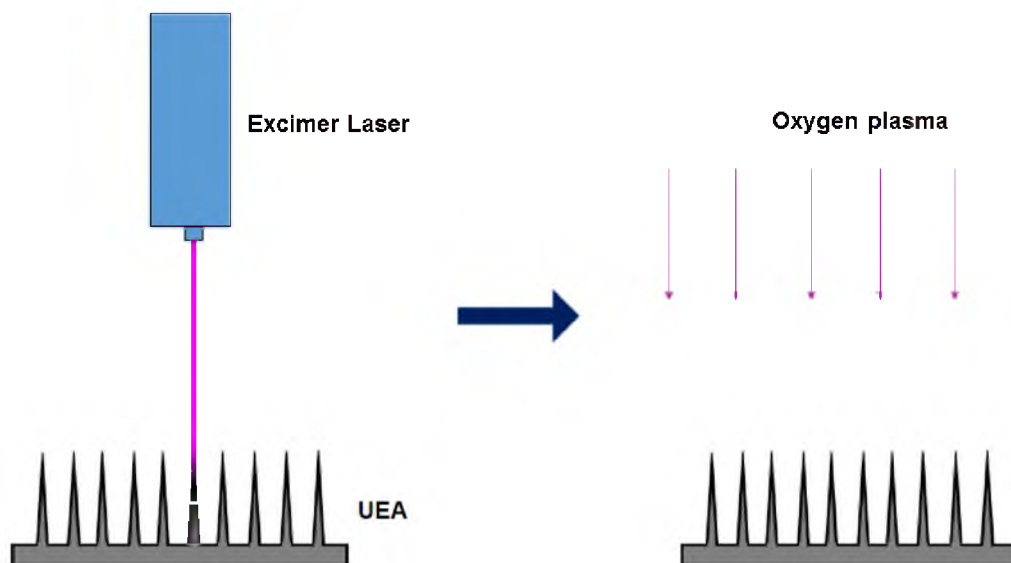


Fig 1.6. Diagram of the hybrid deinsulation method using a combination of laser ablation and O₂ RIE

subsequent activation of iridium film were studied by surface analysis methods and electrochemical techniques for activated iridium oxide coated UEAs.

- (d)** Development of a partially deoxidized SIROF Utah electrode array to acquire damage resistant films with good electrochemical performance (low impedance and high CIC): The annealing temperature was optimized to control the amount of deoxidization on SIROF. The charge injection capacity was maximized by adjusting the degree of deoxidization of SIROF as low as possible. An oxygen diffusion from SIROF to Ti during annealing was investigated with a diffusion barrier Ir between Ti and SIROF to solve the Ti degradation issue.

This dissertation is organized as follows. Chapter 1 introduces the neural interface and silicon-based microelectrode array for the neural interface application. The encapsulation and tip metallization material for laser deinsulation are discussed. Finally, the hypotheses and specific aims of this research are discussed.

Chapter 2 covers the excimer laser system, the electrode tip deinsulation methods, and charge injection mechanism/materials found in the literature. Electrochemical characterization including electrochemical impedance spectroscopy, cyclic voltammetry, and potential transient for electrode materials is reviewed.

Chapter 3 investigates the laser ablation method of Parylene coated Planar and 3D microelectrode. The effect of laser beam fluence and number of pulse on the Parylene etch rate was studied to achieve the laser deinsulation of Parylene coated 3D Utah electrode array. This work is published in *Sensor and Actuator: B Chemical*, 2012.

Chapter 4 reports the hybrid deinsulation method using laser ablation and oxygen reactive ion etching. The experiments were designed to develop Utah electrodes with controllable fine tip exposures and solve the carbon debris issue by O₂ RIE treatment on the laser ablated active area in tips. This work is published in *Micromechanics and Microengineering*, 2012.

Chapter 5 compares the as-deposited SIROF and AIROF coated Utah electrode array to get a high resistance array to film fracture. This work is published in the *Journal of Neuroscience Methods*, 2013.

Chapter 6 investigates the partially deoxidized SIROF Utah electrode array to stabilize an annealing process variation to acquire a SIROF having both high

electrochemical performance and film damage resistance against laser power. This work will be submitted to *Biosensors and Bioelectronics*, 2013.

Finally, the advantages and disadvantages of the laser deinsulation method in implantable microelectrodes are summarized and conclusions discussed in Chapter 7. Additionally, suggestions for future study are also provided in Chapter 7.

1.6 References

- [1] W. F. Agnew and D. B. McCreery, *Neural Prosthesis: Fundamental studies*: Prentice Hall Biophysics & Bioengineering Series, 1990.
- [2] B. S. Wilson, D. T. Lawson, J. M. Muller, R. S. Tyler, and J. Kiefer, "Cochlear implants: some likely next steps," *Annu Rev Biomed Eng*, vol. 5, pp. 207-49, 2003.
- [3] G. M. Clark, "The multiple-channel cochlear implant: the interface between sound and the central nervous system for hearing, speech, and language in deaf people - a personal perspective," *Phil. Trans. R. Soc. London B*, vol. 64, pp. 186-205, 2006.
- [4] R. K. Shepherd and D. B. McCreery, "Basis of electrical stimulation of the cochlea and the cochlear nucleus," *Adv. Otorhinolaryngol.*, vol. 64, pp. 186-205, 2006.
- [5] J. D. Weiland, W. Liu, and M. S. Humayun, "Retinal prithesis," *Annu Rev Biomed Eng*, vol. 7, pp. 361-401, 2005.
- [6] X. Navarro, T. B. Krueger, N. Lago, S. Micera, T. Stieglitz, and P. Dario, "A critical review of interfaces with the peripheral nervous system for the control of neuroprostheses and hybrid bionic systems," *J Peripher Nerv Syst*, vol. 10(3), pp. 229-58, 2005.
- [7] A. L. Benabid, "Deep brain stimulation for Parkinson's disease," *Current Opinion in Neurobiology*, vol. 13(6), pp. 696-706, 2003.
- [8] Y. Li and D. J. Mogul, "Electrical control of epileptic seizures," *Journal of Clinical Neurophysiology*, vol. 24, pp. 197-204, 2007.
- [9] J. S. Perlmutter and J. W. Mink, "Deep brain stimulation," *Ann. Rev. Neurosci.*, vol. 29, pp. 229-57, 2006.
- [10] S. Jezernik, M. Craggs, W. M. Grill, G. Creasey, and N. J. Rijkhoff, "Electrical stimulation for the treatment of bladder dysfunction: current status and future possibilities," *Neurol. Res.*, vol. 24, pp. 413-430, 2002.
- [11] D. J. Krusienski, E. W. Sellers, D. J. McFarland, T. M. Vaughan, and J. R. Wolpaw, "Toward enhanced P300 speller performance," *Journal of Neuroscience Methods*, vol. 167, pp. 15-21, 2008.
- [12] J. Wolpaw, N. Birbaumer, D. McFarland, G. Pfurtscheller, and T. Vaughan, "Brain-Computer interfaces for communication and control," *Clin. Neurophysiol.*, vol. 113, pp. 767-791, 2002.
- [13] N. Birbaumer, "Brain-computer-interface research: coming of age," *Clin Neurophysiol.* , vol. 117(3), pp. 479-83, 2006.

- [14] M. A. L. Nicolelis, L. A. Baccala, R. C. S. Lin, and J. K. Chapin, "Sensorimotor encoding by synchronous neural ensemble activity at multiple levels of the somatosensory system," *Science*, vol. 268, pp. 1353-1358, 1995.
- [15] M. A. L. Nicolelis, D. Dimitrov, J. M. Carmena, R. Crist, G. Lehew, J. D. Kralik, *et al.*, "Chronic, multisite, multielectrode recordings in macaque monkeys," *Proceedings of the National Academy of Sciences*, vol. 100, pp. 11041-11046, September 16, 2003.
- [16] M. A. Nicolelis, A. A. Ghazanfar, B. M. Faggin, S. Votaw, and L. M. Oliveira, "Reconstructing the engram: simultaneous, multisite, many single neuron recordings," *Neuron*, vol. 18, pp. 529-37, Apr 1997.
- [17] M. A. Nicolelis and S. Ribeiro, "Multielectrode recordings: the next steps," *Curr Opin Neurobiol*, vol. 12, pp. 602-6, Oct 2002.
- [18] M. A. L. Nicolelis, "Actions from thoughts," *Nature*, vol. 409, pp. 403-407, 2001.
- [19] K. C. Cheung, "Implantable microscale neural interfaces," *Biomed Microdevices*, vol. 9, pp. 923-38, Dec 2007.
- [20] J. J. Burmeister and G. A. Gerhardt., "Neurochemical arrays," in *In Encyclopedia of sensors*. vol. 6, ed: Eds. C. Grimes, E. Dickey, and M. V. Pishko. Stevenson Ranch, CA: American Scientific Publishers, p. 525, 2006.
- [21] D. J. Anderson, K. Najafi, S. J. Tanghe, D. A. Evans, K. L. Levy, J. F. Hetke, *et al.*, "Batch-fabricated thin-film electrodes for stimulation of the central auditory system," *IEEE Trans Biomed Eng*, vol. 36, pp. 693-704, Jul 1989.
- [22] S. Schmidt, K. Horch, and R. Normann, "Biocompatibility of silicon-based electrode arrays implanted in feline cortical tissue," *J Biomed Mater Res*, vol. 27, pp. 1393-9, Nov 1993.
- [23] G. T. Kovacs, C. W. Storment, M. Halks-Miller, C. R. Belczynski, Jr., C. C. Della Santina, E. R. Lewis, *et al.*, "Silicon-substrate microelectrode arrays for parallel recording of neural activity in peripheral and cranial nerves," *IEEE Trans Biomed Eng*, vol. 41, pp. 567-77, Jun 1994.
- [24] C. C. Della Santina, G. T. Kovacs, and E. R. Lewis, "Multi-unit recording from regenerated bullfrog eighth nerve using implantable silicon-substrate microelectrodes," *J Neurosci Methods*, vol. 72, pp. 71-86, Mar 1997.
- [25] Q. Bai, K. D. Wise, and D. J. Anderson, "A high-yield microassembly structure for three-dimensional microelectrode arrays," *IEEE Trans Biomed Eng*, vol. 47, pp. 281-9, Mar 2000.

- [26] K. Najafi, J. Ji, and K. D. Wise, "Scaling limitations of silicon multichannel recording probes," *IEEE Trans Biomed Eng*, vol. 37, pp. 1-11, Jan 1990.
- [27] T. H. Yoon, E. J. Hwang, D. Y. Shin, S. I. Park, S. J. Oh, S. C. Jung, *et al.*, "A micromachined silicon depth probe for multichannel neural recording," *IEEE Trans Biomed Eng*, vol. 47, pp. 1082-7, Aug 2000.
- [28] R. J. Vetter, J. C. Williams, J. F. Hetke, E. A. Nunamaker, and D. R. Kipke, "Chronic neural recording using silicon-substrate microelectrode arrays implanted in cerebral cortex," *IEEE Trans Biomed Eng*, vol. 51, pp. 896-904, Jun 2004.
- [29] D. R. Kipke, R. J. Vetter, J. C. Williams, and J. F. Hetke, "Silicon-substrate intracortical microelectrode arrays for long-term recording of neuronal spike activity in cerebral cortex," *IEEE Trans Neural Syst Rehabil Eng*, vol. 11, pp. 151-5, Jun 2003.
- [30] K. E. Jones, P. K. Campbell, and R. A. Normann, "A glass/silicon composite intracortical electrode array," *Ann Biomed Eng*, vol. 20, pp. 423-37, 1992.
- [31] E. M. Maynard, C. T. Nordhausen, and R. A. Normann, "The Utah intracortical Electrode Array: a recording structure for potential brain-computer interfaces," *Electroencephalogr Clin Neurophysiol*, vol. 102, pp. 228-39, Mar 1997.
- [32] P. K. Campbell, K. E. Jones, R. J. Huber, K. W. Horch, and R. A. Normann, "A silicon-based, three-dimensional neural interface: manufacturing processes for an intracortical electrode array," *IEEE Trans Biomed Eng*, vol. 38, pp. 758-68, Aug 1991.
- [33] R. Bhandari, S. Negi, L. Rieth, and F. Solzbacher, "A Wafer-Scale Etching Technique for High Aspect Ratio Implantable MEMS Structures," *Sens Actuators A Phys*, vol. 162, pp. 130-136, Jul 2010.
- [34] C. Hassler, R. P. von Metzen, P. Ruther, and T. Stieglitz, "Characterization of parylene C as an encapsulation material for implanted neural prostheses," *J Biomed Mater Res B Appl Biomater*, vol. 93, pp. 266-74, Apr 2010.
- [35] S. F. Cogan, "Neural Stimulation and Recording Electrodes," *Annual Review of Biomedical Engineering*, vol. 10, pp. 275-309, 2008.
- [36] S. Negi, R. Bhandari, L. Rieth, R. W. Wagenen, and F. Solzbacher, "Neural electrode degradation from continuous electrical stimulation: Comparison of sputtered and activated iridium oxide," in *Journal of Neuroscience Methods*, pp. 8-17, 2010.

- [37] R. A. Lawes, A. S. Holmes, and F. N. Goodall, "The formation of moulds for 3D microstructures using excimer laser ablation," *Microsystem Technologies*, vol. 3, pp. 17-19, 1996.
- [38] M. Esashi, K. Minami, and S. Shoji, "Optical exposure systems for three-dimensional fabrication of microprobe," in *Micro Electro Mechanical Systems, 1991, MEMS '91, Proceedings. An Investigation of Micro Structures, Sensors, Actuators, Machines and Robots. IEEE*, pp. 39-44, 1991.
- [39] G. E. Loeb, R. A. Peck, and J. Martyniuk, "Toward the ultimate metal microelectrode," *J Neurosci Methods*, vol. 63, pp. 175-83, Dec 1995.
- [40] E. M. Schmidt, M. J. Bak, and P. Christensen, "Laser exposure of Parylene-C insulated microelectrodes," *J Neurosci Methods*, vol. 62, pp. 89-92, Nov 1995.
- [41] C. Yoonsu, O. C. Seong, R. H. Shafer, and M. G. Allen, "Highly inclined electrodeposited metal lines using an excimer laser patterning technique," in *Solid-State Sensors, Actuators and Microsystems, 2005. Digest of Technical Papers. TRANSDUCERS '05. The 13th International Conference on*, Vol. 2, pp. 1469-1472, 2005.
- [42] J.-M. Yoo, J.-I. Song, P. Tathireddy, F. Solzbacher, and L. W. Rieth, "Hybrid laser and reactive ion etching of Parylene-C for deinsulation of a Utah electrode array," *Journal of Micromechanics and Microengineering*, vol. 22, p. 105036, 2012.
- [43] G. E. Loeb, M. J. Bak, M. Salcman, and E. M. Schmidt, "Parylene as a chronically stable, reproducible microelectrode insulator," *IEEE Trans Biomed Eng*, vol. 24, pp. 121-8, Mar 1977.
- [44] J. B. Fortin and T. M. Lu, "A Model for the Chemical Vapor Deposition of Poly(para-xylylene) (Parylene) Thin Films," *Chemistry of Materials*, vol. 14, pp. 1945-1949, 2002.
- [45] R. Bhandari, S. Negi, L. Rieth, R. A. Normann, and F. Solzbacher, "A Novel Method of Fabricating Convolutd Shaped Electrode Arrays for Neuraland Retinal Prostheses," *Sens Actuators A Phys*, vol. 145-146, pp. 123-130, 2008.
- [46] A. Branner, R. B. Stein, and R. A. Normann, "Selective stimulation of cat sciatic nerve using an array of varying-length microelectrodes," *J Neurophysiol*, vol. 85, pp. 1585-94, Apr 2001.
- [47] W. L. Rutten, "Selective electrical interfaces with the nervous system," *Annu Rev Biomed Eng*, vol. 4, pp. 407-52, 2002.

- [48] D. L. Singleton, G. Paraskevopoulos, and R. S. Irwin, "XeCl laser ablation of polyimide: Influence of ambient atmosphere on particulate and gaseous products," *Journal of Applied Physics*, vol. 66, pp. 3324-3328, 1989.

CHAPTER 2

BACKGROUND AND STATE OF THE ART: TIP DEINSULATION AND ELECTROCHEMISTRY OF CHARGE INJECTION MATERIALS

2.1 Tip Deinsulation

2.1.1 Deinsulation Methods

The purpose of deinsulating the encapsulation material from microelectrode arrays is to generate the active electrode tips to acquire or stimulate neural signals from tissue. Early microelectrode deinsulation techniques used heating to melt the insulation or high-voltage discharges to ablate the material [1, 2]. The heating method led to the breakdown of the insulation adjacent to the deinsulated tip. The use of high voltage discharge degraded the adhesion of the Parylene adjacent to the tips and caused tiny fractures along the electrode shaft. This resulted in decreased impedance values that could degrade the encapsulation lifetime, selectivity, and increase cross talk between channels.

Another recently reported technique uses a diffusion-limited deposition (DLD) of Parylene on neural probes and can be used to generate unencapsulated electrode sites [3]. DLD technique makes use of a concentration gradient of precursor monomers during Parylene deposition between the inside and outside of a specially designed container with perforated lids through which the needle-like microelectrodes were placed. However, this

method is not appropriate for deinsulation of UEAs to get a controllable exposure and highly uniform impedance values of electrode tips because it needs specific containers for different types of electrode to be coated. Chemical etching is also a possibility, but is difficult to employ due to the inertness of the Parylene to most solvents. Dry etching (a.k.a reactive ion etching (RIE)) processes are currently considered the most suitable method to deinsulate Parylene, with the use of an oxygen plasma being most common [4-6].

Both photoresist and aluminum foil masks in conjunction with oxygen plasma etching have been investigated in UEA technology [7-9]. However, the use of a photoresist mask has been found to deteriorate the surface properties of Parylene-C during hard baking or the resist removal by acetone. Therefore, the use of aluminum foil mask and poking the electrode tips to the desired exposure length while deinsulating the Parylene has been adopted as a regular masking procedure in UEA technology. However, poking of aluminum electrodes is a time consuming process, and also has an inherent problem of nonuniformity and repeatability, leading to a large variation in the impedance values ($\sigma > 0.5 \text{ M}\Omega$). Moreover, the foil mask cannot be used for other electrode geometries like variable height electrodes, as introduced in Chapter 1.4.

2.1.2 Laser Beam Characteristics

Laser is an acronym for “Light Amplification by Stimulated Emission of Radiation”. The light is amplified through a stimulated-emission gain process in media, including solids, gases, and liquids, resulting in classes of lasers including solid states lasers, gas lasers, and dye lasers. The wide range of laser source from ultraviolet (UV) to

infrared (IR) enables micromachining of a variety of materials, including ceramic, metals, and polymers.

Several properties like wavelength, mode, and polarization determine the characteristics of a laser beam. The wavelength of a laser is determined by the transitions from the stimulated emission phenomenon. Even if lots of different wavelength lasers were developed, only a few of them, such as He-Ne, Nd:YAG, CO₂, and excimer lasers, are significant commercially in processing of material. The high spatial and temporal coherence allow a laser collimated to long distance with a narrow spectrum. Standing electromagnetic waves are formed by optical oscillation from a laser cavity geometry. The specific geometry of resonator determine a transverse standing wave as a mode of a beam. A variety of mode patterns is presented in Figure 2.1 and is denoted by TEM_{plq} (p is for radial zero field, l is for angular zero field, and q is for longitudinal zero field). The index (p, l) determines a spatial distribution as a transverse mode. The index q represents the number of axial mode under the same spatial distribution. The gain and loss are different between each transverse mode as different spatial distributions. Higher order of mode has more volume and a larger gain. However, it is harder to focus the beam because the laser beam is not from a virtual source.

2.1.3 Excimer Laser System

High-resolution features (a depth and spatial resolution are around the order of 0.1 μm and 1 μm, respectively) can be generated using an excimer laser for micromachining polymers. An excellent quality of MEMs features is enabled by the short wavelength (100 ~ 400 nm) in the ultraviolet region of the spectrum. The name “excimer” originated from excited dimer that exists very shortly as a molecule in an electronic excited state.

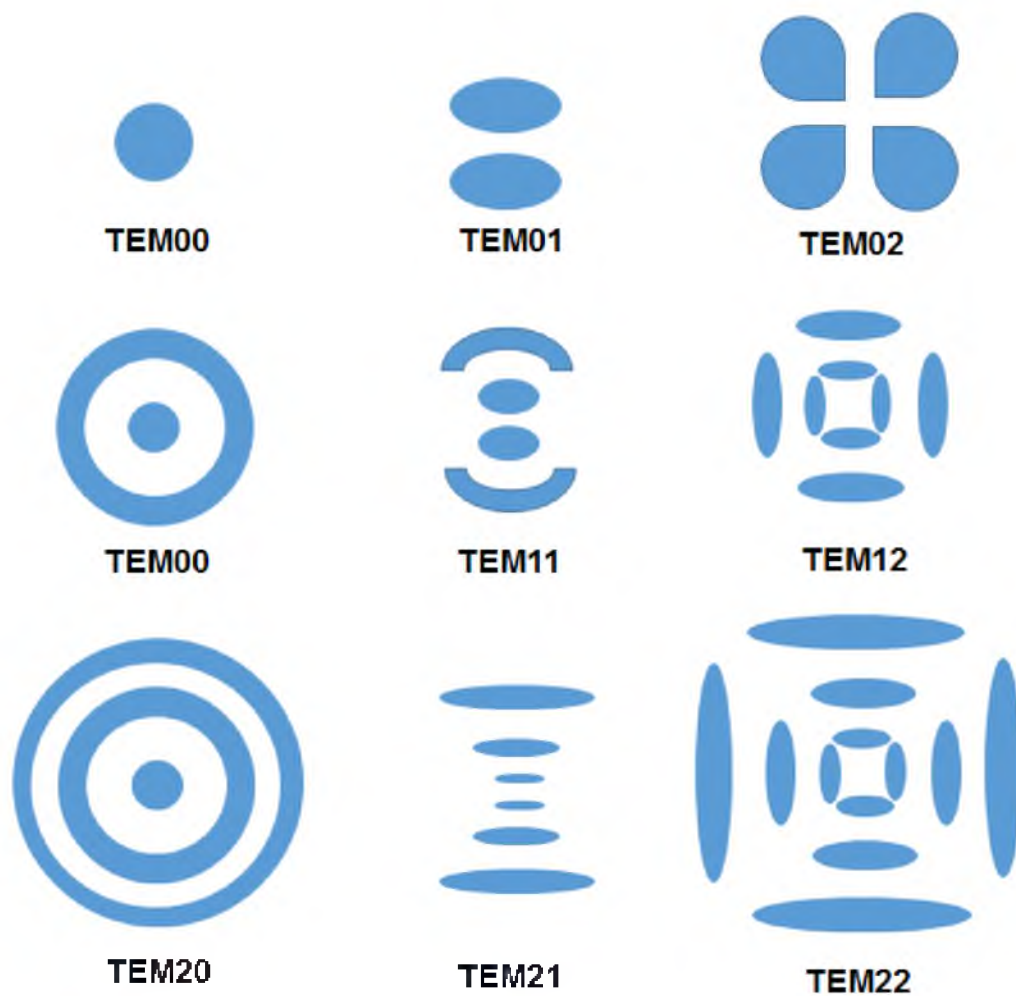


Fig 2.1. Various patterns of TEM mode.

When the excited dimer transits to the ground state, it divides into the individual atoms that are repelled from each other. The dissociation of excited molecules has a very short lifetime ($< \sim 10$ ns) and causes the stimulated emission of the laser. Widely used excimer lasers are krypton fluoride (KrF), argon fluoride (ArF), and xenon chloride (XeCl) which each have different wavelengths. The pumping of the ground state atoms to excited energy level is produced by an electric discharge through gas mixture with high excitation voltage (kV).

KrF excimer lasers have a relatively high photon energy (5 eV) which enables them to manufacture the microscale structure due to efficient ablation of material from the surface [10]. The schematic potential diagram of the KrF excimer laser is shown in Figure 2.2 [11]. The upper level in the diagram is a bound state populated with Kr^+ , F^- , and buffer gas (Ne or He). The minimum potential energy in the curve is unstable such that the excited dimer molecule; KrF^* collapses to the ground level; $\text{Kr} + \text{F}$ state with the occurrence of photon emission. The duration of the KrF^* state is less than a few

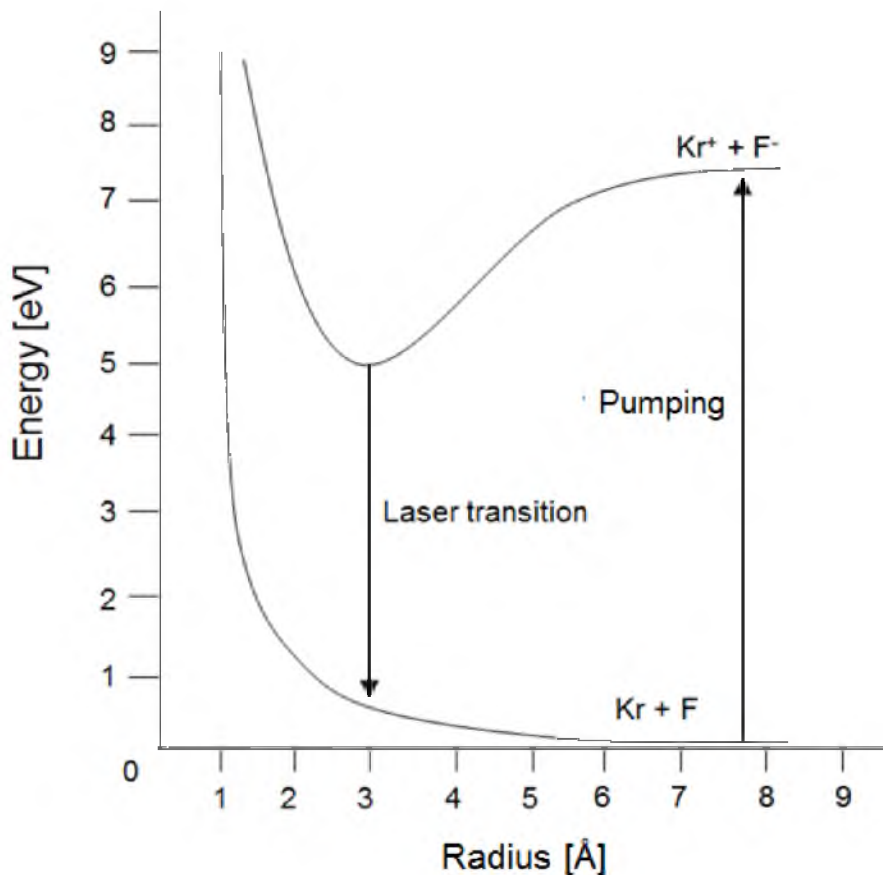


Fig 2.2. Schematic potential diagram of KrF excimer laser. The upper level in the diagram is a bound state populated with Kr^+ , F^- . The excited dimer molecule; KrF^* collapses to the ground level; $\text{Kr} + \text{F}$ state with the occurrence of photon emission.

nanoseconds and the unbounded Kr + F state is bonded covalently and separates Kr and F atoms. The gas discharge makes the lower state pump to the upper ionized energy state; $\text{Kr}^+ + \text{F}^-$. This excitation cycle is repeated continually for the excimer laser transition. KrF excimer lasers are useful for very sharp cutting without heat production because the energy of the short frequency in the ultraviolet region is high enough to break the chemical bonds of material and does not penetrate deeply into the surface of materials, which is suitable for the application of refractive surgery, micromachining, and microlithography.

2.1.4 Laser Deinsulation

Deinsulation using laser machining is an appropriate alternative to solve the challenges associated with aluminum foil mask followed by oxygen plasma deinsulation. Excimer lasers are the most applicable for deinsulation of Parylene-C due to their high resolution and power to remove the encapsulation without thermal effects on the substrate and adjacent material. However, one significant drawback of excimer laser ablation of Parylene is the residue and debris that accumulate on and adjacent to the ablation site. During the laser ablation process, photochemical breaking of bonds occurs with removal of Parylene [12]. These mechanisms can generate small molecular fragments which can accumulate in the form of residue on the surface [13, 14]. The fragments in UV ablation of polymers are combination of gaseous by-products (C_2 , CO, and CO_2) and fracturing of the long chains of the polymer molecules (monomer and oligomer).

Carbon residue from the laser ablation can increase the impedance and decrease the charge storage and charge injection capacities on the surface of the neural interface electrode because it exists on top of the metalized active material [15]. It can be removed

by laser illumination during the laser deinsulation process in case of a large tip exposure. When more fluence and number of pulse are irradiated on the electrode tip surface to get the large exposure area, there is more removal of carbon debris with less redeposition due to the laser power. But for neural interface applications [16, 17], small tip exposures on the order of tens of micrometers are needed to get selective electrical transduction. The relatively small tip area that can be generated by laser deinsulation is more influenced by the carbon residue due to lower flux on the electrode tip surface. Formation of these residues can be decreased significantly using vacuum [18], helium, or oxygen [19] controlled ambient relative to ablation in air. However vacuum, without any medium to push the debris into the exhaust, [18] cannot remove the debris thoroughly. Low Z shield gases (e.g., He) are the most effective methods to avoid momentum exchange with the surrounding atmosphere. Although helium or oxygen environment help to dramatically reduce the surface debris, residue is still present around the ablation sites [19, 20].

To minimize the formation of carbon residues, the laser flux needs to be high enough to efficiently remove the Parylene-C while not damaging the surface of the underlying material. For instance, the laser deinsulation of Parylene on gold makes it difficult to optimize the laser parameters (e.g., fluence and number of pulse) because of the difference of ablation threshold (a minimum fluence of laser to ablate the target material) between gold (255 mJ/cm^2) and Parylene (340 mJ/cm^2) for KrF excimer laser [15]. The difference of ablation threshold can bring about an incomplete ablation of encapsulation material resulting in degradation of impedance on active material. It is critical to select an underlayer that has a higher ablation threshold than the encapsulation to prevent damage to the active surface.

A schematic diagram of the KrF excimer laser system (Optec MicroMaster) used in this study is presented in Figure 2.3. It has x-y stage motion and a computer software for laser/stage control. The sample is fixed by vacuum chuck and the motion stage has $\sim 1 \mu\text{m}$ resolution in each direction. The 248 nm KrF laser can photoablate Parylene-C. The pulse duration for this system is $\sim 5 \text{ nsec}$ and the repetition rate of the pulsed mode laser was chosen between 100 and 200 Hz. The laser fluence [mJ/cm^2] is determined by selecting the output energy and demagnification. The laser beam goes through a mask (xy)

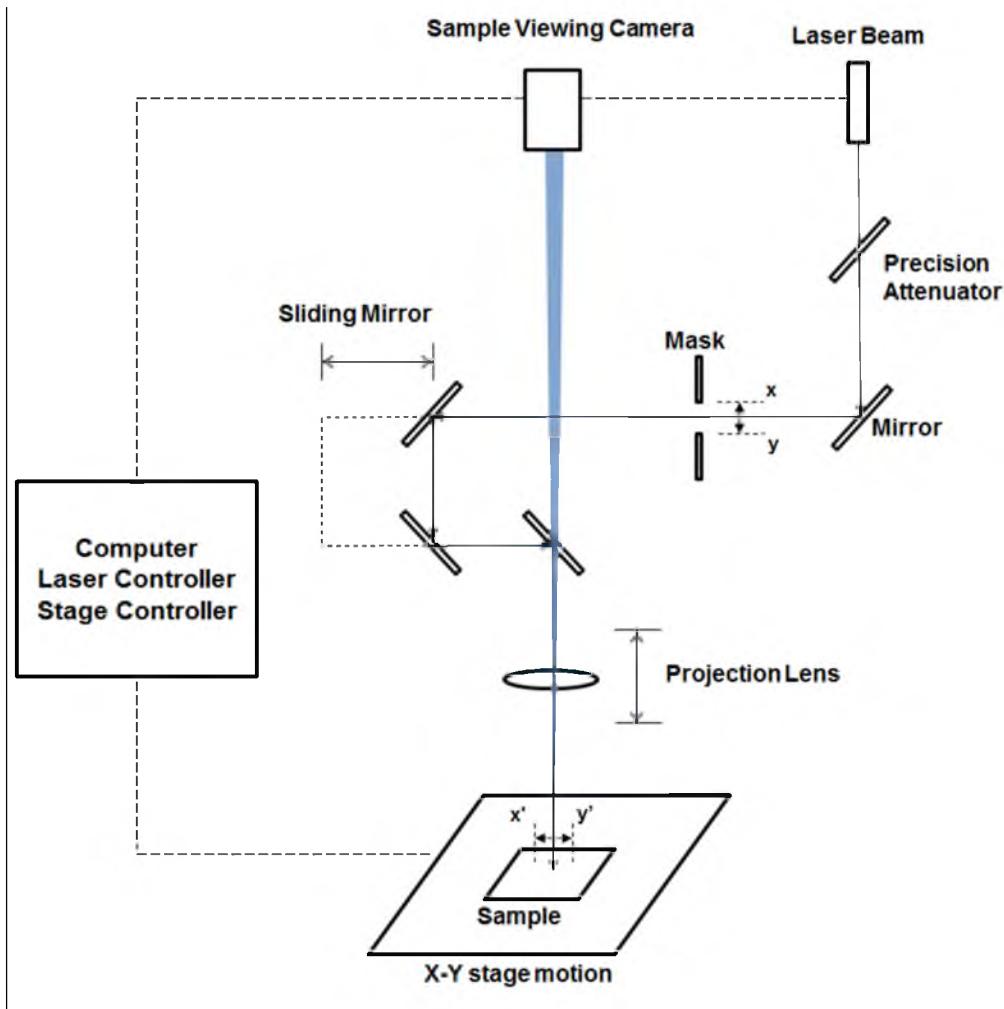


Fig 2.3. A schematic diagram of the laser ablation system is presented that highlights the motion stage, beam steering optics, and mask components.

and passes a projection lens which makes a demagnification image ($x'y'$) on the workpiece. The value of demagnification ranges from 3 to 11. The fixed value of the laser energy was 10 mJ and the intensity of the beam was adjusted by an optical attenuator. The roughly circular electrodes makes the use of a circular laser mask the most appropriate.

2.2 Electrochemistry of the Stimulating and Recording Microelectrode

2.2.1 The Electrode-Electrolyte Interface

There are charge transportation and electrochemical processes at the interface between the microelectrode and physiological solutions when a solid electrode is in the electrolyte. The electrochemical processes at this interface determines not only how this transport will occur, but also what chemical changes it will bring about to both the electrode and the electrolyte. Charge transport is through electrons (or holes) in electrodes, and is conducted through ions in electrolyte. In electrical recording, charge flows between the electrode and electrolyte, though high impedance amplifiers are used to minimize the current exchange in recording. The need to inject charge for functional electrical stimulation results in the need to exchange much greater levels of charge with the tissue. When an electrode is in an ionic solution, though a bias voltage is not applied, electrochemical reactions occur at the interface. The basic reactions are reduction and oxidation:



where O is the oxidant and R is the reductant. The reaction proceeds in one direction thermodynamically. Equilibrium conditions are reached as the reactions take place, reaching a condition where no current is transported across the interface and the reaction rate in forward and reverse directions is equal [21].

There are two mechanisms to keep a continuous net current flow across the interface. One is by capacitive current through the double layer formed by the excess charge on the electrode surface and a space charge layer in the solution. The other is by resistive current through Faradaic processes, in which charges are actually transferred between the electrode and the electrolyte, and chemical compositions in the electrode or solution are either oxidized or reduced [22].

2.2.2 Double Layer Charging

Double layer coupling between the electrode and electrolyte occurs due to the difference of charge carriers between electrode and electrolyte. Electrons cannot move in an electrolyte, and ions cannot move in a solid electrode. When the applying current is larger than a reaction rate across the interface, it builds an accumulation of charge in the boundary of the interface. Electrons build up at the electrode surface and ions build up in the electrolyte by making the double layer. This double layer behaves like an electrical capacitor. In the solution near the interface, the double layer can be further divided into several sublayers, as illustrated in Figure 2.4. The charge is covered in a flat sheet close to the electrode based on the Helmholtz model [21]. The surface of electrode is concentrated in a layer of adsorbed water molecules forming a hydration sheath called the Inner Helmholtz Plane (IHP). Hydrated ions with the opposite charge near the IHP form a layer called the Outer Helmholtz Plane (OHP). The two layers of water molecules make

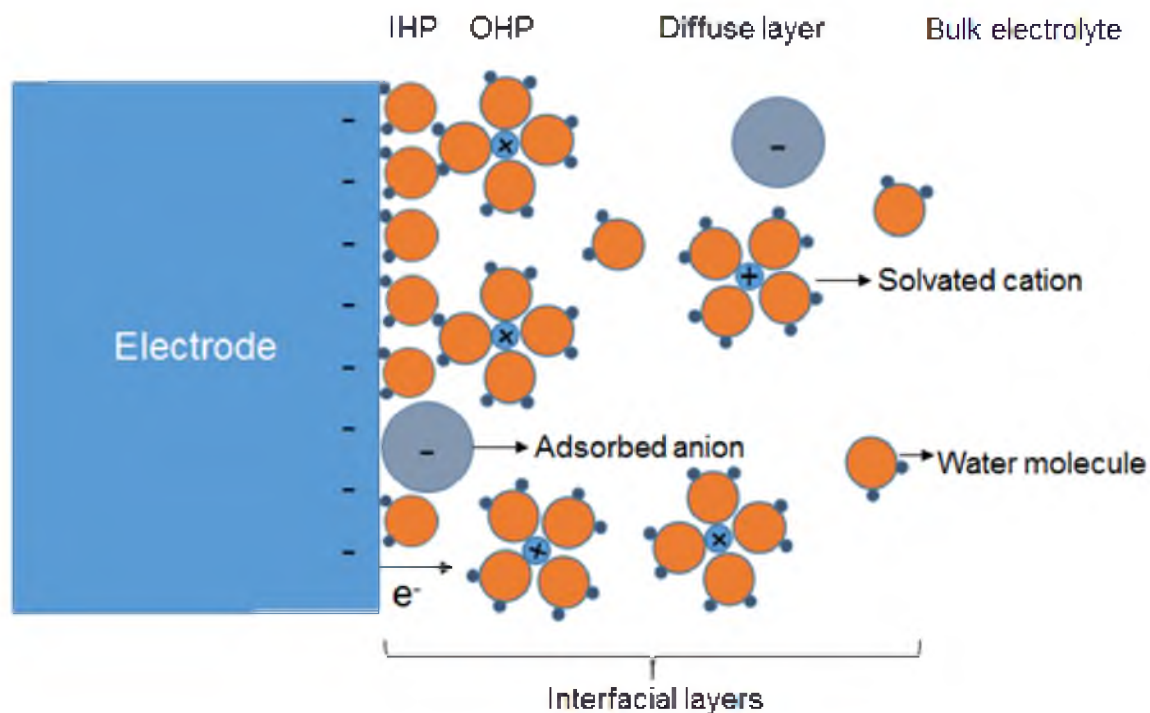


Fig 2.4. The surface layers formed when a metal electrode is immersed in an aqueous ionic solution. The double layer is formed by excess charge at the electrode surface and space charges (oriented water dipoles and ions). Electrons can also be transferred directly across the interface during Faradaic reactions [23].

the separation of charge. The diffuse layer is formed by a gradient of ion concentration from the OHP to the bulk electrolyte [23].

2.2.3 Faradaic Charging

The capacitance per unit area for iridium oxide like sputter deposited iridium oxide films (SIROFs) and activated iridium oxide films (AIROFs) ranges from 1 to 4 mF/cm² which is 100 times greater than the double layer capacitance of platinum or gold. The reason for this high capacitance is not the formation of a double layer, but presence of a Faradaic charge transfer mechanism. An electrode establishes contact with the surrounding environment, thereby transferring electrons across the electrode-electrolyte

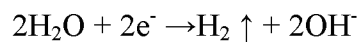
interface via oxidation and/or reduction reactions. All such charge-transfer processes are governed by Faraday's law (i.e., the amount of chemical change occurring at an electrode-electrolyte interface is directly proportional to the current that flows through that interface), and hence are called Faradaic processes. Electrodes at which Faradaic processes occur are also known as charge-transfer electrodes.

Both capacitive and Faradaic pathways can be used for neural stimulation. A major problem in the capacitive mechanism is that the current is usually small compared to the cell stimulation threshold. The capacitive charge injection ability can be increased by adding a thin insulating layer with high dielectric constant on the electrode surface; however, this usually is still not sufficient for neural application [24].

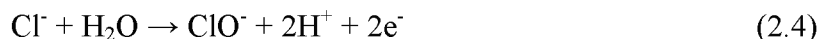
Faradaic reactions at the electrode-electrolyte interface can be divided into two categories: reversible reactions and irreversible reactions. One example of a reversible Faradaic reaction is the redox of iridium oxide:



In such reactions, the change made to the electrolyte or the electrode can be completely undone by reversing the direction of the current. Most common irreversible Faradaic processes include the electrolysis of water:



and the oxidation of chloride ions:



Irreversible reactions will significantly alter the chemical composition and *pH* of the electrolyte (i.e., the extracellular fluid), produce biologically toxic products, or corrode the electrode. This not only damages the electrodes, but also causes abnormalities in the neural function or the cell structure [25]. Therefore, irreversible Faradaic reactions are undesirable for neural stimulation.

2.3 Electrochemical Characterization of Microelectrode

2.3.1 Cyclic Voltammetry

Cyclic voltammetry (CV) is one of the key techniques used in electrochemistry research. Cyclic voltammetry can be used in quantitative investigations of equilibrium potentials, reaction rates, and absorption processes. Often, however, cyclic voltammetry is used qualitatively to get a general idea of what reactions and electrode processes are occurring in an electrochemical system. Cyclic voltammetry has a number of other uses. One is to measure the effective charge storage and charge transfer capabilities of an electrode. Another is to deposit materials onto an electrode surface and characterize the extent of such deposition. Repeated CV testing can also be used as a simple means of checking electrode stability.

Cyclic voltammetry is a controlled potential technique. In its simplest form, the potential is swept back and forth between two endpoints at a slow constant rate, typical around 50 mV/sec. Typical endpoints are about -0.6 and 0.8 V vs Ag|AgCl for iridium oxide that is bounded by the water window. This results in the application of a low-

frequency, large-amplitude triangular voltage waveform to the working electrode. A typical waveform is shown in Figure 2.5. The resulting current is recorded and plotted against the applied potential, generating a plot presented in Figure 2.6. This corresponds to an electrode that can undergo a single perfectly reversible action $R \leftrightarrow O + ne^2$, where O is the oxidized species and R is the reduced species. Positive current corresponds to the forward reaction. Electrons flow out of the working electrode. Electrons flowing out means that a positive current is flowing in. Negative current corresponds to the reverse reaction. As the voltage is swept from V_{min} to V_{max} and back again, the current follows on

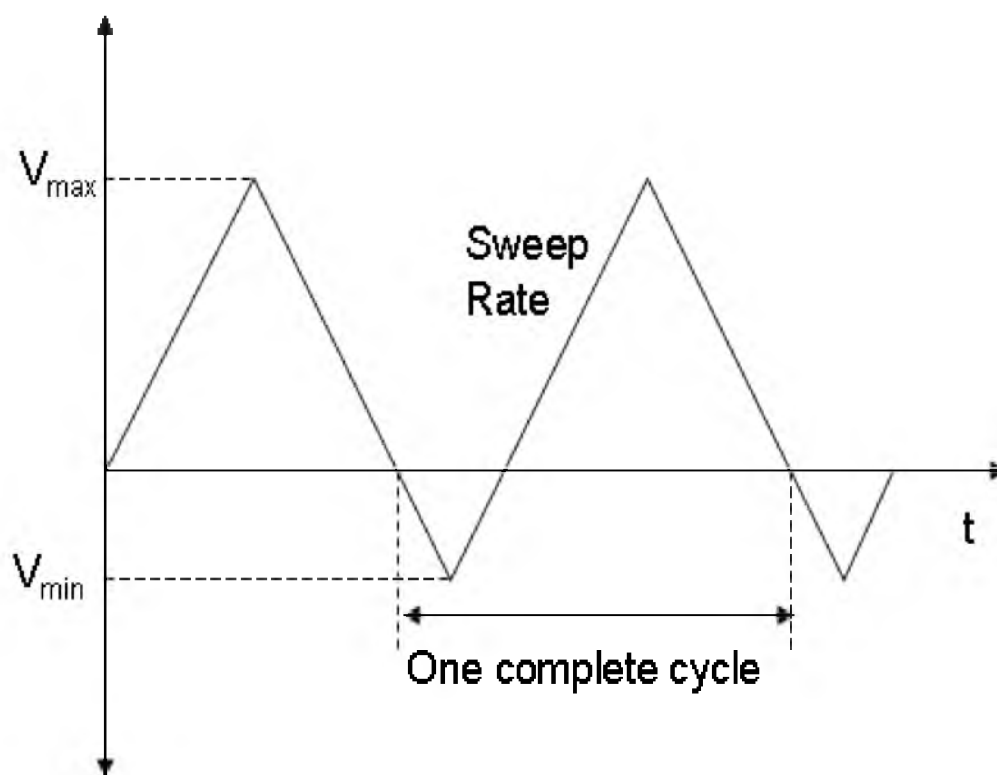


Fig 2.5. Potential waveform used in cyclic voltammetry. V is a triangular wave between V_{max} and V_{min} .

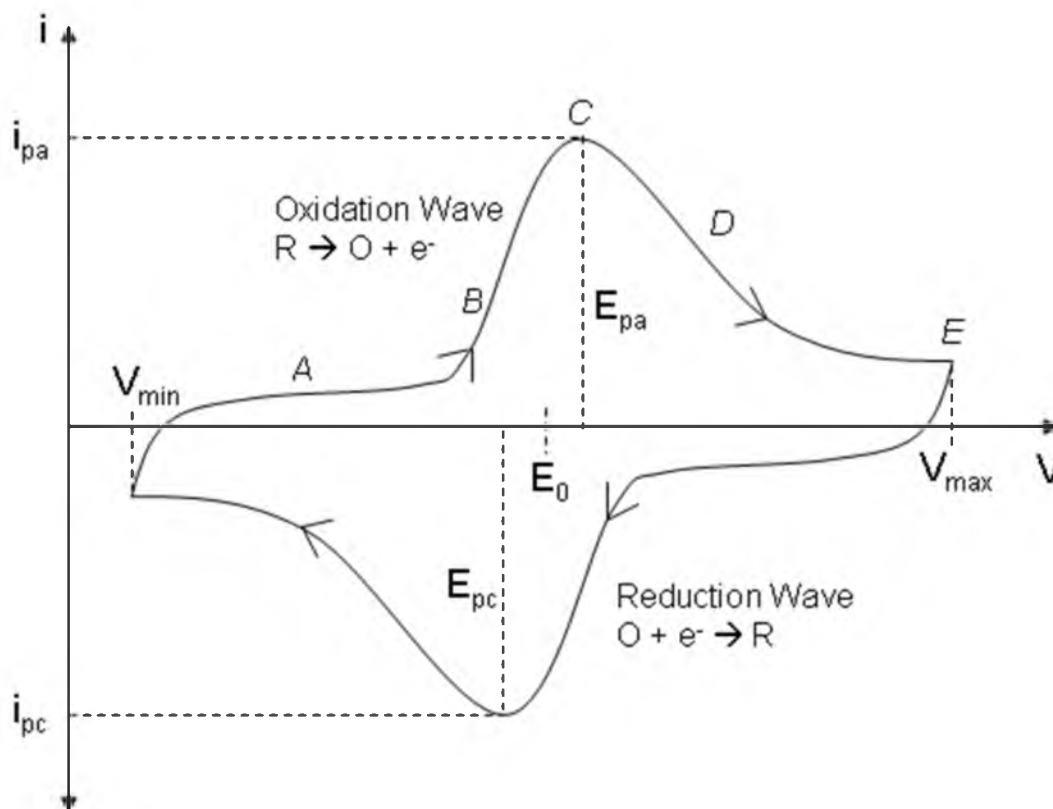


Fig 2.6. An example of a voltammogram is presented with some relevant features marked. As the voltage is swept from V_{min} to V_{max} and back again, the current follows the path with reduction and oxidation.

the path shown in Figure 2.6, moving in the direction of the arrows. Starting near A, the current increases more and more rapidly as it approaches the formal potential $E^{0'}$. Near B, the rise in current begins to slow down, reaching a peak at C. The current continues to decay as it goes through region D. Eventually, the potential reaches V_{max} at point E, the sweep direction reverses, and similar behavior is seen for the negative direction. The number of cycles that are run depends on the application and the amount of time available.

Voltammograms contain a lot of complex information and can be particularly difficult to interpret if multiple reactions are occurring. The waveforms seen with cyclic voltammetry are a clear indication that even the simplest electrodes involve much more than linear resistance and capacitance terms.

In general, the most prominent features of a cyclic voltammogram are due to mass transport and chemical reactions, the very features simple electrical models tend to approximate or ignore [21]. The double layer capacitance and series resistance do show up in the observed waveforms, but their effect is usually small and often treated as an unwanted distortion. By assuming simple models for mass transport and reactant concentrations at the electrode surface, it is possible to derive analytical expressions for the observed peak shapes. The theory and interpretation of cyclic voltammetry data is a widely researched and a deep topic.

The charge storage capacity (CSC) is calculated from a voltammogram by integrating the current with respect to time for either the positive or negative sweep. In most cases, it is then divided by the area of the electrode for easier comparison between samples. The voltage limits for iridium oxide used in the voltammogram are typically just the water window, about -0.6 V and 0.8 V vs Ag|AgCl. If the electrode will only be operated in a specific voltage regime, then it may be desirable to choose other voltage limits for the CSC calculation. The CSC is directly dependent on both the voltage limits and sweep rate; therefore, one must use a consistent measurement protocol for comparison to be useful. The CSC is useful as it represents the maximum amount of charge that can be transferred by the electrode while remaining in a set potential window. Since thicker oxide layers in iridium oxide tend to source more current [22], it has

become a popular way to judge the extent of oxide growth during formation processes. A good iridium oxide electrode will have a CSC of around 30 mC/cm^2 [26, 27]. The charge capacity is measured with the slow sweep rate (50 mV/s) and only a small fraction of it can be safely accessed with typical high-frequency stimulation ($< 1 \text{ kHz}$) because porous electrodes with high electrochemical surface area (ESA) / geometric surface area (GSA) ratio and pore geometry of an electrode in electrolyte form a delay-line with a time-constant during the high-frequency stimulation [22].

A CV plot comparing Ir and activated IrO_x to compare the double layer and Faradaic charging is shown in Figure 2.7. In the voltammogram of the activated Ir, there is a main current peak at 0.25 V in the positive voltage region and -0.21 V in the negative voltage region. It represents the reversible redox reactions between Ir^{3+} and Ir^{4+} .

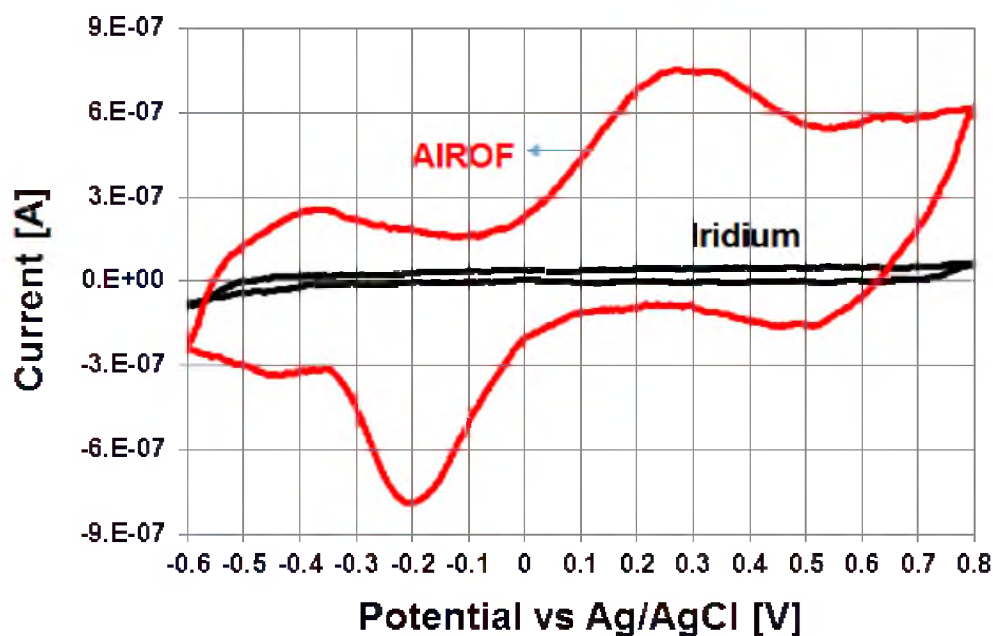


Fig 2.7. Cyclic voltammograms of an Ir and AIROF are presented from planar electrodes with $300 \mu\text{m}$ diameter circle. The CSC_c of Ir and AIROF is 3.5 mC/cm^2 and 10 mC/cm^2 , respectively. The sweep rate was 50 mV/s [28].

On the other hand, the CV of rectangular shape without any redox reactions in Ir shows a capacitive charging of double layer transduction mechanism. The cathodic charge storage capacity (CSCc) of Ir and activated Ir is calculated as 3.5 mC/cm^2 and 10 mC/cm^2 , respectively, by integration of the current with respect to time in the cathodic current region. The higher value of CSCc in activated Ir is by the Faradaic charging mechanism through redox reactions. More details about the experimental methods and results are in Chapter 5.

2.3.2 Electrochemical Impedance Spectroscopy

Electrochemical impedance spectroscopy (EIS) studies an electrode's complex impedance over a wide range of AC frequencies. An electrode is biased at some potential, usually its open circuit potential, and a small sinusoidal potential variation is applied. The magnitude and phase of the resulting current variation is measured. This is repeated over a range of frequencies, typically 1 Hz to 10^5 Hz by a frequency step, building up a spectrum, or generated using a multisine excitation [29].

Impedance spectroscopy is in some ways the polar opposite of cyclic voltammetry. Both are controlled potential techniques, but whereas cyclic voltammetry is large-signal and low frequency, EIS is small-signal and high frequency. As a result, they provide completely different types of information about an electrode. Cyclic voltammetry focuses on the specifics of mass transport and chemical reactions, while impedance spectroscopy abstracts these away and focuses more on the electrical domain. EIS spectra are valuable in assessing the recording capabilities of microelectrodes. EIS can be used to investigate both tissue and electrode properties. The resistive contribution of tissue conductivity to the overall electrode impedance is estimated from the impedance measured at high

frequency, where the contribution to the impedance due to charge transfer at the electrode-tissue interface is negligible.

Impedance spectra are typically displayed as either Bode plots or Nyquist plots. Each has its uses in analyzing electrode behavior. Examples of both plots are presented in Figure 2.8. An equivalent circuit with one time constant in Figure 2.8 (a) leads to a Nyquist plot as shown in Figure 2.8 (b) and a Bode plot as shown in Figure 2.8 (c). In a Bode plot, the log magnitude and the phase of the impedance are graphed versus the log frequency. Bode plots prove useful in model fitting and providing rough impedance

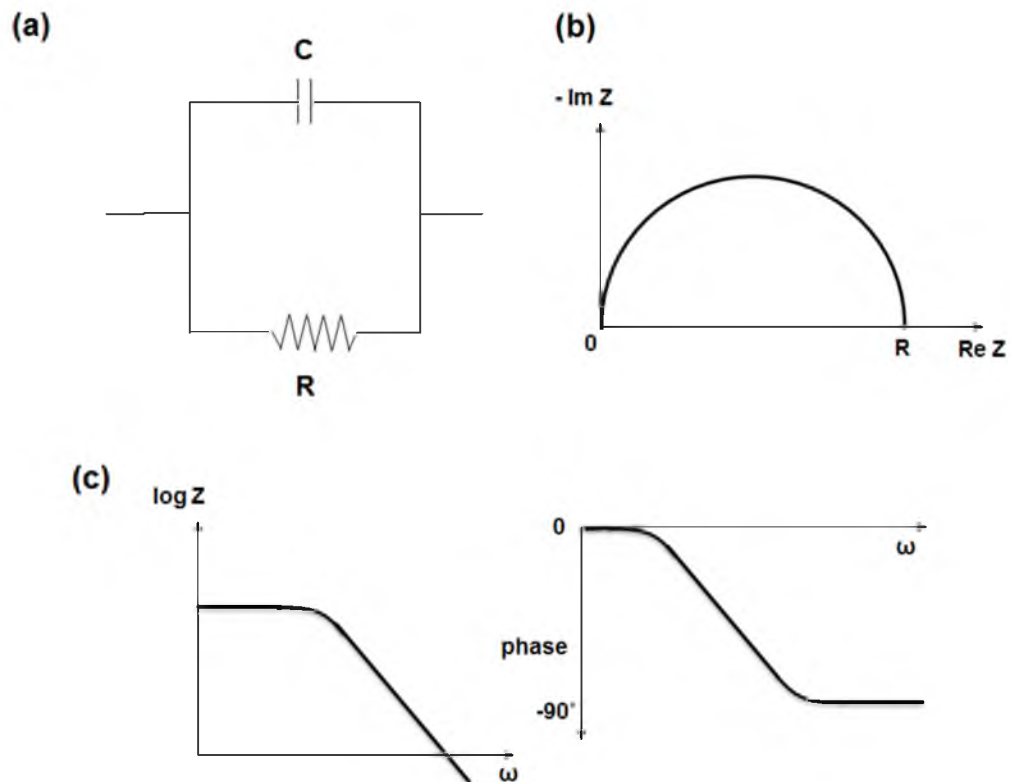


Fig 2.8 An example of (a) equivalent circuit of one time constant, (b) Nyquist plot of circuit (a), and (c) Bode plot of circuit (a).

estimates. In the Nyquist plot, the real and imaginary parts of the impedance are plotted against each other in which the imaginary part of the impedance is plotted on the Y-axis vs. the real part on the X-axis. Nyquist plot are commonly used to identify which circuit model would best fit the observed data. A quick glance at the features in a Nyquist plot can reveal which model element dominates the behavior of the electrode.

2.3.3 Potential Transient

The potential transient method is used to derive a maximum quantity of injected charge in a stimulation pulse within the water window. The charge injection capacity (CIC) is an important indication for the selection of the active surface material in the microelectrode array. A higher CIC is desirable for using smaller electrodes to increase selectivity, while maintaining the ability to deliver sufficient charge for stimulation. An equivalent circuit model of the electrode-electrolyte interface for iridium oxide is shown in Figure 2.9, in which R_s is the electrolyte resistance, R_{ct} is the charge transfer resistance, and the CPE is a constant phase element. Due to the nonideal capacitance response at many electrode-electrolyte interfaces, a CPE can be used instead of the ideal capacitor. The CPE impedance is given by $Z_{CPE} = (A(i\omega)^\alpha)^{-1}$, where ' ω ' is the angular frequency, ' A ' and ' α ' are frequency-independent parameters, and $0 \leq \alpha \leq 1$. The CPE indicates an ideal capacitor for $\alpha = 1$ and an ideal resistor for $\alpha = 0$ [30].

The simplest case is to imagine an electrode model with only a resistor and capacitor in series. In response to a square current pulse, the observed waveform will start with a sharp step in voltage equal to iR_s . This will be followed by an exponential ramp that can be approximated as a straight ramp for short time periods with slope i/C_{dl} (C_{dl} : double layer capacitance) as long as the current is applied. At the end of the pulse, the

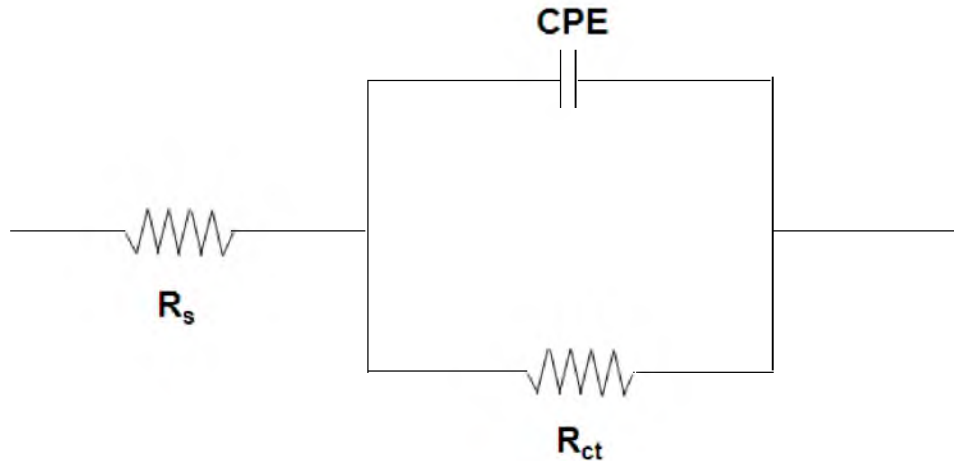


Fig 2.9. Equivalent circuit of the electrode-electrolyte systems. R_s is the electrolyte resistance, R_{ct} is the charge transfer resistance, and the CPE is a constant phase element.

voltage will decrease back down by the original voltage, leaving a net voltage of i/C_{dl} on the capacitor.

If the charge transfer resistance is included, the behavior is slightly more complex. The initial step will be the same, but instead of a straight ramp, the voltage will exponentially approach $iR_s + iR_{ct}$ with time constant $R_{ct}C_{dl}$. Analytical results can be derived for more complex systems of resistors and capacitors using well-known techniques in circuit theory.

In most cases, it is better to make electrochemical measurements with a three electrode cell, but for chronically implanted electrodes, using a true reference electrode is simply not feasible [31]. This is rarely a problem, since most stimulators are current controlled devices and designed to generate a response, not measure electrochemical properties. Even without a reference, well-defined voltage can still be measured across the working and return electrodes. From an electrochemical perspective, this is a

suboptimal system in which to do modeling. However, it is exactly this lack of precise control that must be dealt with and accounted for in a real device.

In this study, current pulses were delivered as charge-balanced biphasic pairs, cathodal first, with equal times and current amplitude for each phase to measure CIC. The CIC is the magnitude of charge per unit area (mC/cm^2) without a damage of the electrode. The biphasic pulse-width of $500 \mu\text{s}$ was used for the charge injection of unbiased SIROF and AIROF planar electrodes and UEAs. As the parameters are defined in Figure 2.10, the max negative potential excursion (E_{mc}) was calculated by subtracting the access voltage (V_a) from the maximum negative voltage in the transient. V_a is equal to iR_s drop and associated with the saline resistance. E_{mc} is also equal to the potential immediately after the end of the cathodic pulse when V_a is zero. The CIC was derived from multiplying stimulation current and pulse width at which the potential (E_{mc}) reaches water reduction potential (-0.6 V) divided by the surface area [22, 30]. More details about experimental methods and results are described in Chapter 5 and 6.

2.4 Iridium Oxide as Electrode Material

2.4.1 Considerations in Material Selection

Degradation of the electrode material during electrical stimulation can occur, particularly if the stimulation voltages exceed the water window [32]. The electrode material also degrades through exposure to the *in-vivo* environment for recording electrodes. Although ideally polarizable electrodes can create the stimulation with no chemical changes at the electrode-tissue interface, commonly used metallic electrodes such as platinum have the charge injection limited to less than $100 \sim 300 \mu\text{C}/\text{cm}^2$ of true surface area without using porous structure for high roughness or additional coating of

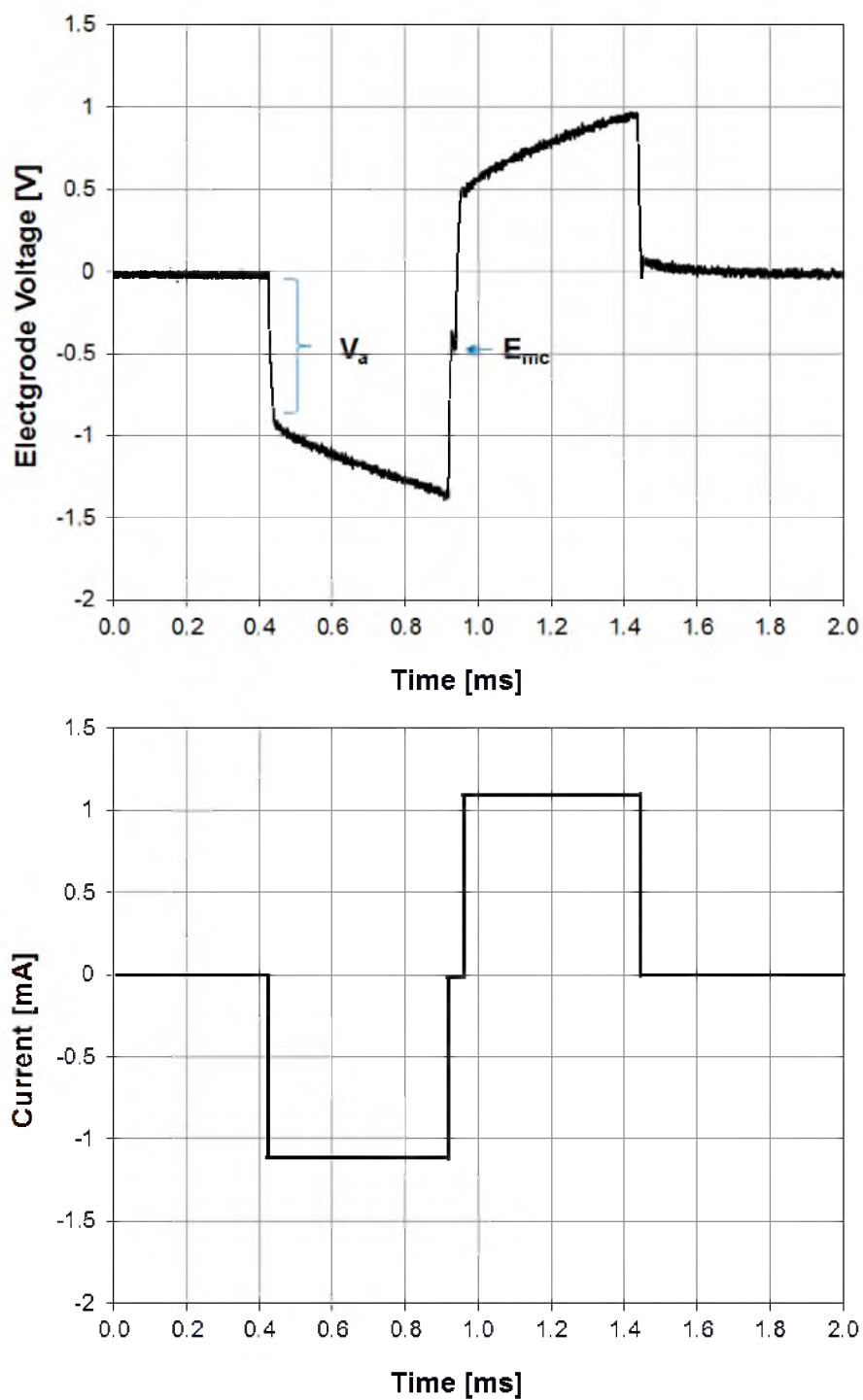


Fig 2.10. Potential transient of the SIROF planar electrode shows access voltage (V_a) and maximum cathodic (E_{mc}) potential excursions during a constant current biphasic pulse. The current pulse amplitude and width per phase is 1.2 mA and 500 μ s, respectively.

high dielectric film [22, 24, 33]. Platinum electrodes, like many other metal electrodes, can be used only as low current density electrodes. However, typical clinical applications in the central nervous system require higher charge injection with small electrode areas. For instance, a retinal implant requires the smaller ($\sim 10 \mu\text{m}$) and highly dense electrodes. Hence, stimulation electrodes with Faradaic charge transfer mechanisms can fulfill the requirements due to their high charge injection ($> 300 \mu\text{C}/\text{cm}^2$). Iridium oxide provides a significant enhancement of charge injection capacity through a valence transition for the Faradaic reaction.

An important consideration in selection of electrode material for use with laser deinsulation is the susceptibility of the material to degradation by laser irradiation. Materials have different values for their laser ablation threshold. The threshold of Parylene-C made in this study was around $250 \text{ mJ}/\text{cm}^2$. A more robust deinsulation process needs an electrode site material that has a higher ablation threshold than the encapsulation material. Iridium oxide thin films do not have a high resistance to laser power during the ablation of Parylene-C because it has relatively small ablation threshold ($< 700 \text{ mJ}/\text{cm}^2$). The damage resistance of IrO_x needs to be improved, or the deinsulation process altered to prevent damage to the electrode sites.

2.4.2 Iridium Oxide

Iridium oxide that is used in this study is one of most attractive electrode materials because it has a high charge injection capacity to facilitate stimulation applications. IrO_2 has a rutile-like structure containing six coordinate iridium and three coordinate oxygen, as shown in Figure 2.11. Rutile is the common mineral form of

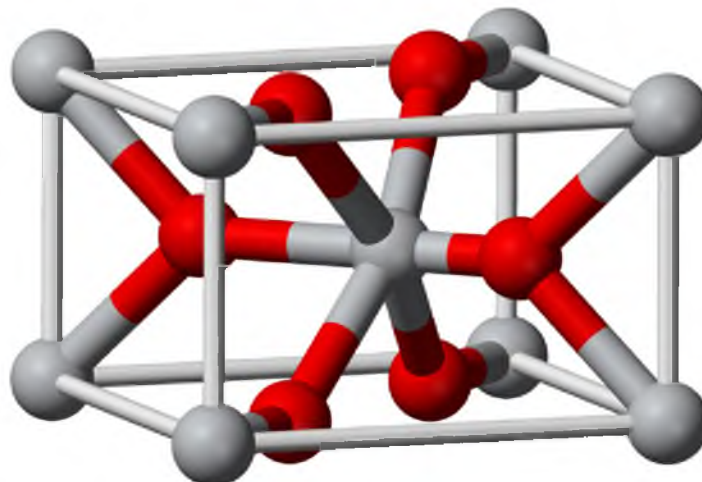


Fig 2.11. The unit cell of the Rutile structure of iridium oxide (IrO_2) is presented. The silver balls represent Ir, and the red balls represent oxygen.

titanium dioxide. When grown or deposited on an electrode, iridium oxide is amorphous, forming chains and networks of iridium centers [34-36]. The iridium atoms in the film can exist in several different oxidation states. The +3 and +4 states are most stable, but others can be present as well. Bound to the iridium atoms are coordinated hydroxide and water molecules, some of which act as links between the iridium centers. The bound molecules can rearrange themselves in many different ways through rapid chemical reactions. The interface between the microelectrode and physiological solution is important because the charge transportation as electrochemical processes takes place and exerts a direct influence on the electrode performance.

Reduction and oxidation reaction take place in the iridium oxide. One possibility is for an electron to be transferred from the underlying metal to an iridium atom in oxide. Another possibility is for an electron to be transferred between two nearby iridium atoms. Both involve changing the oxidation of one or more iridium atoms between the + 3 and + 4 states. At high potentials, iridium atoms in the oxide favor the +4 state, at lower

potentials, the + 3 state is preferred. At equilibrium, one would expect there to be a direct relationship between the concentration of atoms in each state and the applied potential. In order to change the potential in the film, one must convert iridium atoms between the two states. This requires a definite amount of charge. A diagram of redox process in iridium oxide and the equations of chemical reaction are shown in Figure 2.12.

Hydrated iridium oxide films have complex microscopic structures that are highly dependent on how the film was created. When produced by iridium metal activation, AIROF, the film grows as a series of thin sheets. With each potential cycle, a new layer is formed at the metal/oxide interface [26, 27]. Since each layer is formed by oxidizing a pre-existing electrode surface, the structure of the film will be strongly influenced by the crystal structure and surface morphology of the underlying metal. As the film grows, it can develop cracks and pores, some of which are quite large and cause surface flaking [37]. Direct use of AIROF in laser deinsulation is difficult because the laser ablation of Parylene-C can cause damage on the AIROF surface due to low ablation

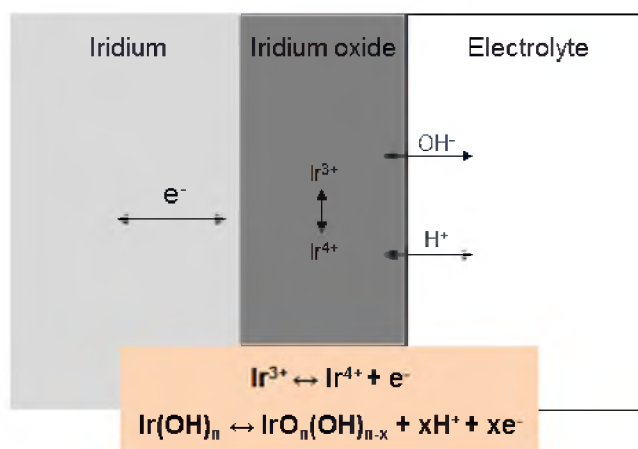


Fig 2.12. Faradaic reaction of iridium oxide film is presented with the equations of chemical reaction. The reversible Faradaic reaction involves reduction and oxidation as the valence transition between Ir^{3+} and Ir^{4+} state of the iridium oxide.

threshold of AIROF ($< 700 \text{ mJ/cm}^2$) that is close to that of Parylene-C ($\sim 250 \text{ mJ/cm}^2$). The ability of conversion from Ir to AIROF makes it possible to use the activated Ir through a slight tuning of the deinsulation process. The laser deinsulation of Parylene on iridium and subsequent electrochemical activation of the iridium can be the alternative to use the AIROF with high charge injection ability, though this is not compatible with wireless-type UEA due to its inability to activate the iridium through pads.

Another method of depositing oxide films is by reactively sputtering them onto a substrate from an iridium target [38-40]. These films have cyclic voltammetric and charge injection properties comparable to those of AIROF even if it is affected by sputtering process parameters like deposition pressure, substrate bias, sputtering gas composition, and sputtering gas composition, etc. [41]. The low laser ablation threshold of SIROF, comparable to AIROF, makes it more challenging to directly make use of as-deposited SIROF with the laser deinsulation technique. A method of partial deoxidation of SIROF using an annealing process which enables the use of SIROF with high charge injection capacity was developed, as is presented in Chapters 5 and 6.

The effective capacitance of iridium oxide is determined primarily by the number and accessibility of the redox centers and its susceptible to limiting charge injection densities due to the shape or type of stimulation waveform. For example, when subjected to a predominantly cathodal pulse of 0.2 msec, the electrode can inject only 1 mC/cm^2 . However, the electrode can inject almost 3.5 mC/cm^2 when the cathodal pulses are interspersed with an anodic bias voltage. The anodic bias voltage returns the electrode/oxide to its highest stable valence state between treatments, thereby increasing the charge injection ability of the electrode [42, 43]. Also, transport and conductivity

limitations during the short treatment timeframes restrict the utilization of the large charge injection capacity of such electrodes.

2.5 References

- [1] G. E. Loeb, M. J. Bak, M. Salcman, and E. M. Schmidt, "Parylene as a Chronically Stable, Reproducible Microelectrode Insulator," *Biomedical Engineering, IEEE Transactions on*, vol. BME-24, pp. 121-128, 1977.
- [2] J. B. Fortin and T. M. Lu, "A Model for the Chemical Vapor Deposition of Poly(para-xylylene) (Parylene) Thin Films," *Chemistry of Materials*, vol. 14, pp. 1945-1949, 2002.
- [3] R. P. von Metzen, N. Lass, P. Ruther, and T. Stieglitz, "Diffusion-Limited Deposition of Parylene C," *Microelectromechanical Systems, Journal of*, vol. 20, pp. 239-250, 2011.
- [4] E. Meng, P.-Y. Li, and Y.-C. Tai, "Plasma removal of Parylene C," *Journal of Micromechanics and Microengineering*, vol. 18, p. 045004, 2008.
- [5] J. M. Hsu, L. Rieth, R. A. Normann, P. Tathireddy, and F. Solzbacher, "Encapsulation of an integrated neural interface device with Parylene C," *IEEE Trans Biomed Eng*, vol. 56, pp. 23-9, Jan 2009.
- [6] A. J. Spence, K. B. Neeves, D. Murphy, S. Sponberg, B. R. Land, R. R. Hoy, *et al.*, "Flexible multielectrodes can resolve multiple muscles in an insect appendage," *J Neurosci Methods*, vol. 159, pp. 116-24, Jan 15 2007.
- [7] P. K. Campbell, K. E. Jones, R. J. Huber, K. W. Horch, and R. A. Normann, "A silicon-based, three-dimensional neural interface: manufacturing processes for an intracortical electrode array," *IEEE Trans Biomed Eng*, vol. 38, pp. 758-68, Aug 1991.
- [8] J. Ji, F. E. H. Tay, J. Miao, and C. Iliescu, "Microfabricated microneedle with porous tip for drug delivery," *Journal of Micromechanics and Microengineering*, vol. 16, p. 958, 2006.
- [9] R. Bhandari, S. Negi, L. Rieth, R. A. Normann, and F. Solzbacher, "A novel masking method for high aspect ratio penetrating microelectrode arrays," *Journal of Micromechanics and Microengineering*, vol. 19, p. 035004, 2009.
- [10] H. Sato and S. Nishio, "Polymer laser photochemistry, ablation, reconstruction, and polymerization," *Journal of Photochemistry and Photobiology C: Photochemistry Reviews*, vol. 2, pp. 139-152, 2001.

- [11] D. Basting, K. Pippert, and U. Stamm, "History and future prospects of excimer laser technology," *RIKEN Review*, vol. 43, pp. 14-22, 2002.
- [12] J. C. Miller and R. F. Haglund, *Laser ablation and desorption* vol. 30: Academic Press, 2009.
- [13] D. L. Singleton, G. Paraskevopoulos, and R. S. Irwin, "XeCl laser ablation of polyimide: Influence of ambient atmosphere on particulate and gaseous products," *Journal of Applied Physics*, vol. 66, pp. 3324-3328, 1989.
- [14] R. Srinivasan and B. Braren, "Ultraviolet laser ablation of organic polymers," *Chemical Reviews*, vol. 89, pp. 1303-1316, 1989.
- [15] O. R. Musaev, P. Scott, J. M. Wrobel, J. A. Wolf, and M. B. Kruger, "UV laser ablation of parylene films from gold substrates," *Journal of Materials Science*, vol. 46, pp. 183-187, 2011.
- [16] A. Branner, R. B. Stein, and R. A. Normann, "Selective Stimulation of Cat Sciatic Nerve Using an Array of Varying-Length Microelectrodes," *Journal of Neurophysiology*, vol. 85, pp. 1585-1594, 2001.
- [17] W. L. C. Rutten, "Selective electrical interfaces with the nervous system," *Annual Review of Biomedical Engineering*, vol. 4, pp. 407-452, 2002.
- [18] J. R. Lankard, Sr., and G. Wolbold, "Excimer laser ablation of polyimide in a manufacturing facility," *Applied Physics A*, vol. A 54, pp. 355-359, 1992.
- [19] J. H. Brannon, J. R. Lankard, A. I. Baise, F. Burns, and J. Kaufman, "Excimer laser etching of polyimide," *Journal of Applied Physics*, vol. 58, pp. 2036-2043, 1985.
- [20] S. Kuper and J. Brannon, "Ambient gas effects on debris formed during KrF laser ablation of polyimide," *Applied Physics Letters*, vol. 60, pp. 1633-1635, 1992.
- [21] A. J. Bard, *Electrochemical methods : fundamentals and applications*, 2nd ed.: New York : Wiley, 2001.
- [22] S. F. Cogan, "Neural Stimulation and Recording Electrodes," *Annual Review of Biomedical Engineering*, vol. 10, pp. 275-309, 2008.
- [23] Z. Ahmad and D. Macdonald, *Principles of Corrosion Engineering and Corrosion Control, Second Edition*: Elsevier Science, 2012.
- [24] T. L. Rose, E. M. Kelliher, and L. S. Robblee, "Assessment of capacitor electrodes for intracortical neural stimulation," *Journal of Neuroscience Methods*, vol. 12, pp. 181-193, 1985.

- [25] S. B. Brummer and M. J. Turner, "Electrochemical Considerations for Safe Electrical Stimulation of the Nervous System with Platinum Electrodes," *Biomedical Engineering, IEEE Transactions on*, vol. BME-24, pp. 59-63, 1977.
- [26] J. D. Weiland, "Electrochemical Properties of Iridium Oxide Stimulating Electrodes," PhD thesis, University of Michigan, 1997.
- [27] J. D. Weiland and D. J. Anderson, "Chronic neural stimulation with thin-film, iridium oxide electrodes," *IEEE Trans Biomed Eng*, vol. 47, pp. 911-8, Jul 2000.
- [28] J.-M. Yoo, S. Negi, P. Tathireddy, F. Solzbacher, J.-I. Song, and L. W. Rieth, "Excimer laser deinsulation of Parylene-C on iridium for use in an activated iridium oxide film-coated Utah electrode array," *Journal of Neuroscience Methods*, 2013, in press.
- [29] A. Lasia, "Electrochemical Impedance Spectroscopy and its Applications," in *Modern Aspects of Electrochemistry*. vol. 32, B. E. Conway, J. O. M. Bockris, and R. White, Eds., ed: Springer US, pp. 143-248, 2002.
- [30] S. Negi, R. Bhandari, L. Rieth, and F. Solzbacher, "In vitro comparison of sputtered iridium oxide and platinum-coated neural implantable microelectrode arrays," *Biomedical Materials*, vol. 5, p. 015007, 2010.
- [31] M. W. Shinwari, D. Zhitomirsky, I. A. Deen, P. R. Selvaganapathy, M. J. Deen, and D. Landheer, "Microfabricated Reference Electrodes and their Biosensing Applications," *Sensors*, vol. 10, pp. 1679-1715, 2010.
- [32] S. Negi, R. Bhandari, L. Rieth, R. Van Wagenen, and F. Solzbacher, "Neural electrode degradation from continuous electrical stimulation: comparison of sputtered and activated iridium oxide," *J Neurosci Methods*, vol. 186, pp. 8-17, Jan 2010.
- [33] T. L. Rose and L. S. Robblee, "Electrical stimulation with Pt electrodes. VIII. Electrochemically safe charge injection limits with 0.2 ms pulses," *IEEE Trans Biomed Eng*, vol. 37, pp. 1118-20, Nov 1990.
- [34] S. H. Glarum and J. H. Marshall, "The A-C Response of Iridium Oxide Films," *J. Electrochem. Soc.*, vol. 127, pp. 1467-1474, 1980.
- [35] L. D. Burke and D. P. Whelan, "A new interpretation of the charge storage and electrical-conductivity behavior of hydrous iridium oxide," *J. Electroanal. Chem.*, vol. 124, pp. 333-337, 1981.
- [36] L. D. Burke and D. P. Whelan, "A voltammetric investigation of the charge storage reactions of hydrous iridium oxide layers," *Journal of Electroanalytical Chemistry and Interfacial Electrochemistry*, vol. 162, pp. 121-141, 1984.

- [37] V. Birss, R. Myers, H. Angerstein-Kozłowska, and B. E. Conway, "Electron Microscopy Study of Formation of Thick Oxide Films on Ir and Ru Electrodes," *J. Electrochem. Soc.*, vol. 131, pp. 1502-1510, 1984.
- [38] W. C. Dautremont-Smith, "Transition metal oxide electrochromic materials and displays: a review: Part 2: oxides with anodic coloration," *Displays*, vol. 3, pp. 67-80, 1982.
- [39] K. S. Kang and J. L. Shay, "Blue Sputtered Iridium Oxide Films (Blue SIROF's)," *J. Electrochem. Soc.*, vol. 130, pp. 766-769, 1983.
- [40] L. M. Schiavone, W. C. Dautremont-Smith, G. Beni, and J. L. Shay, "Electrochromic iridium oxide films prepared by reactive sputtering," *Appl. Phys. Lett.*, vol. 35, pp. 823-825, 1979.
- [41] S. Negi, R. Bhandari, L. Rieth, and F. Solzbacher, "Effect of sputtering pressure on pulsed-DC sputtered iridium oxide films," *Sensors and Actuators B: Chemical*, vol. 137, pp. 370-378, 2009.
- [42] W. F. Agnew, T. G. H. Yuen, D. B. McCreery, and L. A. Bullara, "Histopathologic evaluation of prolonged intracortical electrical stimulation," *Experimental Neurology*, vol. 92, pp. 162-185, 1986.
- [43] E. M. Kelliher and T. L. Rose, "Evaluation of Charge Injection Properties of Thin Film Redox Materials for use as Neural Stimulation Electrodes," *MRS Online Proceedings Library*, vol. 110, 1987.

CHAPTER 3

EXCIMER-LASER DEINSULATION OF PARYLENE-C COATED UTAH ELECTRODE ARRAY TIPS

Reprinted with permission from Sensors and Actuators B: Chemical

Volume 166-167, pp. 777-786, 2012



Excimer-laser deinsulation of Parylene-C coated Utah electrode array tips

Je-Min Yoo^{a,b,*}, Asha Sharma^b, Prashant Tathireddy^b, Loren W. Rieth^b, Florian Solzbacher^b, Jong-In Song^{a,**,}

^a Department of Nanobio Materials and Electronics, Gwangju Institute of Science and Technology, Gwangju 500-712, Republic of Korea

^b Department of Electrical and Computer Engineering, University of Utah, Salt Lake City, UT, United States

ARTICLE INFO

Article history:

Received 2 June 2011

Received in revised form 19 March 2012

Accepted 27 March 2012

Available online 2 April 2012

Keywords:

UEA

Parylene

Laser deinsulation

Photoablation

Excimer laser

ABSTRACT

Utah electrode arrays (UEAs) are highly effective to measure or stimulate neural action potentials from the central or peripheral nervous system. The measured signals can be used for applications including control of prosthetics (recording) and stimulation of proprioceptive percepts. The UEAs are coated with biocompatible Parylene-C, and the electrode tips are deinsulated to expose the active electrode coated with sputtered iridium oxide films (SIROFs) to transduce neural signals. In conventional UEA technology, the electrode tips are deinsulated by poking the electrodes through aluminum foil followed by an oxygen plasma etch of the exposed areas. However, this method suffers from lack of uniformity and repeatability and it is time consuming. We focus on laser tip-deinsulation technology that can provide a repeatable, uniform, and less time consuming tip exposure for UEAs. The laser deinsulated SIROF area is characterized by X-ray photoelectron spectroscopy (XPS), scanning electron microscope (SEM), a tomographic microscope (AFM), and by measuring the impedance of the exposed sites. The value of impedance and XPS peaks showed that the Parylene was clearly removed. The damage induced by laser irradiation on the SIROF film was also investigated to understand the selectivity of laser deinsulation. Thicker SIROF films showed better resistance to fracture. The results indicate that laser deinsulation is an effective method to etch Parylene films.

© 2012 Elsevier B.V. All rights reserved.

1. Introduction

Neural interfaces for chronic implantation need to be encapsulated by a biocompatible material to protect the device from the harsh physiological environment. In addition, the encapsulation material must be biocompatible in contact with the neural tissue in the vicinity of the device. Parylene-C, which has a polymer structure as presented in Fig. 1, is a representative material for encapsulation in biomedical implants and has good adhesion, uniformity, electrical insulation, and biological and chemical inertness, is non-toxic to body tissue [1–3].

Neural recording and stimulation require the removal of the Parylene from the active electrode tips of the UEA to facilitate transduction [4]. In very early designs, the recording tips of the microelectrodes were exposed either by using a heating element to melt back the insulation or by a high-voltage arcing technique [2]. The heating method usually led to the breakdown of the insulation

near the tip after implantation. The high voltage arcing technique resulted in poor adhesion of the Parylene insulation at the tips and caused tiny fractures along the electrode shaft, which decreased the impedance values. In addition, these methods made it difficult to control the size of the tip exposure. Several other methods, such as chemical etching, cannot be used because Parylene is inert to most solvents. Therefore, dry etching processes are currently considered the most suitable method, and these include plasma etching, ion reactive etching, and deep reactive etching [5].

Oxygen plasma etching is the standard method to remove Parylene from the electrode tip in UEA manufacturing [6]. Both the photoresist and the aluminum foil mask with oxygen plasma etching have been investigated in UEA technology [7–9]. However, the photoresist etching mask changes the surface properties of the Parylene. Therefore, poking the electrode tips through an aluminum foil to the desired exposure length for deinsulation of the Parylene has been adopted as a regular masking procedure in UEA technology. However, the polishing of an aluminum mask is a time consuming process that is not practical on a production scale, and it also has an inherent problem of non-uniformity and poor repeatability leading to a large variation in the impedance values. Moreover, the foil mask cannot be used for more complex geometries, such as variable height electrodes.

* Corresponding author at: Department of Electrical and Computer Engineering, University of Utah, 505 Central Campus Drive, MEB 1690, Salt Lake City, UT 84112, United States. Tel.: +1 801 581 6941; fax: +1 801 581 5281.

** Corresponding author. Tel.: +82 62 715 2208.

E-mail addresses: Je-Min.Yoo@utah.edu (J.-M. Yoo), jsong@gist.ac.kr (J.-I. Song).

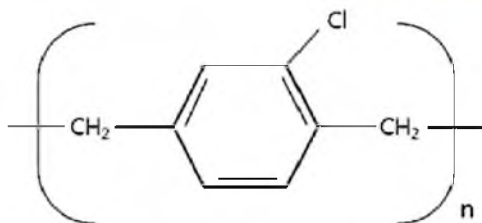


Fig. 1. The structure of Parylene-C.

To overcome the shortcomings of an aluminum foil mask, deinsulation using a laser is investigated as an appropriate alternative. Laser ablation of Parylene has been used since the early 1990s [10]. Laser deinsulation has also been demonstrated to remove Parylene from biomedical microelectrodes based on Pt tips [11,12], and to ablate micron-thick Parylene films from a copper surfaces [13].

There are two primary mechanisms for laser etching, vaporization and photoablation, which result in removal of surface layers [14]. To use the laser photoablation method for Parylene deinsulation from UEA tips, several processing parameters, for example, laser wavelength, pulse duration, the number of pulses, and fluence, need to be optimized. In this study, we used the laser ablation method for deinsulating the Parylene-coated iridium oxide tips of the UEA.

The trade-off between the fluence and the number of pulses was an important consideration for selective photoablative removal of Parylene without leaving any cracks or damage in the iridium oxide active electrode surfaces. Using a KrF (248 nm) excimer laser appears to be a useful ablation method due to a strong absorption characteristic of the Parylene as well as the iridium oxide film in the UV region below the wavelength of 280 nm.

We first investigated the laser ablation of the Parylene-coated iridium oxide film deposited on flat silicon substrates to study the influence of the laser and characterize the laser ablated iridium oxide surfaces by scanning electron microscopy (SEM), atomic force microscope (AFM), and X-ray photoelectron spectroscopy (XPS). Based on the optimization of the laser parameters on planar surfaces, we implemented the laser ablation method to deinsulate the Parylene from the tips of 3-D Utah electrode array.

2. Experiment

2.1. Fabrication of planar structures and microelectrode arrays

The flat substrates prepared for initial optimization of the laser deinsulation parameters consisted of film stacking similar to the Utah electrode array. The samples were prepared using *p*-type (100) single crystal silicon wafers. Titanium (50 nm), followed by iridium oxide (400, 800 and 1100 nm) were deposited on the silicon

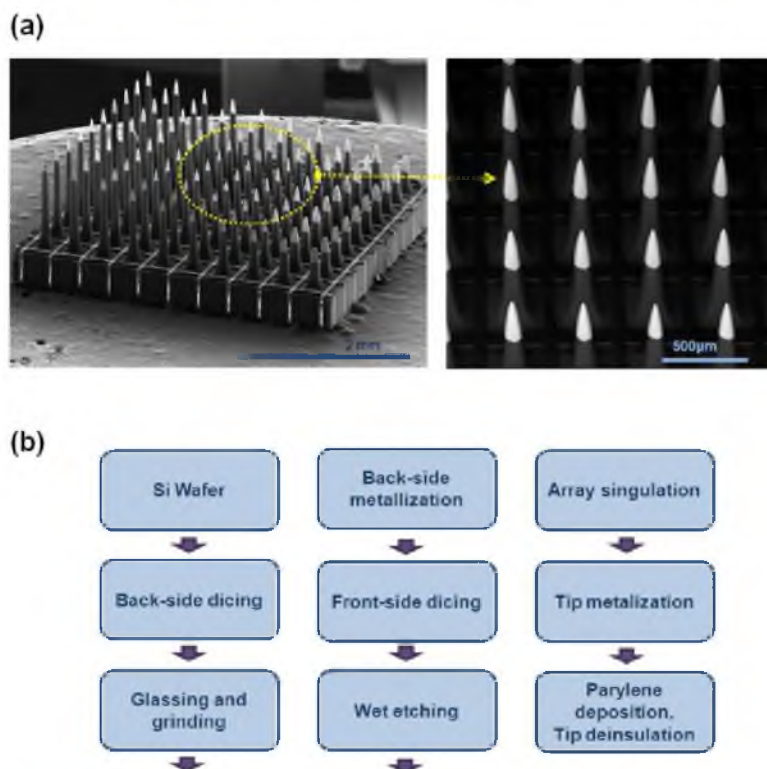


Fig. 2. (a) Scanning electron micrograph of UEAs (left) and the backscattered image of the electrode array in detail (right) and (b) schematic view of the process flow for wafers-scale fabrication of the Utah electrode array.

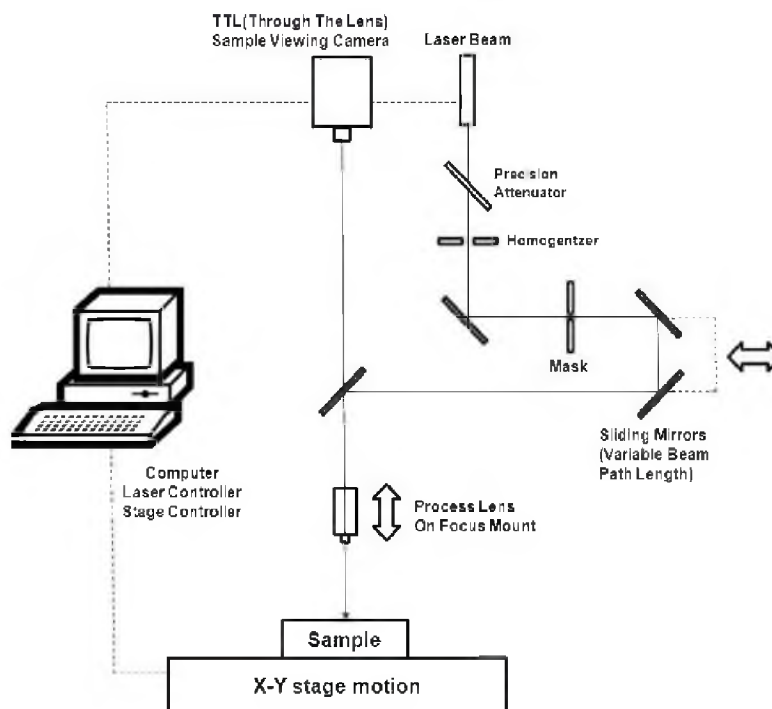


Fig. 3. Schematics diagram of the laser ablation system.

substrates by DC and Pulsed-DC sputter deposition, respectively (TMV Super Series SS-40C-IV Multi Cathode Sputtering system). The titanium acts as an adhesive layer and was deposited in Ar ambient with flowing of 150 sccm at a chamber pressure of 20 mTorr and sputtering power of 90 W for 5 min. The titanium target was 99.6% pure, 3 in. in diameter and 0.125 in. in thickness (Kurtj Lesker, Pittsburgh, PA). SIROF was deposited in Ar and O₂ plasma with both gases flowing at the rate of 100 sccm. The sputtering power was 100 W with deposition pressure of 10 mTorr. The deposition rate was 10 nm/min. The pulse width and frequency were 2016 ns and 100 kHz, respectively. The iridium target was 99.8% pure, 3 in. in diameter and 0.125 in. in thickness (Kurtj Lesker, Pittsburgh, PA). Three different thicknesses of iridium oxide films were deposited on flat substrates in order to investigate film damage from the laser. Annealing (Lindberg Annealing Furnace, 375 °C using 98% Ar and 2% H₂ forming gas) was performed to improve the adhesion between the deposited films and the substrate, and aid in the formation of Ohmic contacts. Parylene (3 μm) film was deposited by chemical vapor deposition using a Paratech 3000 Labtop deposition system. To improve the chemical adhesion between the Parylene and the underneath film, 0.5% Silquest A-174 silane was used. Finally, the Parylene film was removed from the active area by the laser system (Optec MicroMaster Excimer Laser, KrF 248 nm).

The UEA is a 3-D silicon-based structure consisting of a 10 × 10 array of tapered silicon electrodes with a length of 1.5 mm and pitch of 400 μm between tips as shown in Fig. 2(a). The detailed SEM image on the right presents several electrodes just after tip metallization which shows the connections to iridium oxide film

that form the active surface. Fig. 2(b) is the schematic view of the process flow for wafers-scale fabrication of UEAs. To make the UEAs, a 2 mm thick, p-type, c-Si (100) wafer with the diameter of 75 mm and a resistivity of 0.01–0.05 Ω cm was prepared as substrates. Back-side dicing, glassing and grinding were needed to form the back side metal pad for wire bonding. Front-side dicing and wet etching were then used to shape the electrodes. Then, array singulation, tip metallization and Parylene deposition were performed to complete the devices. During the tip metallization, titanium and iridium oxide were deposited by DC and Pulsed-DC sputter deposition, respectively, and annealed in a way similar to that described for the planar substrates. For the last step, tip deinsulation was carried out. The fabrication of UEAs is described elsewhere in detail [7,15].

2.2. Excimer laser system and optical layout description

The laser deinsulation system used in this study includes an excimer laser, sophisticated beam delivery optics, a precision sample motion stage, and a computer with a flexible control software as shown in Fig. 3. The wavelength of the laser is 248 nm (KrF) which is capable of photoablating the Parylene films. The laser operates in a pulse mode, typically pulsing at a rate of 100 Hz. Pulses are 5–6 ns in duration. The fluence can be controlled by laser energy.

This system uses projection optics where the laser beam is passed through a circular mask, and then was demagnified and focused on the sample. A circular mask was used because the electrode base is circular. The sample for laser deinsulation was mounted on a vacuum chuck. The sample motion stage had a

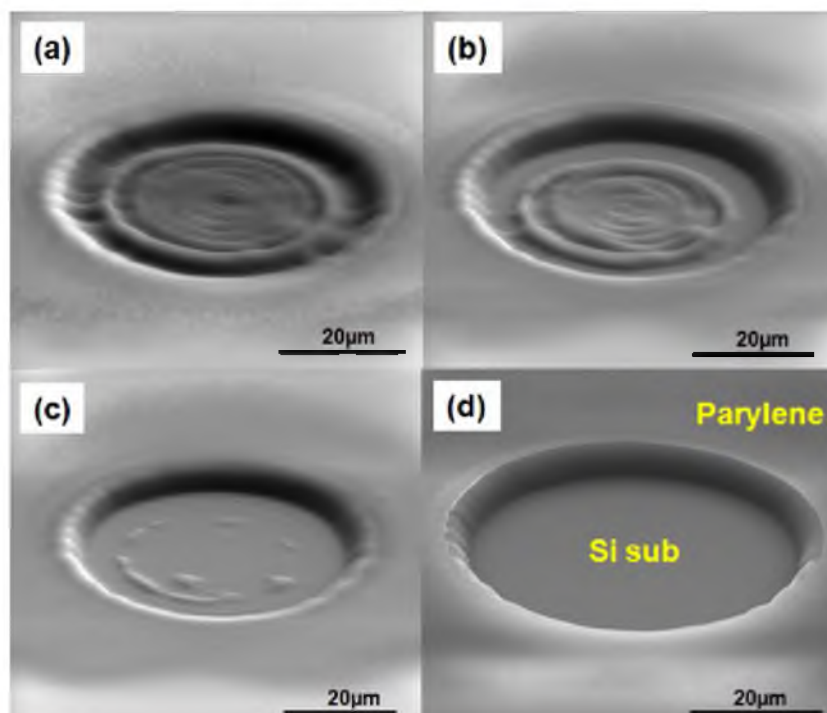


Fig. 4. 30° filtered scanning electron micrographs (SEM) of the circles on a silicon substrate after laser ablation with 1000 mJ/cm^2 : (a) 10 pulses, (b) 20 pulses, (c) 30 pulses and (d) 100 pulses.

resolution of $1 \mu\text{m}$ in x and y directions. The deinsulated area of the tip depends not only on the mask size but also on the laser fluence and the number of laser pulses. After optimization of all these factors for the desired tip exposures on the UEAs, a circular mask with the diameter of $550 \mu\text{m}$ and a process lens with a demagnification of 7.3 and a working distance of $\sim 10 \text{ cm}$ between sample and process lens were used in our experiments.

Additionally, monitoring the sample is also important for deinsulation of electrode tips precisely in μm scale. Therefore, a

real-time observation by visible imaging was used to control the deinsulation process. The laser ablation system used in this study had dual-camera vision including an off-axis camera for general overview and a high magnification through the lens (TTL) image in windows on a flat screen monitor. When the sample was in focus on the CCTV, the UV was automatically in focus on the sample. The laser system has independent light sources, including a highlighter for optimum contrast on the sample. This was helpful in finding the tip location.

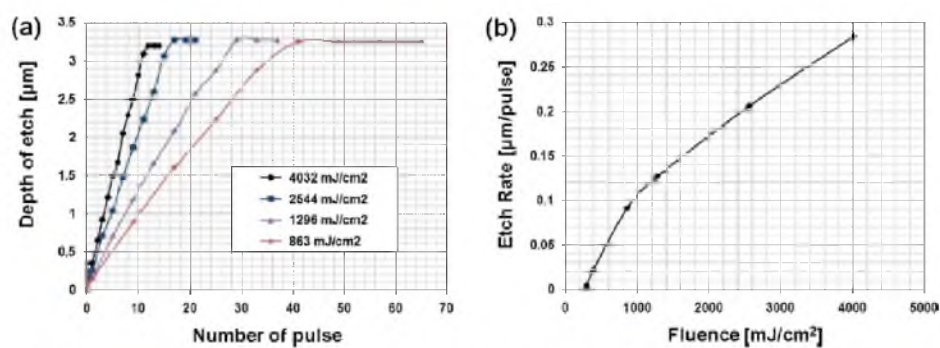


Fig. 5. (a) The etch depth of the Parylene as a function of the number of laser pulses and (b) the Parylene etch rate by as a function of the fluence.

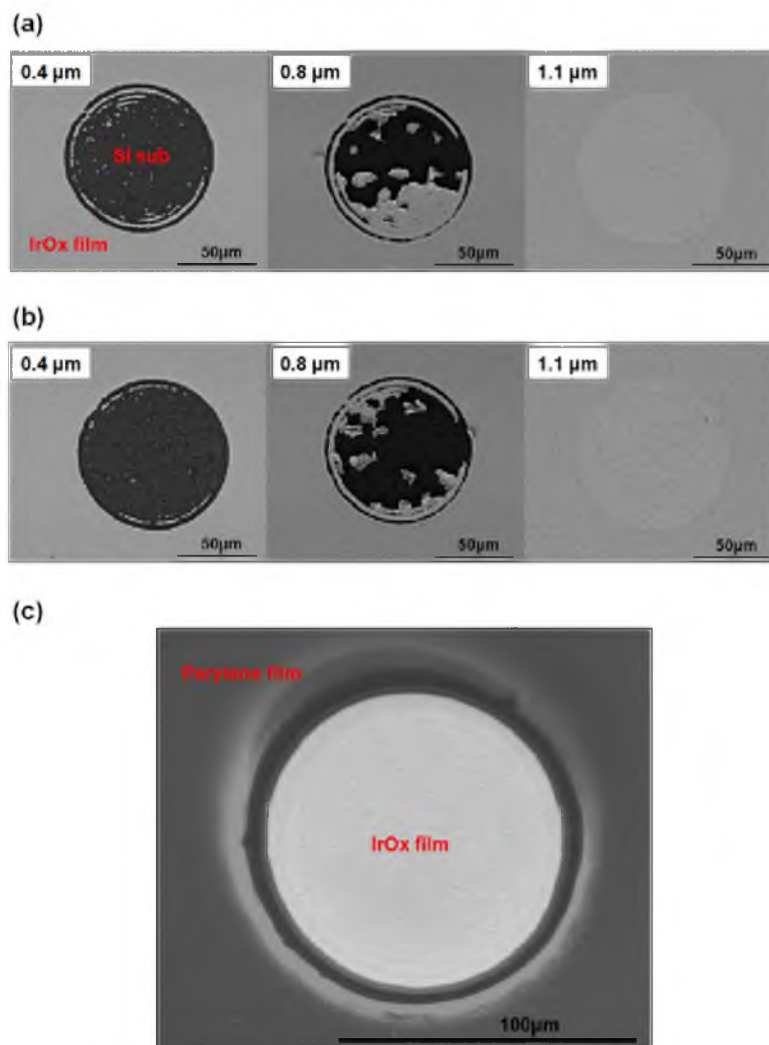


Fig. 6. (a) SEM images (backscattering images) for films with three different thicknesses (0.4 μm , 0.8 μm , and 1.1 μm) exposed to a single laser pulse with 1680 mJ/cm^2 fluence for investigation of iridium oxide film fracture tendency, (b) SEM images for films with three different thicknesses (0.4 μm , 0.8 μm , and 1.1 μm) exposed to 100 laser pulses with 1680 mJ/cm^2 fluence and (c) SEM image of the laser ablated hole on a Parylene-coated iridium oxide film.

2.3. Surface, chemical, and electrical characterization of laser deinsulated electrodes

The surface morphology and roughness before and after laser deinsulation were examined by scanning electron microscopy (SEM) using an FEI Quanta SEM and a Digital Instruments atomic force microscope (AFM). Chemical analysis of the deinsulated spots was performed by X-ray photoelectron spectroscopy (XPS) using a Kratos Axis Ultra DLD to examine the presence of iridium, oxygen,

carbon and chlorine, and to look for any changes in film composition due to laser irradiation. Utah electrode impedances were measured by poking the electrodes into conductive agar using an impedance meter (Blackrock Microsystems). The agar was prepared from phosphate-buffered saline and agarose powder in a weight ratio of 42:1. A platinum counter electrode probe was inserted in the agar. Impedances of individual electrodes were measured sequentially using a probe signal of 100 nA (peak to peak) at a 1 kHz frequency.

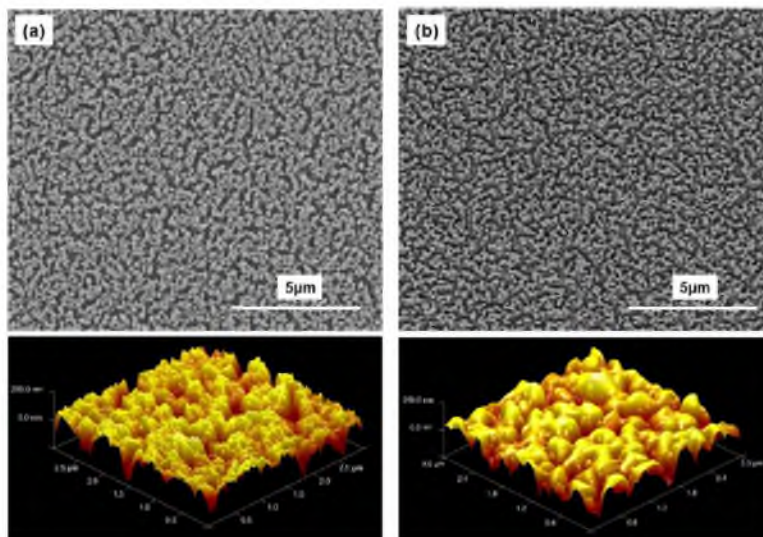


Fig. 7. SEM images (upper) and AFM images (bottom) of iridium oxide films before (left) and after (right) laser ablation.

3. Results and discussion

First, the effect of laser exposure after removal of the Parylene was investigated by changing the number of laser pulses. Fig. 4 shows a set of four SEM micrographs from a laser ablated hole in the Parylene film on the silicon substrate after laser ablation using a fluence of 1000 mJ/cm^2 . When the number of pulses used for ablation was 10, the Parylene remained as a ripple-shaped circle as seen in Fig. 4(a). Figs. 4(b)–(d) have successively less Parylene remaining as the number of pulses was increased to 20, 30, and 100, respectively. Fig. 4(d) shows that a clean deinsulated surface without any Parylene residue was obtained when 100 pulses were used.

We then investigated the effect of beam fluence on the Parylene etch rate for the planar samples. Fig. 5(a) presents the etch depth of the Parylene film as a function of the number of pulses for $3.2 \mu\text{m}$ Parylene film. The last point of each curve indicates the number of pulses required to remove Parylene completely without any residue on the hole area. As expected, the number of pulses required for complete removal of Parylene decreased as a higher fluence was used. Fig. 5(b) shows the etch rate of Parylene as a function of the fluence, which indicates that at least approximately 250 mJ/cm^2 is required to etch Parylene.

The effect of SiROF thickness on the damage to the film from laser ablation was investigated. The incident laser energy absorbed in the surface material is converted into electronic or vibrational excitation energy, which causes laser desorption or ablation. The skin depth for excitation is typically on the order of tens of nanometers. Within a skin depth of about 50–100 nm of the surface, there is an extremely high density of excitation [14]. We compared several iridium oxide film samples with different thicknesses to investigate the film damage that is caused by laser energy. Fig. 6(a) shows the SEM images of iridium oxide films with three different thicknesses ($0.4 \mu\text{m}$, $0.8 \mu\text{m}$, and $1.1 \mu\text{m}$) after being exposed to a single laser pulse with 1680 mJ/cm^2 fluence. As can be seen in the figure, a thicker film had a higher resistance to damage. The threshold fluences for film damage were 1200, 1440, and 1920 mJ/cm^2 for the film thickness of $0.4 \mu\text{m}$, $0.8 \mu\text{m}$, and $1.1 \mu\text{m}$, respectively.

Additionally, the fluence and the number of pulses were also examined, and expected the iridium oxide film suffered from more fracture as higher laser fluence was used. However, the number of pulses did not show significant difference in film damage for up to 100 laser pulses as shown in Fig. 6(b). Based on these results, we chose the iridium oxide film thickness of $1.1 \mu\text{m}$ since it had a larger safety margin for clean removal of the Parylene without damaging the underlying iridium oxide film. Fig. 6(c) shows the SEM image of a laser deinsulated hole on a $1.1 \mu\text{m}$ thick iridium oxide film coated with $3 \mu\text{m}$ thickness of Parylene. The fluence and the number of pulses were 1000 mJ/cm^2 and 100, respectively. The image shows the deinsulated iridium oxide film without any damage.

The surface of an iridium oxide film was inspected using SEM and the data are presented in Fig. 7, with micrographs from (a) before and (b) after laser illumination. The surface became more granular after laser irradiation. Atomic force microscopy was also performed to examine the surface roughness of the iridium oxide film before and after the laser ablation. The left bottom image of Fig. 7 is the AFM image of an as-deposited iridium oxide film with the scan area of $3 \mu\text{m} \times 3 \mu\text{m}$ and the R_{rms} of the film was 64 nm. The right bottom image of Fig. 7 shows the AFM images of an iridium oxide film with the same scan area after laser ablation and the R_{rms} of the film was 67 nm. However, when the scan area was reduced to $0.5 \mu\text{m} \times 0.5 \mu\text{m}$, the R_{rms} changed from 21.6 nm before laser ablation to 18 nm after laser ablation. This confirms that the surface of the iridium oxide film became smoother through heat treatment by laser energy.

To investigate change of the elemental/chemical composition of the iridium oxide surface during ablation, the XPS spectra using an Al K α anode operated at 300 W and 15 kV were collected from the film from the $200 \mu\text{m}$ diameter ablated hole shown in Fig. 6. The XPS spectra from a bare Parylene film deposited on top of an iridium oxide film substrate show Cl 1s and Cl 2p peaks as shown in the left of Fig. 8(a). The analysis area was approximately $700 \mu\text{m} \times 300 \mu\text{m}$. The XPS spectra from an ablated surface show Ir 4f and O 1s and C 1s peaks. The Ir 4d peak is very close to C 1s as can be observed in the right of Fig. 8(a). The XPS beam spot size was chosen as

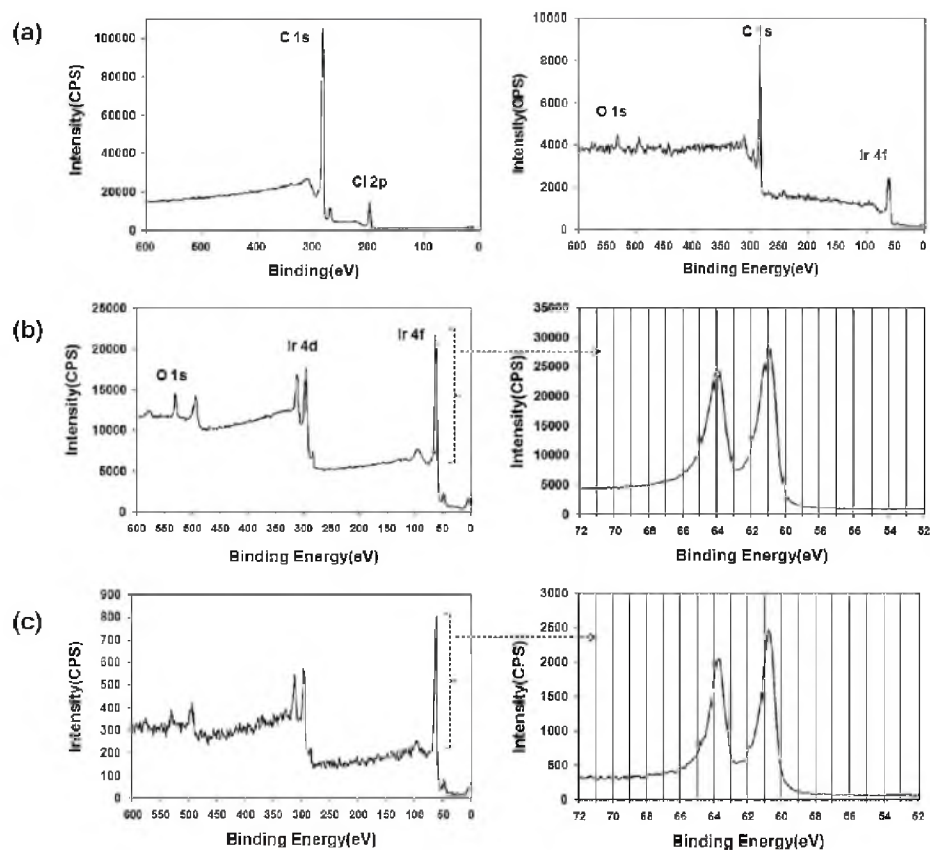


Fig. 8. X-ray photoemission spectra of (a) the Parylene film (left) and laser ablated spot on Parylene coated iridium oxide film (right), (b) as deposited iridium oxide film (left) and Ir 4f peaks in high resolution scan (right) and (c) laser ablated spot on as deposited iridium oxide film (left) and Ir 4f peaks in high resolution scan (right).

110 $\mu\text{m} \times 110 \mu\text{m}$ to analyze the ablated area of hole. The C 1s peak in the figure could be due to the debris of carbon coming onto the surface after the Parylene decomposition by the laser energy. During ablation, the molecular fragments ejected from the ablation zone could have the momentum exchange with the surrounding atmosphere and could have been redeposited on the ablated area. The redeposition occurs generally in vicinity of the ablation area. Although there are carbon deposits in the ablated area indicated by the C 1s peak, the absence of the chlorine peak indicates that the Parylene has been removed.

Fig. 8(b) and (c) presents XPS spectra of an as-deposited iridium oxide and a laser irradiated spot on the iridium oxide film. Both spectra show the Ir 4f and O 1s peaks. These peaks are similar to those observed in the right of Fig. 8(a) except for the carbon peak. The images on the right of Fig. 8(b) and (c) show the detailed Ir 4f peaks with high resolution which has very metallic characteristics. For the as-deposited iridium oxide shown in Fig. 8 (b) the peak position is 61 eV for Ir 4f_{7/2} and 64 eV for Ir 4f_{5/2}. However, after laser ablation the position of the peaks shifted to the lower binding energy as shown in Fig. 8(c). This is attributed to the removal of the natural oxygen from the surface by laser energy. The XPS analysis shows that the laser ablation carried out in this

experiment did not change elemental/chemical composition of the iridium oxide.

Finally, the laser tip deinsulation was performed on the 3-D Utah electrode array. The thickness of the iridium oxide film was 1.1 μm , which was determined from prior experimental data on the planar structure as described previously. The electrode tip exposure should be targeted at more than 20 μm from the tip of the electrode to the encapsulation edge in the Utah electrode to acquire good neuron sensitivity and impedance value enough for neural recording applications in cortical tissue [6]. Fig. 9 shows 30° tilted scanning electron micrograph images of a Utah electrode tip with 1.1 μm thick iridium oxide film after laser illumination. Fig. 9(a) shows the images of laser deinsulated tips after they were exposed to 35, 100, and 200 laser pulses with a fluence of 1440 mJ/cm^2 . The exposures of the electrode tip to the encapsulation edge are ~ 5 , 30, and 90 μm for 35, 100, and 200 laser pulses, respectively. Fig. 9(b) shows the images of laser deinsulated tips after they were exposed to the fluence of 1200, 1440, and 1680 mJ/cm^2 with 150 laser pulses. The exposures of the electrode tip to the encapsulation edge are ~ 45 , 60 and 80 μm for the fluence of 1200, 1440, and 1680 mJ/cm^2 , respectively. These results indicate that the exposure of the electrode tip can be controlled by fluence and number of

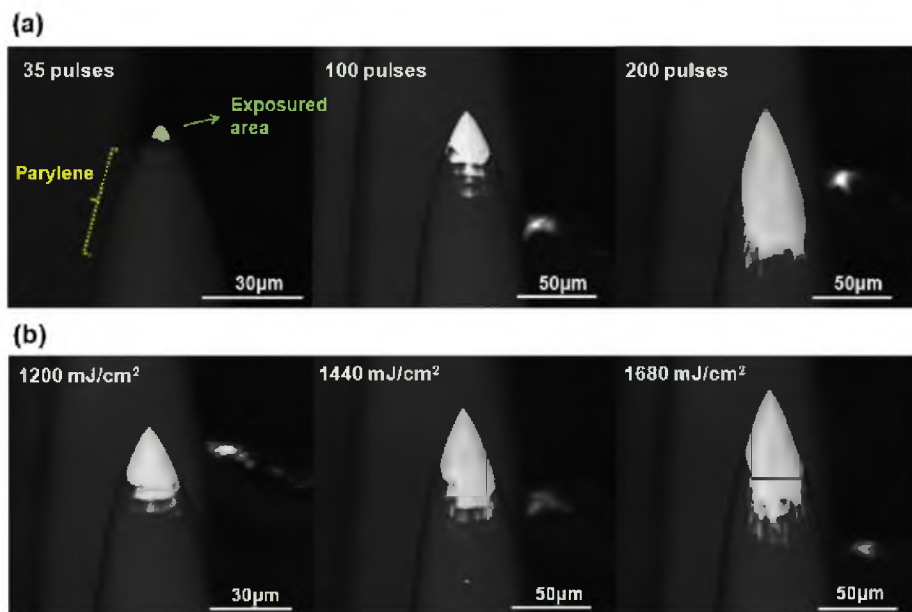


Fig. 9. 30° tilted scanning electron micrograph using backscattered electron images of a Utah electrode tip having 1.1 μm thickness iridium oxide film after laser deinsulation by (a) 35, 100, and 200 pulses with the fluence of 1440 mJ/cm^2 and (b) fluence of 1200, 1440, and 1680 mJ/cm^2 with 150 laser pulses.

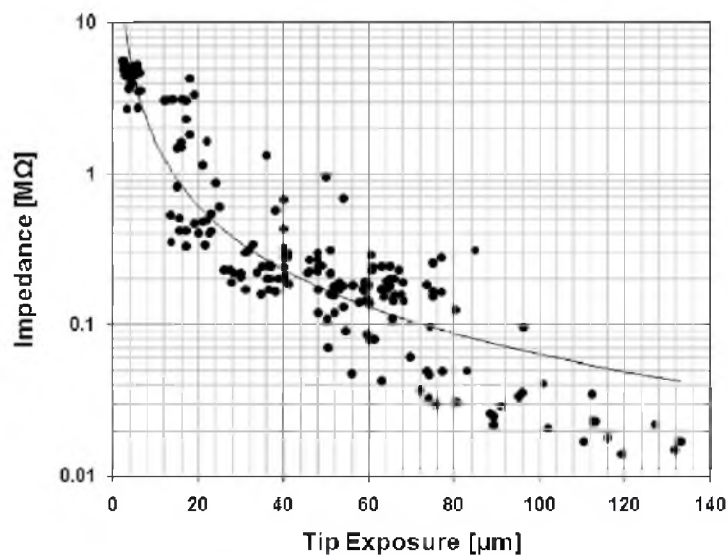


Fig. 10. Impedance values as a function of the tip exposure of laser deinsulated Utah electrode. The tip exposure lengths were measured by SEM at a 30° sample tilt angle. The solid line is the trend line with the equation $y = 41.309x^{-1.405}$.

laser pulses. The uneven removal of Parylene from the electrode tips is attributed to the nonuniformity of laser power and the varying oblique angles between the laser beam and the electrode tip surface. However, the tip exposure was highly reproducible, leading to the same area of exposure under the same deinsulation conditions.

Fig. 10 shows the impedance values as a function of the tip exposure of laser deinsulated Utah electrode arrays. The y-axis is a log scale to express the impedance value in the entire tip exposure range from $\sim 2 \mu\text{m}$ to $\sim 130 \mu\text{m}$. The tip exposure lengths were measured by SEM at a 30° sample tilt angle. The solid line is the trend line with the equation $y = 41.309x^{-1.405}$. The impedance value became around $0.02 \text{ M}\Omega$ as the tip exposure is increased beyond $140 \mu\text{m}$ and become larger than $1 \text{ M}\Omega$ for tip exposures of less than $20 \mu\text{m}$. The rather high deviation of impedance values from the trend line is attributed to the variation of the contact force of the working probe during impedance measurement and the variation of the amount of carbon redeposition on the active tip surface during the laser ablation process. The electrode tip exposure larger than $100 \mu\text{m}$ provides the impedance value of a few tens of kilo-ohm, which is the normal target impedance value for neural interface applications [6].

4. Conclusions

This study demonstrated that the laser ablation using a KrF excimer laser is an effective deinsulation method for Parylene-coated Utah electrode array. Optimum conditions for deinsulating the electrode tips in the UEA using the laser ablation were investigated through XPS, SEM, and AFM analyses and impedance measurement. The thickness of the iridium oxide film that is resistant to the film fracture induced by laser energy was derived and the parameters of laser ablation in terms of the fluence and the number of laser pulses for complete removal of Parylene film from the electrode tip were also derived. The laser ablation process was used for deinsulation of Parylene-coated Utah electrode array, producing the electrode impedance in the range of tens of $\text{k}\Omega$ that is suitable for implantable neural interface device applications. A more sophisticated method to remove the residual carbon redeposited on the deinsulated electrode surface will be explored to reduce the rather large variation of the electrode impedance value. The results suggest that the laser ablation using a KrF excimer laser is acceptable for deinsulation of the Utah electrode tips and more complicated electrode structures for implantable device applications.

Acknowledgments

This work was supported by WCU (R31-2008-000-10026-0) and Bio-imaging Research Center programs at GIST, and DARPA award N66001-06-C-4056. Sample fabrication, laser deinsulation, and film characterization were performed in the Utah Nanofabrication Lab and the Surface and Nanomaging Lab at University of Utah. I would like to thank Brian van Devener, Kathryn Ecsedy, and others for assistance in collecting XPS and SEM data and the UEA production team for providing the electrode arrays. Florian Solzbacher has commercial and financial interest in Blackrock Microsystems.

References

- [1] C. Hassler, R.P. von Metzner, P. Rucher, T. Spiegeltz, Characterization of parylene C as an encapsulation material for implanted neural prostheses, *Journal of Biomedical Materials Research Part B: Applied Biomaterials* 93B (2010) 266–274.
- [2] G.E. Loeb, M.J. Bak, M. Salzman, E.M. Schmidt, Parylene as a chronically stable, reproducible microelectrode insulator, *biomedical engineering*, *IEEE Transactions on BME* 24 (1977) 121–128.
- [3] D.C. Rogger, A.J. Fong, W. Li, H. Ameri, A.K. Abuja, C. Gutierrez, I. Lavrov, H. Zhong, P.R. Menon, E. Meng, J.W. Burdick, R.R. Roy, V.R. Edgerton, J.D. Weiland, M.S. Humayun, Y.-C. Tai, Flexible parylene-based multielectrode array technology for high-density neural stimulation and recording, *Sensors and Actuators B: Chemical* 132 (2008) 449–460.
- [4] R.A. Normann, Technology insight: future neuroprosthetic therapies for disorders of the nervous system, *Nature Clinical Practice, Neurology* 3 (2007) 444–452.
- [5] E. Meng, et al., Plasma removal of Parylene C, *Journal of Micromechanics and Microengineering* 18 (2008) 045004.
- [6] H. Jui-Mei, L. Rieth, R.A. Normann, F. Tathireddy, F. Solzbacher, Encapsulation of an integrated neural interface device with parylene C, *IEEE Transactions on Biomedical Engineering* 56 (2009) 23–29.
- [7] P.K. Campbell, K.E. Jones, R.J. Huber, K.W. Horch, R.A. Normann, A silicon-based, three-dimensional neural interface: manufacturing processes for an intracortical electrode array, *IEEE Transactions on Biomedical Engineering* 38 (1991) 758–768.
- [8] J.-J. et al., Microfabricated microneedle with porous tip for drug delivery, *Journal of Micromechanics and Microengineering* 16 (2006) 958.
- [9] R. Bhandari, S. Negi, L. Rieth, R.A. Normann, F. Solzbacher, A novel masking method for high aspect ratio penetrating microelectrode arrays, *Journal of Micromechanics and Microengineering* 19 (2009) 035004.
- [10] M. Esashi, M. Minami, S. Shoji, Optical exposure systems for three-dimensional fabrication of microprobe, in: *Micro Electro Mechanical Systems MEMS '91*, Proceedings, An Investigation of Micro Structures, Sensors, Actuators, Machines and Robots, IEEE, 1991, pp. 39–44.
- [11] G.E. Loeb, R.A. Peck, J. Martyniuk, Toward the ultimate metal microelectrode, *Journal of Neuroscience Methods* 63 (1995) 175–183.
- [12] E.M. Schmidt, M.J. Bak, P. Christensen, Laser exposure of Parylene-C insulated microelectrodes, *Journal of Neuroscience Methods* 62 (1995) 89–92.
- [13] C. Voonsu, O.C. Seong, R.H. Shafer, M.G. Allen, Highly inclined electrodeposited metal lines using an excimer laser patterning technique, in: *Digest of Technical Papers, TRANSDUCERS '05*, The 13th International Conference on Solid-State Sensors, Actuators and Microsystems, vol. 1462, 2005, pp. 1469–1472.
- [14] J.C. Miller, R.F. Haglund, Laser Ablation and Desorption, Academic Press, 2009.
- [15] R. Bhandari, S. Negi, L. Rieth, F. Solzbacher, A wafer-scale etching technique for high aspect ratio implantable MEMS structures, *Sensors and Actuators A: Physical* 162 (2010) 130–136.

Biographies

Je-Min Yoo received his Master's degree in Physics in 2006 at Korea University. In 2007, he started his Ph.D. degree in the Department of Nanobio Materials and Electronics in Gwangju Institute Science and Technology. He has worked in the Integrated Neural Interface Program (INIP) at the University of Utah as a visiting researcher since 2009. His current research interests include the design, fabrication, testing of MEMs and wireless Brain Machine Interface (BMI) devices, power/data transfer system, and CMOS analog circuit design.

Asha Sharma received her Ph.D. from the Indian Institute of Technology Kanpur, India, in 2006. She was a Postdoctoral Fellow at the Georgia Institute of Technology in Atlanta in the School of ECE until 2008. Following that, she worked at the University of Utah in Salt Lake City from 2009 to 2011 as a Postdoctoral Researcher in the Microsystems Laboratory, focusing her research on fully integrated wireless neural interfaces. She is currently a Research Scientist-II at the Georgia Institute of Technology in Atlanta in the School of ECE. Her primary research interests are organic electronic devices, such as OPV, OLED, and OFET. In addition, she is also interested in the application of organic electronics and photonics to the biology and medicine for the next generation of biocompatible, low cost, and clean-environment healthcare technologies. She has co-authored 23 publications in peer-reviewed journals and 24 contributed conference presentations and proceedings.

Prashant Tathireddy received a Bachelor's degree in chemical technology from Osmania University, Hyderabad, India, in 1997, and the Ph.D. degree from the Department of Chemical Engineering, University of Utah, Salt Lake City, in 2004. Until 1999, he was a Project Leader at Computer Maintenance Corporation (CMC) Limited, Hyderabad. Until 2007, he was a Postdoctoral Fellow in the Microsystems Laboratory, Department of Electrical and Computer Engineering, University of Utah, where he is currently a Research Assistant Professor in the Department of Electrical and Computer Engineering. He is also a Guest Scientist at Fraunhofer Institute for Biomedical Engineering (IBMT) in St. Ingbert, Germany. His current research interests include development and fabrication of implantable microdevices (BioMEMS), microfluidics, and microsensors.

Loren Rieth received his BS degree in materials science from The Johns-Hopkins University, Baltimore, MD, in 1994. He received his PhD in materials science and engineering from the University of Florida, Gainesville, FL, in 2001. From 2001 to 2003, he was a postdoctoral research associate at the University of Utah, Salt Lake City, UT, and continued at the University of Utah as a research assistant professor in materials science (2003–2005), and electrical and computer engineering (2004–present). His research is focused on deposition and characterization of thin film materials for sensors (chemical, physical, and biological), MEMS, BioMEMS, and energy production.

Florian Solzbacher received his MSc. in electrical engineering from the Technical University Berlin in 1997 and his Ph.D. from the Technical University Ilmenau in 2003. He is director of the Microsystems Laboratory at the University of Utah and a faculty member in the departments of Electrical and Computer Engineering,

Materials Science and Bioengineering, and he is responsible for the Utah branch office of the Fraunhofer IZM, Germany. Dr. Solzbacher is co-founder of First Sensor Technology GmbH, an established supplier to the automotive and process control industry in the USA, Europe and Asia. He is Chairman of the German Association for Sensor Technology AMA. His work focuses on harsh environment microsystems, sensors and materials. He is author of over 60 scientific and engineering publications and book chapters on MEMS devices, technologies and markets for harsh environments. Since 2004, he has been Chairman of Sensor + Test, the world's largest international trade fair and ensemble of conferences for sensors, metrology and testing.

Jong-In Song received the BS degree in electronics engineering from Seoul National University, Seoul, Korea, in 1980, the MS degree in electronics engineering from the Korea Advanced Institute of Science and Technology (KAIST), Daejeon, Korea, in

1982, and the Ph.D. degree in electrical and electronics engineering from Columbia University, New York, NY, in 1990. From 1986 to 1990, he was a Graduate Research Assistant with the Center for Telecommunications Research, where he pioneered high-performance GaAs/AlGaAs 2-D electron gas (ZDEG) charge coupled device research for microwave and infrared-imaging applications. From 1990 to 1994, he joined the Electronics Science and Technology Division, Belkore, where he was primarily involved in the development of microwave transistors including GaInF/GaAs, InAlAs/InGaAs, InP/InGaAs HBTs, and their application to monolithic microwave integrated circuits (MMICs). In 1994, he joined the Gwangju Institute of Science and Technology (GIST), Gwangju, Korea, where he is currently a Professor with the Department of Nanobio Materials and Electronics. His current research interests include low-power and high-speed devices and circuits, millimeter-wave over fiber (MMoF) communication systems, and distributed sensor networks.

CHAPTER 4

HYBRID LASER AND REACTIVE ION ETCHING OF PARYLENE-C FOR DEINSULATION OF A UTAH ELECTRODE ARRAY

Reprinted with permission from Journal of Micromechanics and Microengineering

Volume 22, pp. 105036, 2012

Hybrid laser and reactive ion etching of Parylene-C for deinsulation of a Utah electrode array

Je-Min Yoo^{1,2}, Jong-In Song¹, Prashant Tathireddy², Florian Solzbacher² and Loren W Rieth²

¹ Department Nanobio Materials and Electronics, Gwangju Institute of Science and Technology, Gwangju 500-712, Korea

² Department of Electrical and Computer Engineering, University of Utah, Salt Lake City, UT-84112-9206, USA

E-mail: Je-Min.Yoo@utah.edu, jisong@gist.ac.kr and loren.rieth@utah.edu

Received 4 May 2012, in final form 15 July 2012

Published 10 September 2012

Online at stacks.iop.org/JMM/22/105036

Abstract

Electrodes used for neural interfaces are typically encapsulated by biocompatible materials such as Parylene-C. Tips of a Utah electrode array (UEA) for recording neural action potentials are typically exposed using a reactive ion etching (RIE); however, it has limitations due to the complex 3D geometry of electrode arrays, resulting in nonuniformity of deinsulated area, difficulty in achieving very fine tip exposure, and decrease in selectivity in acquiring the neural signals. The laser ablation technique can be used to deinsulate electrode tips with exposures smaller than 20 μm . However, the electrode arrays suffer from increased impedance due to redeposition of the carbon debris produced by the ablation of the Parylene-C on the active area of the electrodes. The hybrid laser and plasma etching uses a laser (KrF) ablation followed by an oxygen reactive ion etching process to better control tip exposure, particularly for electrode arrays with more complex geometries, and a lower electrode impedance at the same time. Characterization of the deinsulated electrode surface by scanning electron microscope (SEM), x-ray photoelectron spectroscopy (XPS) and impedance of a Utah electrode array (UEA) suggests that the hybrid laser/RIE method is suitable for deinsulation of UEAs for neural interface applications.

(Some figures may appear in colour only in the online journal)

1. Introduction

In order to record neuronal action potentials and/or local field potentials within the brain, neural interface electrodes should be implanted. Silicon-based implantable electrodes including the Utah electrode array (UEA) and the Michigan probes are passivated using biocompatible materials such as Parylene-C on the inactive areas to insulate the electrode sites and to protect the brain tissue [1]. In order to record neural signals or stimulate neurons the active electrode sites should be exposed. The deinsulation of electrodes in neural interface devices has been an issue as various types of electrodes with complex geometries were developed [2, 3]. Deinsulation methods reported in the literature include electrical discharge,

wet etching, dry etching and laser ablation [3–5]. The electrical discharge method has disadvantages including poor control over the tip exposure and poor adhesion of the Parylene-C layer near the exposed tip of the electrode. Moreover, it can cause tiny fractures along the electrode shaft resulting in increased impedance value. The wet etching method is challenging for removal of the Parylene-C because this material is chemically inert and thus is only etched by a few exotic solvents. Reactive ion etching is a relatively clean and effective method to remove the Parylene-C insulation, so has been adopted for use on a Utah electrode array [6] with 10×10 electrodes shown in figure 1(a). This technique uses an aluminum foil as an etching mask. The electrodes are poked through the aluminum foil to expose the tips to a desired length [7]. Figure 1(b) shows

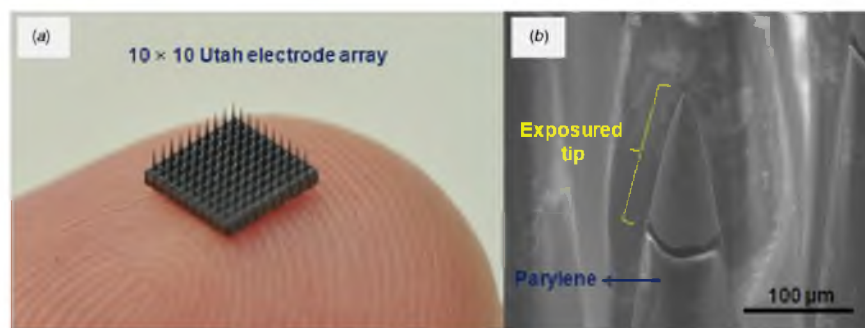


Figure 1. (a) Photograph of a Utah electrode array with 10×10 electrodes, (b) SEM image of a Utah electrode tip fabricated by the oxygen plasma etching using an aluminum foil mask.

the SEM image of a tip of a UEA exposed by the oxygen plasma etching method with an aluminum foil mask. This method is simple and can provide electrode tips with relatively low impedance. However, the impedance of electrodes within the UEA has a large standard deviation ($\sigma > 0.5 \text{ M}\Omega$) because of the nonuniformity of the tip exposure. In addition, the poking of an aluminum foil mask is done manually and thus is a time-consuming process. Moreover, the foil masks are difficult to use for complicated electrode geometries including convoluted-, cylindrical-, or spherical-shaped electrode arrays that have nonlinear gradients of electrode heights. Those complicated electrode arrays are useful for peripheral nerve interfaces, retina interfaces [2] and accessing more complex-shaped structures in the cortex.

The laser ablation method has been previously investigated [8] and applied to remove the Parylene-C from the tip of the electrodes for neural interface applications [9, 10]. Since the laser ablation can deinsulate individual electrodes, it can be effectively used for fabrication of electrode arrays with complex geometries. However, the ablation of the Parylene-C with an excimer laser has a significant drawback of redeposition of the carbonaceous debris on and around the ablation site. Laser ablation occurs through a combination of photochemical bond breaking and heating that can vaporize the material [11]. While vaporization and molten expulsion of the Parylene-C by the laser ablation can effectively remove the Parylene-C, small and volatile fragments of carbon can be accumulated in the form of debris on the surface [12]. This carbon debris can deteriorate the electrochemical impedance and the charge injection and storage capacities of the electrodes. While the debris can be removed by the laser ablation with conditions of high fluence and large number of pulses, the electrode tip exposure (the distance from the electrode tip to the Parylene-C insulation edge) becomes large ($> 50 \mu\text{m}$). For cortical neural interfaces [13, 14], a small tip exposure ($< 40 \mu\text{m}$) is typically desired to selectively record or stimulate a small population of neurons. To fabricate an electrode with a small tip exposure a laser ablation with lower fluence is required, which can produce more carbon debris and thus contribute to increased electrode impedances. The surface debris has been reported to be significantly reduced by

the laser ablation under vacuum [15], helium, or oxygen [16] environment compared with the laser ablation in air. However, the laser ablation under vacuum is somewhat impractical. The use of a shield gas with a low atomic weight is one of the most effective methods to avoid momentum exchange between the carbon debris and surrounding atmosphere, resulting in reduced deposition of the carbon debris on the sample surface. The use of helium or oxygen environment helps to dramatically reduce but does not completely eliminate the surface debris around the ablation sites.

In this paper, a hybrid method of etching Parylene-C using the laser ablation and the reactive ion etching (RIE) using an inductively coupled oxygen plasma as a post-treatment of the laser ablated active region to fabricate a carbon residue free Utah electrode array is reported.

2. Experiments

The characteristics of the laser ablation of Parylene-C on planar Si substrates as well as on electrode tips of UEAs were investigated. Planar Si substrates were used for x-ray photoelectron spectroscopy (XPS) characterization of the laser deinsulated surface since this technique cannot be applied to UEA tips. The metal and Parylene deposition processes for the planar samples is identical to those of the UEA. A 50 nm titanium film was sputter deposited followed by an iridium oxide film ($1 \mu\text{m}$) on *p*-type (100) *c*-Si wafers by DC and reactive pulsed-DC sputter deposition processes, respectively (T-M Vacuum Super series). The iridium oxide film was reactively sputtered in Ar and O_2 plasma, each flow rates of 100 sccm and using 100 W and a pressure of 10 mTorr. The deposition rate was 10 nm/min. The titanium film was used as an adhesion layer between the iridium oxide film and the Si substrate. The sputter deposited iridium oxide is an active electrode material of the electrode tips in a UEA [17]. Annealing (Lindberg annealing furnace, 375°C using 98% Ar and 2% H_2 forming gas) was performed for 45 min to improve the adhesion between the deposited films and the substrate, and aid in the formation of Ohmic contacts. A $3 \mu\text{m}$ thick thin film of Parylene-C was then deposited by a chemical vapor

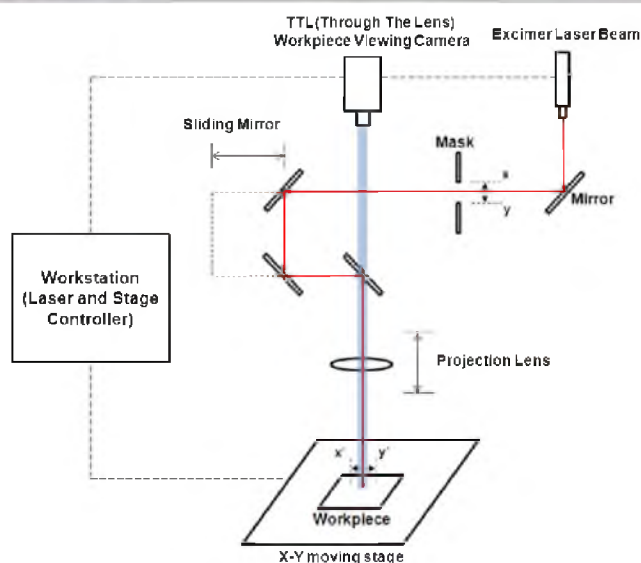


Figure 2. Schematics of the laser ablation system.

deposition system (Paratech 3000 Labtop) using the Gorham process [6, 18]. To improve adhesion between the Parylene-C and the Si substrate, an adhesion promoter, Silquest A-174 silane, was used [6]. The fabrication process of the UEA is reported elsewhere in detail [19, 20].

The Parylene-C encapsulation material on a planar sample and electrode tips of the UEA was removed by the laser ablation. The laser ablation system (Optec MicroMaster) used in this study has a small workstation including a KrF excimer laser, sophisticated beam delivery optics, a precision stage motion and a control software, as shown in figure 2. A KrF excimer laser with an ultraviolet wavelength of 248 nm, which has a relatively high optical photon energy leading to photochemical reaction [11], was used. The laser beam passes through an adjustable mask (xy) and then a projection lens to form a demagnified image ($x'y'$) on the sample. The demagnification $D = xy/x'y'$ is adjustable from 3 to 11. The fluence at the workpiece is determined by the energy of the laser and the demagnification and attenuation in the beam delivery optics of the laser ablation system. The laser is operated in a pulse mode with a repetition rate of 100 Hz and a pulse duration of 5–6 ns. The laser output energy was fixed at 10 mJ and the energy impinging on the sample was controlled using an optical attenuator incorporated in the system.

The circular mask has a diameter of 550 μm , and combined with a demagnification of 7.3 generated a 75 μm diameter spot on the workpiece. More details of the laser ablation process are described in the other literature [21]. Reactive ion etching with O_2 was used to remove carbon surface contamination. The oxygen plasma etching used a March Plasmod (March Plasma Systems) which utilizes an inductively coupled plasma (ICP). The system provides

isotropic etching to remove the target material uniformly in the complex-shaped electrode tip [6]. The RF (13.56 MHz) power and the pressure for the oxygen plasma etching were 150 W and 400 mTorr, respectively. This process does not require a mask for selective etching to remove carbon residue on the laser-ablated area only since it does not etch Parylene-C significantly.

The surface morphology of the samples after the laser deinsulation and the oxygen plasma treatment was examined by a SEM (FEI Quanta600 FEG) which was operated in a backscattered electron (BSE) mode under a high vacuum condition. Chemical and elemental analysis of the deinsulated spots was performed using an AxisUltraDLD XPS (Kratos Analytical) to examine the presence of iridium oxide, carbon and chlorine. The monochromatic x-ray source, Al K_{α} (180 W), was used and the analysis area was $110 \times 110 \mu\text{m}^2$ to collect spectra within the etched spot. The pass energy of 160 eV with 200 ms in dwell time and 1 eV in step was used for a survey scan, and the pass energy of 40 eV with 500 ms in dwell time and 0.1 eV in step was used for a high-resolution scan to improve the resolution and to reduce the background noise. The Utah electrode impedance was measured using a two-electrode method by poking the deinsulated electrodes into a conductive agarose gel and using an impedance meter (Blackrock Microsystems). The agarose gel was prepared from a mixture of phosphate-buffered saline and agarose powder in a weight ratio of 42:1. A platinum counter electrode probe was inserted in the gel. Impedances of individual electrodes were measured sequentially using a probe signal of 100 nA (peak to peak) at the frequency of 1 kHz between the electrode and Pt counter electrode.

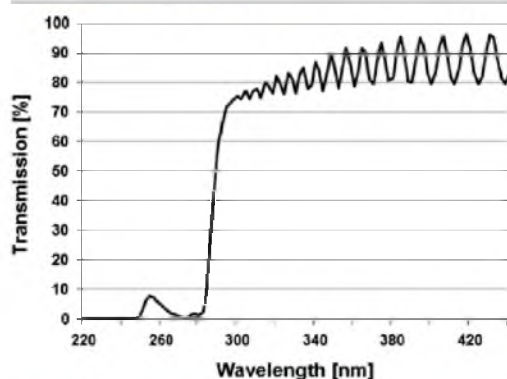


Figure 3. UV/Vis transmission characteristics of a 3 μm -thick Parylene-C film.

3. Result and discussion

A UV transmission spectrum through a 3 μm Parylene-C film measured using a variable angle spectroscopic ellipsometer (Woollam Spectroscopic) is shown in figure 3. The energy of the KrF excimer laser with the wavelength of 248 nm is strongly absorbed, which helps KrF excimer lasers be effective for laser ablation of Parylene-C.

The carbon residue after ablation of Parylene-C on a planar iridium oxide film was investigated by SEM and XPS. Figure 4(a) is a SEM image of a hole with a diameter of 200 μm on an iridium oxide film after laser ablation using a fluence of 1 J cm^{-2} and 100 pulses. The ablation conditions were optimized for the best deinsulation of Parylene-C without damaging the underlying iridium oxide film. Figure 4(b) is a backscattered electron (BSE) SEM image, which shows the boundary between bright (iridium oxide) and dark (Parylene) region indicating that the deinsulation was done thoroughly. Figure 4(c) is a magnified SEM image of the upper left region of figure 4(a), which also shows a distinct boundary between Parylene-C and iridium oxide film. The surface of the deinsulated area was investigated by XPS using an Al

K α anode. Figure 5 shows XPS spectra collected from a Parylene film and a laser ablated hole. The XPS spectrum from a sputter-cleaned Parylene film, shown in figure 5(a), has photoelectron peaks of C 1s, Cl 2p and Cl 2s associated with the Parylene film. The O 1s peak associated with physisorbed oxygen was not observed since it was removed by sputter cleaning with 2 keV Ar $^+$. The XPS from a laser-ablated spot measured with a pass energy of 160 eV, shown in figure 5(b), has peaks of Ir 4f and O 1s associated with the iridium oxide film and C 1s. The atomic concentrations of Ir, C and O were 1.9, 83.7 and 14.3%, respectively. Figure 5(c) shows a high-resolution XPS scan measured with a pass energy of 40 eV for the C 1s peak. The C 1s line has a full width half maximum (FWHM) of 1.57 eV. The C 1s peak is attributed to carbon residue produced by the laser ablation of Parylene since the atomic concentration and the FWHM of strictly adventitious carbon are in general below 15% and in the range from 1.0 eV to 1.4 eV, respectively. Absence of the chlorine peaks indicates that the Parylene-C was likely pyrolyzed and became a carbonaceous species.

In order to investigate the effect of the oxygen plasma etching on the surface of the laser ablated iridium oxide film, XPS was done again on samples exposed by the laser ablation followed by 1 min oxygen plasma etching. As shown in figure 6(a), a significantly smaller C 1s peak compared with that of a sample before the oxygen plasma etching was observed and an Ir 4d line showed up. A high-resolution XPS scan shown in figure 6(b) also reveals the Ir 4d peak and the significantly smaller C 1s peak. The estimated atomic concentration of the carbon peak is 14.8%, which is close to the value observed for the adventitious carbon. The results indicate that the carbon residue was effectively removed by the oxygen plasma treatment.

Figures 7(a) and (b) show imaging XPS data taken at the binding energy of the Ir 4f peak (60.3 eV) for the laser ablated sample before and after oxygen plasma treatment, respectively. Figures 7(c) and (d) show imaging XPS data taken at the binding energy of the C 1s peak (283.8 eV) for the laser ablated sample before and after oxygen plasma treatment, respectively. The Ir 4f imaging spots shown in figure 7(a) had the atomic concentration of 1.9% before oxygen plasma

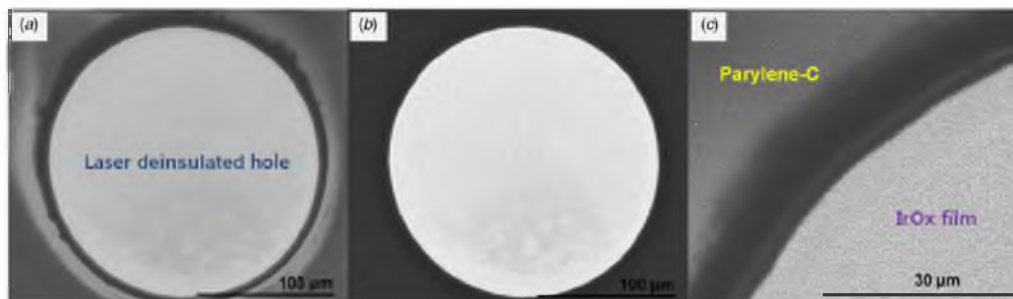


Figure 4. (a) SEM image of a 200 μm diameter hole on an iridium oxide film after laser ablation of 3 μm thickness Parylene-C film with a fluence of 1 J cm^{-2} and a number of pulses of 100, (b) backscattered electron (BSE) image of (a), and (c) magnified image at the boundary between Parylene-C and iridium oxide film.

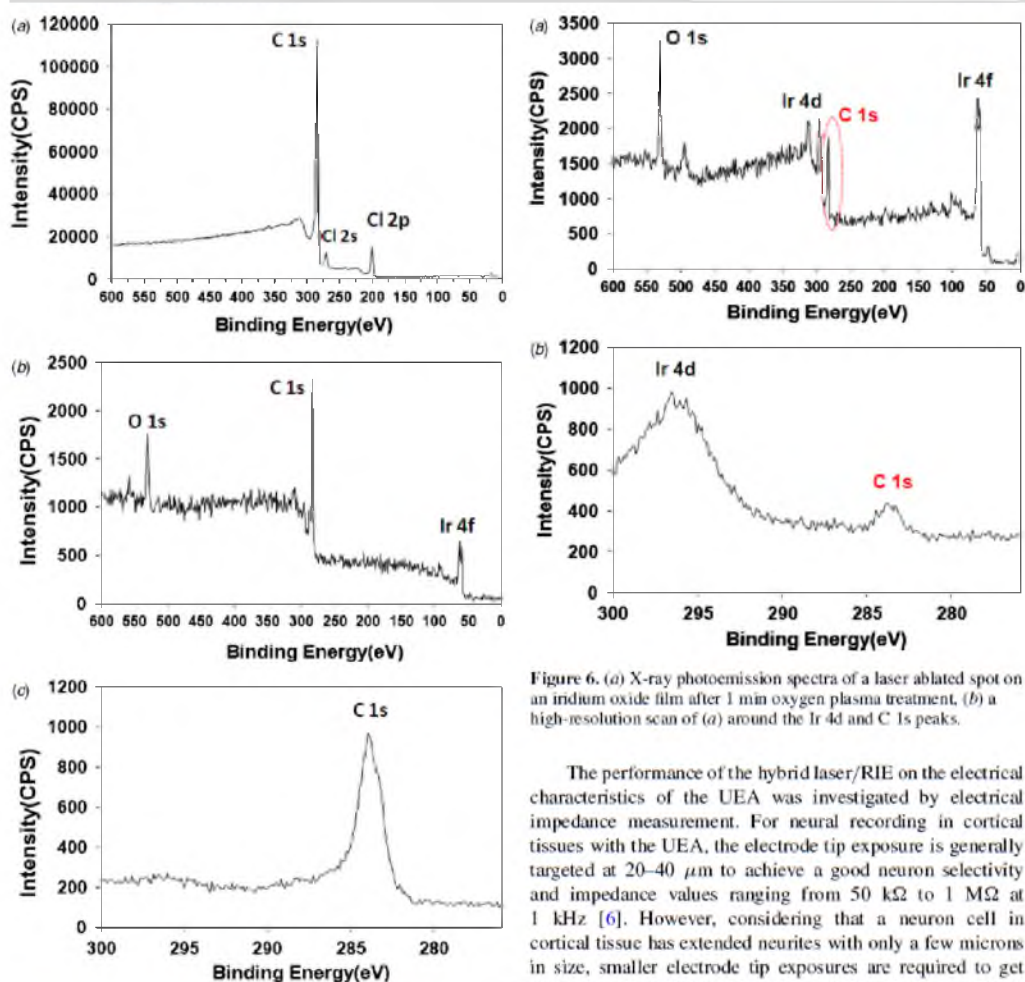


Figure 6. (a) X-ray photoemission spectra of a laser ablated spot on an iridium oxide film after 1 min oxygen plasma treatment, (b) a high-resolution scan of (a) around the Ir 4d and C 1s peaks.

Figure 5. X-ray photoemission spectra of (a) a Parylene film, (b) a laser ablated spot on an iridium oxide film and (c) a laser ablated spot on an iridium oxide film with high-resolution scan around the C 1s peak.

treatment. After 1 min oxygen plasma etching, as shown in figure 7(b), the intensity of the Ir 4f image became higher and the atomic concentration increased to 34.3%. On the other hand, the C 1s imaging spots shown in figure 7(c) had the atomic concentration of 83.6% before oxygen plasma treatment. After 1 min oxygen plasma etching, as shown in figure 7(d), the intensity of the C 1s image became lower and the atomic concentration decreased to 14.8%. The results indicate that the ICP oxygen plasma treatment can effectively remove the carbon residue on the deinsulated iridium oxide surface.

The performance of the hybrid laser/RIE on the electrical characteristics of the UEA was investigated by electrical impedance measurement. For neural recording in cortical tissues with the UEA, the electrode tip exposure is generally targeted at 20–40 μm to achieve a good neuron selectivity and impedance values ranging from 50 k Ω to 1 M Ω at 1 kHz [6]. However, considering that a neuron cell in cortical tissue has extended neurites with only a few microns in size, smaller electrode tip exposures are required to get more spatial resolution although it can degrade the sensitivity for stimulation and recording of small signals due to higher electrode impedance. In order to investigate the effects of the hybrid process on the performance of electrodes with an especially small tip exposures for the better selectivity, electrodes with two different tip exposures, 11–13 μm and 17–19 μm , were fabricated. The fluence and number of pulses for the electrode with a tip exposure of $\sim 12 \mu\text{m}$ were 750 mJ cm^{-2} and 200 and those for a tip exposure of $\sim 18 \mu\text{m}$ were 850 mJ cm^{-2} and 200, respectively. The effect of the oxygen plasma etching on the surface of the exposed electrode and the electrode impedance was investigated. Figure 8(a) shows a 30° tilted scanning electron micrograph of an electrode tip using a backscattered electron imaging right after laser ablation. The backscattered intensity on the sidewall of the active electrode is low due to carbon surface contamination, which is consistent with the XPS and BSE data from the planar structures. Figures 8(b) and (c) show images of the

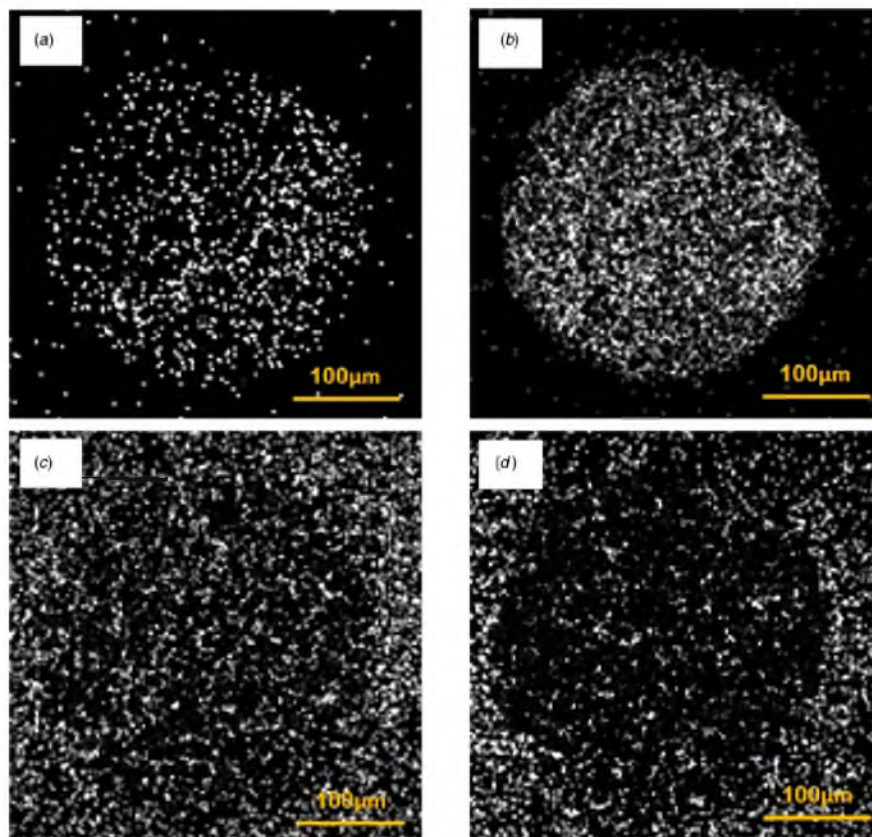


Figure 7. Imaging XPS data for (a) the Li 4f peak before oxygen plasma treatment, (b) the Ir 4f peak after 1 min oxygen plasma treatment, (c) the C 1s peak before oxygen plasma treatment, (d) the C 1s peak after 1 min oxygen plasma treatment.

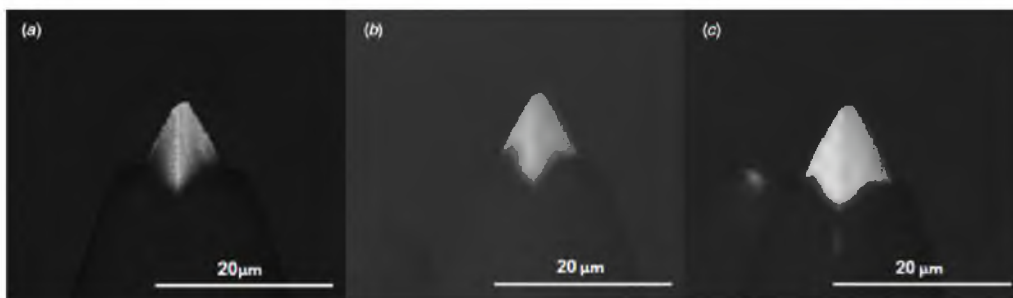


Figure 8. Scanning electron micrographs using backscattered electron imaging (a) after laser deinsulation using the fluence of 750 mJ cm^{-2} and the number of pulses of 200, (b) after laser deinsulation and 4 min oxygen plasma etching, (c) after laser deinsulation and 8 min oxygen plasma etching.

exposed electrode tips after the oxygen plasma etching of 4 and 8 min, respectively, revealing much higher backscattered electron intensity relative to the Parylene-C areas.

The etch rate of the Parylene-C by O_2 RIE was measured on 10 Utah electrodes. Figure 9(a) shows the etched thickness of the Parylene-C determined by measuring the horizontal

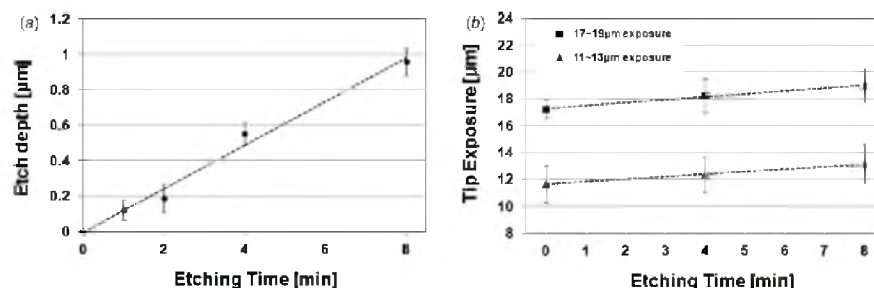


Figure 9. (a) Etch depth of the Parylene-C plotted as a function of RIE time, (b) tip exposures for electrodes with two different initial exposures of 11–13 μm and 17–19 μm as a function of RIE time.

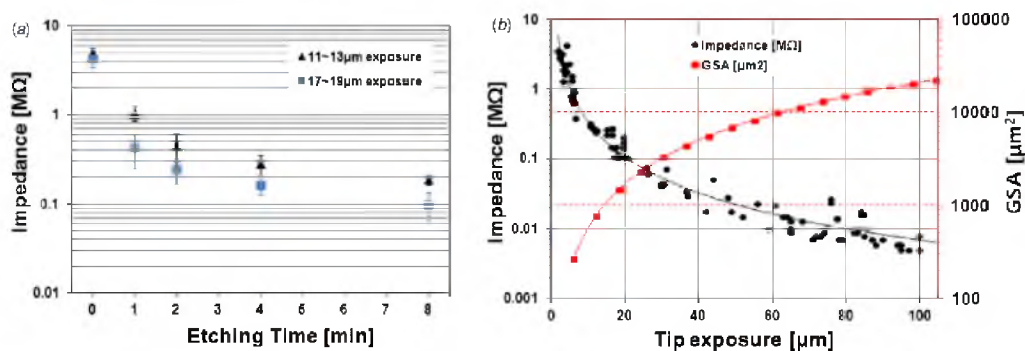


Figure 10. (a) Impedance of electrodes with initial tip exposures of 11–13 μm and 17–19 μm as a function of the oxygen plasma etch time, (b) impedance and GSA of electrodes fabricated by laser ablation and 2 min oxygen plasma etching. The solid line is the trend line ($y = 17.49x^{-1.70}$ and $R^2 = 0.97$ for impedance, $y = 15.32x^{1.57}$ and $R^2 = 0.99$ for GSA).

length of the Parylene-C in the spot located at 35 μm down from the tip end. The error bar represents the standard deviation (σ) of the measurements. The dotted line shows a trend line and the estimated Parylene-C etch rate is approximately 0.12 $\mu\text{m min}^{-1}$. The variation of the electrode tip exposures for electrodes with two different initial exposures of 11–13 μm and 17–19 μm as a function of the RIE etching time was measured and is shown in figure 9(b). The electrode tip exposure was defined as the average of minimum and maximum distances from the tip of the electrode to the edge of the deinsulated Parylene-C. The rate of tip exposure variation was $\sim 0.19 \mu\text{m min}^{-1}$ for the electrodes with the initial exposure of 11–13 μm and $\sim 0.22 \mu\text{m min}^{-1}$ for the electrodes with the initial exposure of 17–19 μm . The rate of tip exposure variation was larger than the Parylene-C etch rate, which indicates there exists thin sidewall residue of Parylene-C near the borderline of the Parylene-C.

The impedance of the electrodes with the two different initial exposures was measured as a function of the RIE etching time and presented in figure 10(a). The impedance value was a few MΩ immediately after laser ablation. After 1 min of RIE, the average impedance value of the two electrode

groups decreased from $\sim 4.6 \text{ M}\Omega$ to $\sim 0.7 \text{ M}\Omega$ and its standard deviation also decreased from $\sim 0.8 \text{ M}\Omega$ to $\sim 0.2 \text{ M}\Omega$. The average impedance value and its standard deviation saturated to $\sim 0.15 \text{ M}\Omega$ and $\sim 0.03 \text{ M}\Omega$ after 8 min of RIE. Figure 10(b) shows the impedance and geometrical surface area (GSA) values of Utah electrodes as a function of the tip exposure fabricated by the laser deinsulation and 2 min oxygen plasma etching. The GSA of the electrode was calculated assuming that the electrode tip is in the form of a cone. The radius and height of the cone were measured from SEM image. The solid line is a trend line with the equation $y = 17.49x^{-1.70}$ and the R -squared (R^2) value is 0.97 for impedance. The GSA has the equation $y = 15.32x^{1.57}$ and $R^2 = 0.99$. The impedance data were more correlated to the GSA rather than the tip exposure. Note that there exists some difference between the GSA and the real surface area due to surface roughness [21]. The electrode impedance value was larger than 1 MΩ for tip exposures smaller than $\sim 5 \mu\text{m}$ and approaches smaller than 10 kΩ as the tip exposure was increased beyond 100 μm . The results indicate that Utah electrode arrays with improved electrical characteristics can be fabricated by the hybrid laser and oxygen plasma etching of Parylene-C.

4. Conclusions

A hybrid Parylene-C etching method using a laser ablation followed by O_2 RIE was developed, and the performance and impedance when applied to Utah electrode arrays was investigated. The XPS spectra from planar samples showed that 1 min of the oxygen plasma etching is enough to remove significant amounts of carbon residue on the iridium oxide surface exposed by laser ablation. The average impedance value of Utah electrodes with initial electrode tip exposures of 11–13 μm and 17–19 μm decreased dramatically from $\sim 4.6\text{ M}\Omega$ to $\sim 0.7\text{ M}\Omega$ after 1 min oxygen plasma etching and became as low as $\sim 0.15\text{ M}\Omega$ after 8 min oxygen plasma etching. The tip exposure length was highly reproducible ($\sigma \leq 1.5\text{ }\mu\text{m}$) between electrode tips for the same laser deinsulation parameters. Furthermore, the deviation of impedance value for the same exposure was drastically decreased ($\sigma \leq 0.2\text{ M}\Omega$) even after 1 min oxygen plasma etching treatment. Compared with the conventional deinsulation method using oxygen plasma etching with an aluminum foil mask the laser deinsulation has advantages including an ability to control the deinsulation area precisely and to achieve smaller tip exposure ($\leq 20\text{ }\mu\text{m}$). Additionally, the laser deinsulation offers much smaller deviation ($\sigma \leq 0.2\text{ M}\Omega$) of electrode impedance than that ($\sigma > \sim 0.5\text{ M}\Omega$) of the conventionally deinsulated UEA caused by the nonuniformity of the tip exposure. The results indicate that the hybrid Parylene-C etching method is suitable for fabrication of low impedance Utah electrodes with small tip exposures for neural interface applications.

Acknowledgments

This work was supported by WCU (R31-2008-000-10026-0) and Bio-imaging Research Center programs at GIST, and DARPA award N66001-06-C-4056 and NIH (1R01NS064318-01A1). Sample fabrication, laser deinsulation and film characterization were performed in the Utah Nanofabrication Laboratory and Surface and Nanoimaging Laboratory at the University of Utah. I would like to thank Dr Brian van Devener and Kathryn Ecsedy for assistance in collecting XPS and SEM data and also appreciate the help from the UEA production team for the electrode arrays.

References

- [1] Cheung K 2007 Implantable microscale neural interfaces *Biomed. Microdevices* **9** 923–38
- [2] Bhandari R, Negi S, Rieth L, Normann R A and Solzbacher F 2008 A novel method of fabricating convoluted shaped electrode arrays for neural and retinal prostheses *Sensors Actuators A* **145–146** 123–30
- [3] Loch G E, Bak M J, Salzman M and Schmidt E M 1977 Parylene as a chronically stable, reproducible microelectrode insulator *IEEE Trans. Biomed. Eng.* **BME-24** 121–8
- [4] Rodger D C et al 2008 Flexible parylene-based multielectrode array technology for high-density neural stimulation and recording *Sensors Actuators B* **132** 449–60
- [5] von Metzner R P, Lass N, Ruther P and Stieglitz T 2011 Diffusion-limited deposition of Parylene C *J. Microelectromech. Syst.* **20** 239–50
- [6] Jui-Mei H, Rieth L, Normann R A, Tathireddy P and Solzbacher F 2009 Encapsulation of an integrated neural interface device with Parylene C *IEEE Trans. Biomed. Eng.* **56** 23–9
- [7] Ji J et al 2006 Microfabricated microneedle with porous tip for drug delivery *J. Micromech. Microeng.* **16** 958
- [8] Esashi M, Minami K and Shoji S 1991 Optical exposure systems for three-dimensional fabrication of microprobe *In: Micro Electro Mechanical Syst., (1991), MEMS' 91: Proc. An Investigation of Micro Structures, Sensors, Actuators, Machines and Robots. IEEE* pp 39–44
- [9] Loch G E, Peck R A and Martyniuk J 1995 Toward the ultimate metal microelectrode *J. Neurosci. Methods* **63** 175–83
- [10] Schmidt E M, Bak M J and Christensen P 1995 Laser exposure of Parylene-C insulated microelectrodes *J. Neurosci. Methods* **62** 89–92
- [11] Miller J C and Haglund R F 2009 *Laser Ablation and Desorption* vol 30 (New York: Academic Press)
- [12] Singleton D L, Paraskevopoulos G and Irwin R S 1989 XeCl laser ablation of polyimide: influence of ambient atmosphere on particulate and gaseous products *J. Appl. Phys.* **66** 3324–8
- [13] Branner A, Stein R B and Normann R A 2001 Selective stimulation of cat sciatic nerve using an array of varying-length microelectrodes *J. Neurophysiol.* **85** 1585–94
- [14] Rutten W L C 2002 Selective electrical interfaces with the nervous system *Annu. Rev. Biomed. Eng.* **4** 407–52
- [15] Lankard J R Sr and Wölbold G 1992 Excimer laser ablation of polyimide in a manufacturing facility *Appl. Phys. A* **54** 355–9
- [16] Brannon J H, Lankard J R, Baise A I, Burns F and Kaufman J 1985 Excimer laser etching of polyimide *J. Appl. Phys.* **58** 2036–43
- [17] Negi S, Bhandari R, Rieth L and Solzbacher F 2009 Effect of sputtering pressure on pulsed-DC sputtered iridium oxide films *Sensors Actuators B* **137** 370–8
- [18] Gorham W F 1966 A new, general synthetic method for the preparation of linear poly-p-xylylenes *J. Polym. Sci. A* **4** 3027–39
- [19] Campbell P K, Jones K E, Huber R J, Horch K W and Normann R A 1991 A silicon-based, three-dimensional neural interface: manufacturing processes for an intracortical electrode array *IEEE Trans. Biomed. Eng.* **38** 758–68
- [20] Bhandari R, Negi S, Rieth L and Solzbacher F 2010 A wafer-scale etching technique for high aspect ratio implantable MEMS structures *Sensors Actuators A* **162** 130–6
- [21] Yoo J-M, Sharma A, Tathireddy P, Rieth L W, Solzbacher F and Song J-I 2012 Excimer-laser deinsulation of Parylene-C coated Utah electrode array tips *Sensors Actuators B* **166–167** 777–86

CHAPTER 5

**EXCIMER LASER DEINSULATION OF PARYLENE-C
ON IRIIDIUM FOR USE IN AN ACTIVATED
IRIDIUM OXIDE FILM-COATED
UTAH ELECTRODE ARRAY**

Reprinted with permission from Journal of Neuroscience Methods

Volume 215, pp. 78 - 87, 2013



Contents lists available at SciVerse ScienceDirect

Journal of Neuroscience Methods

journal homepage: www.elsevier.com/locate/jneumeth

Clinical Neuroscience

Excimer laser deinsulation of Parylene-C on iridium for use in an activated iridium oxide film-coated Utah electrode array

Je-Min Yoo^{a,b,*}, Sandeep Negi^b, Prashant Tathireddy^b, Florian Solzbacher^b, Jong-In Song^{a,**}, Loren W. Rieth^{b,*}

^a Department of Nanobio Material and Electronics, Gwangju Institute of Science and Technology, Gwangju 500-712, Republic of Korea

^b Department of Electrical and Computer Engineering, University of Utah, Salt Lake City, UT, USA

HIGHLIGHTS

- ▶ The iridium film exhibits a much higher resistance to damage due to high laser power.
- ▶ The lower the laser fluence, the higher the humps of carbon debris.
- ▶ An electrode array tip laser ablated using a high fluence shows a distinctive boundary line between the exposure area and Parylene.
- ▶ Laser deinsulation of electrode tips with iridium film and subsequent activation of the iridium film are suitable for fabrication of high-performance silicon-based implantable devices.

ARTICLE INFO

Article history:

Received 15 September 2012

Received in revised form 6 February 2013

Accepted 12 February 2013

Keywords:

UEA
Iridium oxide
Parylene
Laser deinsulation
Photoablation
Excimer laser

ABSTRACT

Implantable microelectrodes provide a measure to electrically stimulate neurons in the brain and spinal cord and record their electrophysiological activity. A material with a high charge capacity such as activated or sputter-deposited iridium oxide film (AIROF or SIROF) is used as an interface. The Utah electrode array (UEA) uses SIROF for its interface material with neural tissue and oxygen plasma etching (OPE) with an aluminium foil mask to expose the active area, where the interface between the electrode and neural tissue is formed. However, deinsulation of Parylene-C using OPE has limitations, including the lack of uniformity in the exposed area and reproducibility. While the deinsulation of Parylene-C using an excimer laser is proven to be an alternative for overcoming the limitations, the iridium oxide (IrOx) suffers from fracture when high laser fluence (>1000 mJ/cm²) is used. Iridium (Ir), which has a much higher fracture resistance than IrOx, can be deposited before excimer laser deinsulation and then the exposed Ir film area can be activated by electrochemical treatment to acquire the AIROF. Characterisation of the laser-ablated Ir film and AIROF by surface analysis (X-ray photoelectron spectroscopy, scanning electron microscope, and atomic force microscope) and electrochemical analysis (electrochemical impedance spectroscopy, and cyclic voltammetry) shows that the damage on the Ir film induced by laser irradiation is significantly less than that on SIROF, and the AIROF has a high charge storage capacity. The results show the potential of the laser deinsulation technique for use in high performance AIROF-coated UEA fabrication.

© 2013 Elsevier B.V. All rights reserved.

1. Introduction

The electrical stimulation of cortical and other central nervous systems and recording of electrical signals from these systems require the use of penetrating microelectrodes to approach the

target neurons as closely as possible (Hochberg et al., 2006; Normann, 2007). As the geometric size of an electrode is reduced to achieve better selectivity, the current density required to deliver the necessary amount of stimulation charge increases. The electrode surface material that interfaces between the electrode and neural tissue should be able to transfer the electrical current between them efficiently. Transduction of the current can take place via either double-layer capacitive coupling or a Faradaic reaction (Agnew and McCreery, 1990). Noble metals, including platinum, iridium, gold, and palladium, which present a capacitive or pseudo-capacitive coupling transduction mechanism, have been selected as the material for neural stimulating electrodes because of their resistance to corrosion. These materials are also

* Corresponding author at: Department of Electrical and Computer Engineering, University of Utah, 505 Central Campus Drive, MEB 1690, Salt Lake City, UT 84112, USA. Tel.: +1 801 581 6941; fax: +1 801 581 5281.

** Corresponding author. Tel.: +82 62 715 2208.

E-mail addresses: Je-Min.Yoo@utah.edu (J.-M. Yoo), jsong@gist.ac.kr (J.-I. Song), loren.rieth@utah.edu (L.W. Rieth).

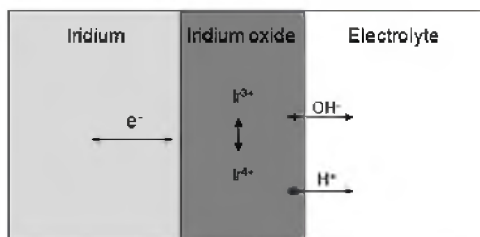


Fig. 1. Faradaic reaction of activated iridium oxide film.

desirable for long-term stimulation and recording applications because no chemical species are created or consumed during current stimulation. However, as the area of the electrode decreases, double-layer capacitive coupling alone is often insufficient to deliver the required charge. Materials with a Faradaic reaction transduction mechanism, where current transduction takes place through reduction and oxidation, can provide a much higher level of charge injection for the stimulation of neurons. Iridium oxide is the material with a Faradaic reaction transduction mechanism that displays the highest charge injection capacity, where the reduction and oxidation of iridium oxide film are primarily due to the valence change between Ir^{3+} and Ir^{4+} states (Cogan, 2008; Negi et al., 2010a).

There are two types of iridium oxide that are used for the fabrication of microelectrodes: activated and sputter-deposited iridium oxide film (AIROF and SIROF). AIROF is formed through electrochemical activation of the iridium film, and this reaction is accompanied by counter-ion (H^+ or OH^-) charge compensation from an electrolyte, as shown in Fig. 1. AIROF was the first iridium oxide film to receive attention as an oxide/chlorine catalyst in acid (Mozota and Conway, 1981) as well as for its resistance to corrosion (Johnson and Hench, 1977) and for use as an electrochromic material for display devices (Gottesfeld and McIntyre, 1979). Initially, iridium, along with other noble metals in the platinum metal group, had been studied as a neural interface material. However, activated iridium oxide was recognised as an alternative to these metals due to its higher charge storage capacity and corrosion resistance (Robblee et al., 1983). AIROF electrodes composed of iridium wire and sputtered iridium films on a silicon substrate are widely used for intracortical stimulation and recording applications. Silicon-based AIROF microelectrodes have been used as Michigan probes (Anderson et al., 1989) and in Utah electrode arrays (UEAs) (Negi et al., 2010b).

Another widely used type of iridium oxide film is SIROF, which is acquired via reactive sputtering of an iridium target in an oxidising plasma environment. SIROF exhibits cyclic voltammetric and charge storage capabilities comparable to AIROF, although its film characteristics are affected by the applied sputtering process parameters, including the deposition pressure, substrate bias, and sputtering gas composition (Negi et al., 2009).

There are various methods for removing insulation materials from microelectrodes (Fortin and Lu, 2002; Loeb et al., 1977; Schanze et al., 2007). It was recently reported that diffusion-limited deposition of Parylene on a neural probe allows electrode sites to be uncovered (von Metzner et al., 2011). However, this method is not appropriate for the deinsulation of UEAs to achieve controllable exposure and highly uniform impedance values on electrode tips. In UEAs, oxygen plasma etching (OPE) with an aluminium foil mask has conventionally been used to etch an insulation material, Parylene-C, from the electrode tip. The demand for the development of microelectrodes that exhibit sophisticated geometries with different electrode heights (Bhandari et al., 2008) in UEAs is

leading a shift of deinsulation methods from oxygen plasma etching using an aluminium foil mask to laser etching, as laser etching makes the deinsulation of individual tips in the UEA possible (Yoo et al., 2012a). Furthermore, the laser deinsulation process is attractive for the large-scale production of microelectrode arrays because it is less time consuming and highly reproducible. Although laser ablation of a polymer material presents the drawback of the redeposition of carbonaceous debris on and around the ablated site, the surface debris can be reduced by various methods, including the use of a shielding gas (Brannon et al., 1985; Kuper and Brannon, 1992), ultrasonic cleaning (Musaev et al., 2011) and dipping in a chemical solution. Oxygen plasma treatment after laser ablation is the other alternative to remove carbon debris (Yoo et al., 2012b). It is important to minimise the amount of residual carbon debris, as this debris potentially results in biocompatibility problems in long-term stimulation and recording applications through foreign body reactions.

The selection of the electrode surface material is particularly important because the laser deinsulation of Parylene-C can produce damage to the electrode surface material, including cracking, delamination, melting, and vapourisation. While a laser fluence lower than the threshold fluence value for damaging the electrode surface material can be used, ablation of Parylene-C at a low fluence can result in incomplete removal of this substance from the laser-ablated spot (Musaev et al., 2011), causing nonuniform exposure of deinsulated tips and high deviation in impedance values.

A higher laser fluence can improve the uniformity of the exposure of the deinsulated tip and can reduce the redeposition of residual carbon debris (Liu et al., 2012). When the laser fluence is high, the momentum of the ablated by-products is sufficiently high to allow them to escape from the ablation zone into the atmosphere, resulting in less redeposition. Thus, an electrode surface material that exhibits a high resistance to the damage induced by a high laser fluence is necessary to achieve uniform and repeatable electrode tip exposure. Iridium is one potential candidate for use as an electrode surface material. Iridium displays superior physical properties, such as a very high mass density ($22,560 \text{ kg m}^{-3}$), melting point (2466°C), and Young's modulus ($5.28 \times 10^{-8} \text{ kPa}$), compared with other metals in the platinum group, which makes it resistant to high laser power-induced damages. Furthermore, it can be easily deposited on silicon-based microelectrodes via sputtering and is therefore suitable for mass microfabrication. Finally, after being exposed through laser ablation, iridium can be converted to AIROF, which exhibits a high charge injection capacity.

In this study, we investigate the resistance of sputtered iridium and iridium oxide films against damage induced by laser power. Planar iridium and AIROF electrodes deinsulated via laser ablation were fabricated and characterised using surface analysis methods (X-ray photoelectron spectroscopy, scanning electron microscopy, and atomic force microscopy) and electrochemical techniques (electrochemical impedance spectroscopy and cyclic voltammetry). Based on the determined optimised electrochemical activation parameters, 3D UEA tips with AIROF were produced using laser deinsulation and characterised.

2. Materials and methods

To investigate the effect of the laser fluence on the damage to iridium film and SIROF, iridium film and SIROF were deposited on p-type (100) c-Si wafers using DC and reactive pulsed-DC sputter deposition systems (T-M Vacuum Super series), respectively. Iridium films with three different thicknesses (50, 200 and 600 nm) were deposited on a titanium adhesion layer (50 nm) at a deposition rate of 5 nm/min in an Ar gas ambient (at a flow rate of 150 sccm and a chamber pressure of 20 mTorr). The sputtering power was

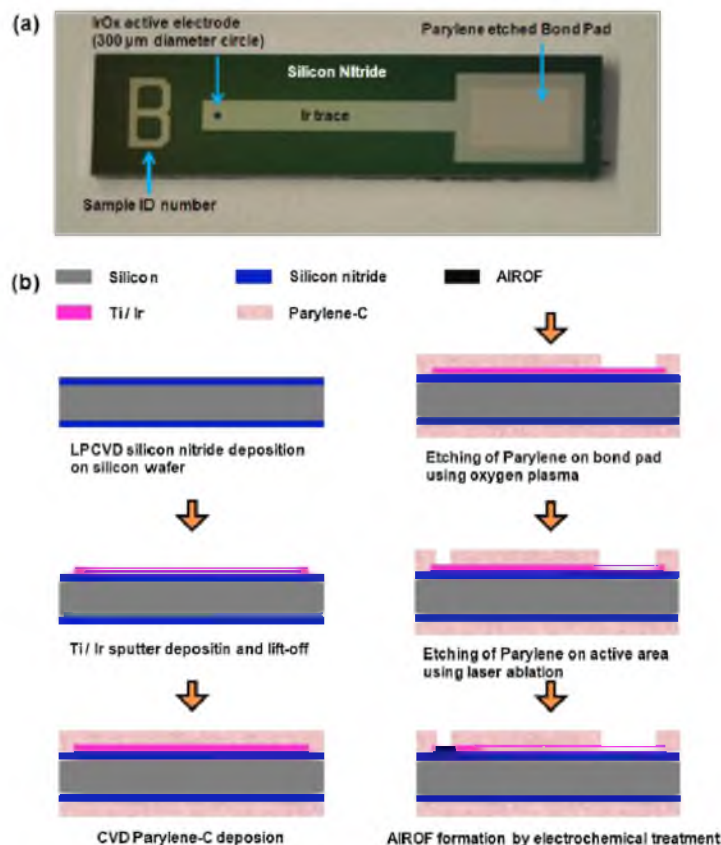


Fig. 2. (a) Planar view of the AIROF electrode and (b) schematic process flow for planar AIROF electrode fabrication.

90 W. SIROF was deposited with a deposition rate of 10 nm/min in an Ar and O₂ plasma ambient (flow rate of 100 sccm and chamber pressure of 10 mTorr). The sputtering power was 100 W.

Planar AIROF electrodes were also fabricated on *p*-type (100) *c*-Si wafers to investigate their electrochemical performance. Fig. 2 shows a planar view of and the fabrication process flow for the planar AIROF electrode (Negi et al., 2009). The Si wafer was deposited with a silicon nitride film acting as a dielectric insulation layer using a low-pressure chemical vapour deposition system. The film was grown for 2 h using ammonia and dichlorosilane gases with flow rates of 10 and 60 sccm, respectively. The pressure and temperature were 600 mTorr and 825 °C, respectively. Titanium (50 nm) and iridium (600 nm) films were deposited sequentially with a DC sputter deposition system. LOR 7B (MicroChem, Newton, MA) and positive photoresist (Shipley Microposit S-1813, Marlborough, MA) were used to pattern the metal films via a lift-off technique. Parylene-C (3 μm) was deposited through chemical vapour deposition using the Paratech 3000 laptop deposition system (Jui-Mei et al., 2009). To improve the chemical adhesion between Parylene and the substrate, an adhesion promoter, 0.5% Silquest A-174 silane (GE, Silicones), was used. The standard photolithography technique was employed to expose the Parylene-C to the bonding

pads, and the Parylene-C was then removed using a capacitively coupled plasma reactive ion etching (RIE) system (Oxford Plasmalab 80 plus). During RIE, an oxygen flow rate of 50 sccm, chamber pressure of 100 mTorr, and RF power and frequency of 75 W and 13.56 MHz, respectively, were employed. The etching time was 12 min. The Parylene film was removed from the active area of the electrode (diameter of 300 μm) using an excimer laser system with a wavelength of 248 nm (Optec MicroMaster). The exposed iridium in the active area was converted to AIROF in phosphate buffered saline (PBS) at a pH of 7.4. The composition of the PBS solution was as follows: 0.13 M NaCl, 0.022 M KH₂PO₄·H₂O, and 0.081 M Na₂HPO₄·7H₂O. Activation was achieved by applying rectangular pulses with a cathodic bias of −0.8 to −0.95 V and an anodic bias of 0.95 V with respect to the Ag/AgCl reference electrode in PBS solution to the exposed iridium film. The frequency of the pulses was 1 Hz, and 2000 cycles of pulses were applied (Negi et al., 2010b).

An AIROF Utah electrode array was fabricated through anodically oxidising Ir to AIROF following the removal of Parylene. The fabrication process for a Utah electrode array has been described in detail in other studies (Bhandari et al., 2010; Campbell et al., 1991). The same metallisation (Ti/Ir) used for the planar AIROF electrode was deposited on the electrode tips and then insulated with

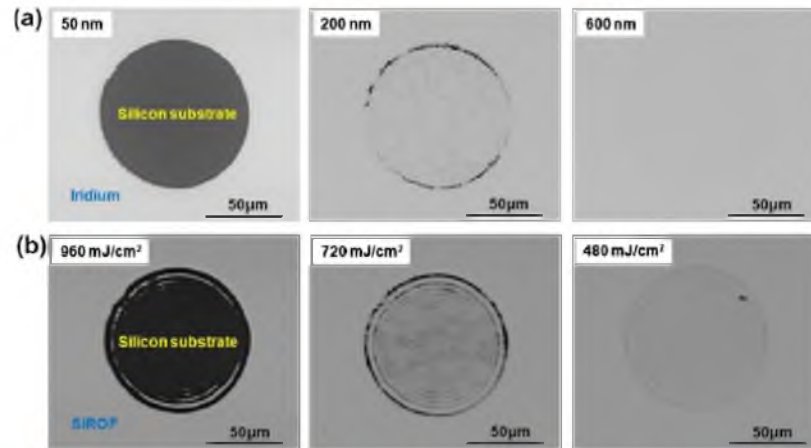


Fig. 3. (a) Backscattered SEM images of iridium films with three different thicknesses (50 nm, 200 nm, and 600 nm) exposed to 100 laser pulses with a fluence of 1920 mJ/cm². (b) Backscattered SEM images of SIROF (600 nm) exposed to different laser fluences (960, 720, and 480 mJ/cm²).

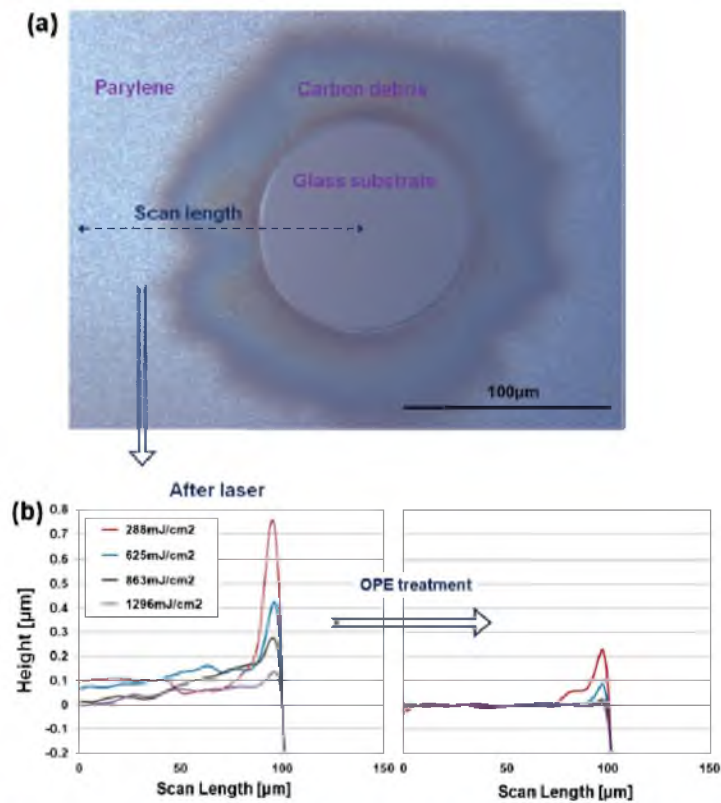


Fig. 4. (a) Optical image of a laser-ablated spot (diameter of 100 µm) on a soda-lime glass. (b) Surface profiles of the edges of circles ablated using different laser fluences (left) and after 2 min of OPE treatment (right).

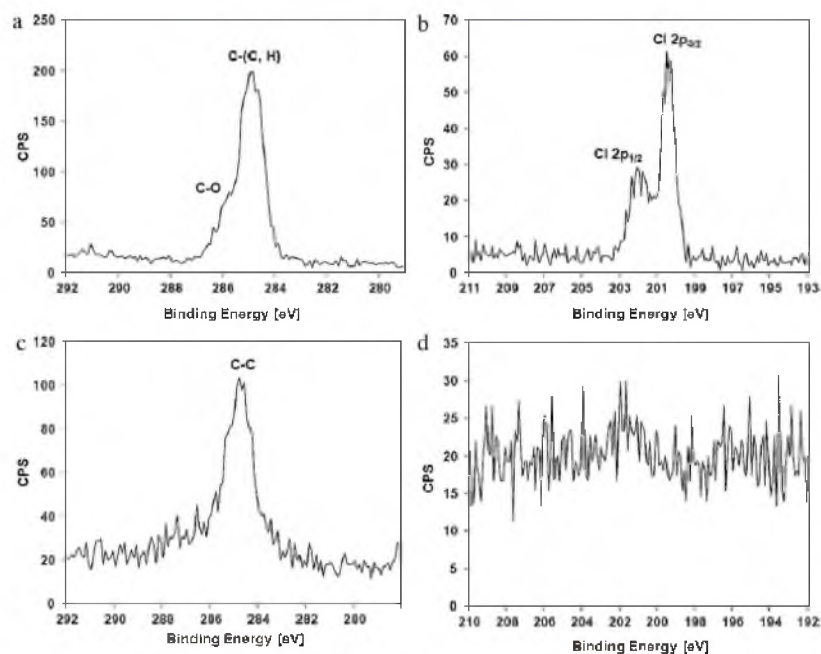


Fig. 5. X-ray photoemission spectra of (a) the C 1s peak of as-deposited Parylene-C, (b) the Cl 2p peak of as-deposited Parylene-C, (c) the C 1s peak of laser-ablated Parylene-C and (d) the Cl 2p peak of laser-ablated Parylene-C.

Parylene-C. The Parylene-C insulator material on the electrode tips was removed via focusing a demagnified excimer laser spot with a diameter of 70 μm on the Utah electrode tips. The laser pulses were 5 ns in duration, with a repetition rate of 100 Hz, and the laser fluence was 1500 mJ/cm^2 . The details of the laser ablation system are reported in Yoo et al. (2012a).

The morphology and roughness of the electrode surface before and after laser deinsulation were examined via scanning electron microscopy (SEM, FEI Quanta) and atomic force microscopy (AFM, Digital Instruments). Chemical and elemental analyses of the laser-ablated electrode surface were performed using XPS (Kratos Axis Ultra DLD) to examine the presence of residual carbon debris from laser-ablated Parylene. A monochromatic Al K α (180 W) X-ray source was employed, and the analysis was performed in a circular region with a diameter of 55 μm .

Sputter cleaning using 2 keV Ar⁺ was performed prior to XPS analysis to remove physisorbed oxygen on the film surface. Electrochemical impedance spectroscopy (EIS) and cyclic voltammetry (CV) were performed using the planar AIROF electrode in PBS solution to determine the impedance and charge storage capacity (CSC). The data were acquired using a computer-controlled commercial electrochemical test system (Gamry Instruments PC4 potentiostat). The Ag|AgCl electrode was used as a reference electrode, and a large-area Pt wire was used as a counter electrode. All potentials were measured with respect to the Ag|AgCl reference electrode. For the EIS measurements, sinusoidal signals with an amplitude of 10 mV and frequencies ranging from 1 Hz to 1 MHz were employed. Cyclic voltammograms were acquired for the potential limits of -0.6 V and 0.8 V with a sweep rate of 50 mV s^{-1} . Following common practice, the cathodal CSC (CSCc) was used to characterize the electrodes. The CSC was calculated from the time

integral for the cathodic current in a cyclic voltammogram over a potential range that is just within that of water electrolysis. For iridium oxide, the water electrolysis window was typically considered to be -0.6 V to 0.8 V with respect to the Ag|AgCl reference electrode.

3. Results and discussion

First, the effect of the laser fluence on the morphology of iridium film and SIROF was investigated. Fig. 3(a) shows backscattered SEM images of the iridium films with three different thicknesses (50 nm, 200 nm and 600 nm) exposed to 100 laser pulses with a fluence of 1920 mJ/cm^2 . While the iridium films with thickness of 50 and 200 nm showed cracks, there were no fractures observed on the iridium film with a thickness of 600 nm at a laser fluence of 1920 mJ/cm^2 . Fig. 3(b) shows backscattered SEM images of SIROF with a film thickness of 600 nm illuminated using 100 laser pulses with different laser fluences (960, 720, and 480 mJ/cm^2). As can be seen in the figure, the SIROF was damaged under laser fluences higher than 720 mJ/cm^2 . The results presented in Fig. 3 indicate that iridium film shows much a higher resistance against damage due to high laser power compared with SIROF.

Fig. 4(a) displays an optical image of a laser-ablated spot (diameter of 100 μm) formed on a polished soda-lime glass substrate coated with Parylene (thickness of 3 μm). While Parylene was clearly removed within the circle, debris remained around the edge of the circle. Fig. 4(b) provides the hump heights at the edge of circles ablated using different fluences (~290, 630, 860, and 1300 mJ/cm^2) immediately after laser ablation (left) and after 2 min of OPE treatment (right). The profiles were measured with a Tencor profilometer (Profilometer Tencor P-20H). The lower the

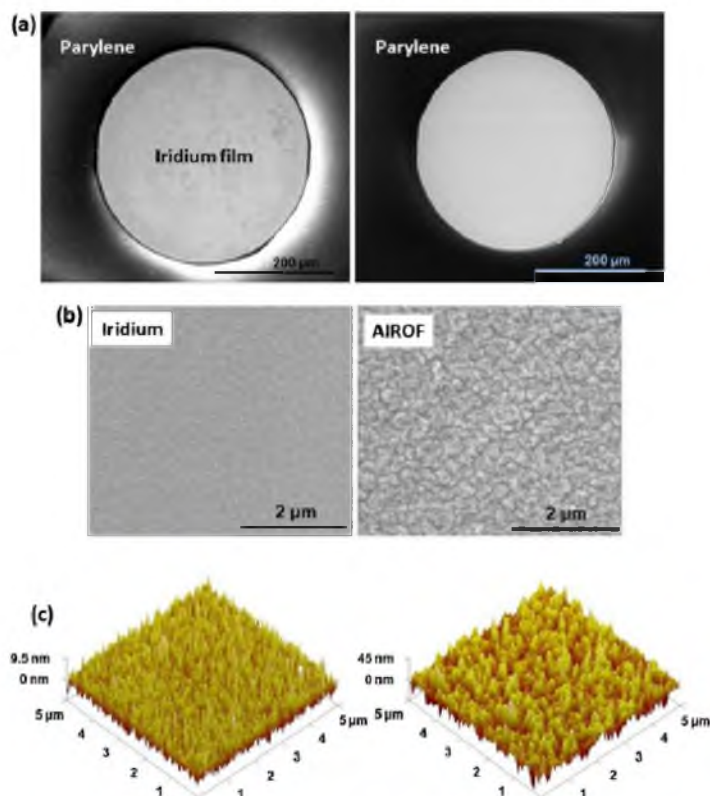


Fig. 6. (a) SEM images of laser deinsulated holes in a Parylene-coated iridium film before (left) and after (right) OPE treatment. (b) SEM images of iridium film (left) and AIROF film (right). (c) AFM images of iridium film (left) and AIROF film (right).

applied laser fluence, the higher the humps were found to be. During laser ablation, the laser breaks down Parylene into molecular fragments, and carbon debris is ejected from the ablation zone into the air. When the momentum of the carbon debris is not sufficient, it can be redeposited in the vicinity of the ablation area due to momentum exchange with the atmosphere. When the laser fluence is high, the momentum of the carbon debris can be sufficiently high to escape the ablation zone into the atmosphere, resulting in lower hump heights. The hump heights were decreased by OPE treatment. The carbon residue redeposited around the exposed area can potentially produce biocompatibility problems in long-term stimulation and recording applications due to foreign body reactions.

Fig. 5 provides the X-ray photoemission spectra of a planar iridium electrode sample coated with Parylene-C before and after laser ablation. As shown in Fig. 5(a) and (b), in the as-deposited Parylene-C, there are peaks corresponding to the rings and chain carbons of Parylene (C–C,H), oxygen contamination peaks (C–O) originating from water absorption on the surface, and spin orbit split Cl 2p peaks. Fig. 5(c) and (d) provides the X-ray photoemission spectra of the region of carbon debris shown in Fig. 4(a), revealing that the Parylene was decomposed, leaving carbon debris purely consisting of carbon elements (C–C) behind.

Based on the above experimental results, planar AIROF electrodes were fabricated and characterised. Laser deinsulation of a 300 μm-diameter circle on iridium film (thickness of 600 nm) coated with Parylene (thickness of 3 μm) was performed using laser pulses of 50 with a fluence of 1500 mJ/cm². Fig. 6(a) shows SEM images of the laser-deinsulated circle immediately after laser illumination (left) and after 2 min of subsequent OPE treatment (right). Activation of iridium film to produce AIROF was achieved by applying rectangular pulses (with levels of –0.8 and 0.95 V with respect to the Ag/AgCl reference electrode) in PBS solution. Two thousand cycles of pulses with a repetition rate of 1 Hz were applied. Fig. 6(b) shows SEM images of iridium film (left) and AIROF (right). After activation, the roughness of the film was increased. Fig. 6(c) shows AFM images of iridium film (left) with an rms roughness of 2.7 nm and AIROF (right) with an rms roughness of 11.3 nm.

Fig. 7(a) and (b) provides the X-ray photoemission spectra obtained before the electrochemical activation of the iridium film, and Fig. 7(c) and (d) provides those of AIROF. Fig. 7(a) shows sharp peaks for spin orbit split Ir 4f. However, as shown in Fig. 7(b), there was no O 1s peak. On the other hand, Fig. 7(c) shows broadened Ir 4f peaks, and Fig. 7(d) shows an apparent O 1s peak. Because the AIROF sample contained iridium atoms of different valences in tetravalent

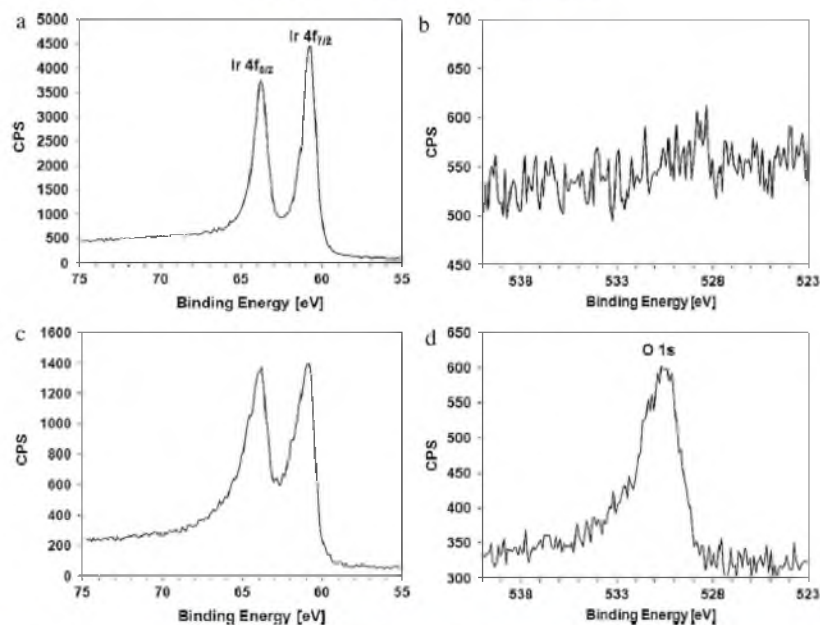


Fig. 7. X-ray photoemission spectra showing (a) the Ir 4f peak for the as-deposited iridium film, (b) the O 1s peak for the as-deposited iridium film, (c) the Ir 4f peak of the AIROF and (d) the O 1s peak of the AIROF.

or trivalent form, the full-width half-maximum (1.25 eV) of Ir 4f_{7/2} in AIROF was wider than that (0.9 eV) of pure iridium. The broadened asymmetric O 1s peak shown in Fig. 7(d) can be attributed to hydroxides, adsorbed water, or water from hydration (Kodintsev et al., 1992).

Fig. 8(a) shows SEM images of AIROF produced using rectangular pulse levels of -0.85 and 0.95 V (left), -0.9 and 0.95 V (centre), and -0.95 and 0.95 V (right). Among the many parameters of the activation pulse signal for the growth of AIROF, including the anodic/cathodic voltage, ramp-up rate, dwell time, and number of

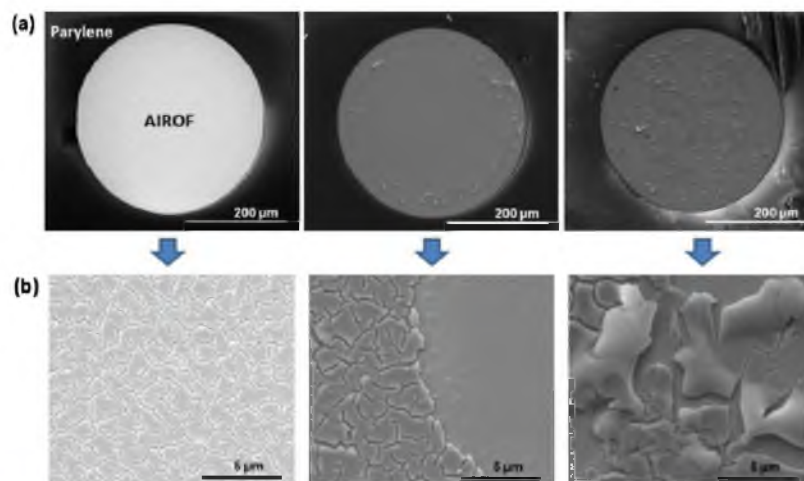


Fig. 8. (a) SEM images of AIROF produced using rectangular pulse levels of -0.85 and 0.95 V (left), -0.9 and 0.95 V (centre), and -0.95 and 0.95 V (right); (b) Magnified images of (a).

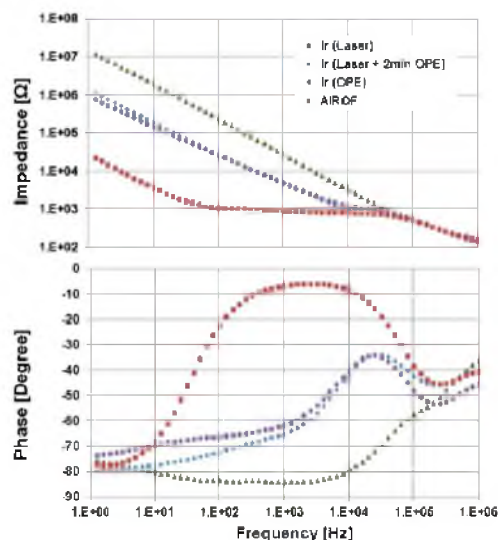


Fig. 9. Amplitude (upper) and phase (bottom) of the impedance of planar electrodes with an iridium active area formed using three different deinsulation conditions and with an AIROF active area (area of the active region = $70,600 \mu\text{m}^2$).

pulses, the cathodic voltage was analysed in detail because it is one of the most critical parameters for tuning the film growth rate (Pickup and Birss, 1987). A crack started to appear the AIROF at a cathodic voltage of -0.85 V , and the degradation of the film morphology became more severe as the cathodic voltage became more negative, as shown in Fig. 8(b). The AIROF partially flaked off at -0.9 V and completely flaked off at -0.95 V . Behaviour similar to that of the AIROF fabricated on wire-type iridium electrodes has previously been reported (Cogan et al., 2004). Although the AIROF activated using pulse levels of -0.8 and 0.95 V showed a stable morphology without cracks, a long-term analysis of the stimulation of AIROF electrodes under an in vivo environment is required for chronic implantation applications.

The Bode plot of the impedance values for planar electrodes with an iridium active area and AIROF active area are presented in Fig. 9. The active area was circular in shape and has a diameter of $300 \mu\text{m}$ (geometric area of approximately $70,600 \mu\text{m}^2$). The thickness of the iridium film was 600 nm . The active area was exposed via deinsulation of Parylene using laser pulses of 50 with a fluence of $1500 \text{ nJ}/\text{cm}^2$. The impedance of the planar iridium electrode fabricated through laser ablation only was $28 \text{ k}\Omega$ at 1 kHz . However, it was decreased significantly, down to $\sim 5 \text{ k}\Omega$, by 2 min of subsequent OPE treatment. This value was similar to that of an electrode fabricated only via OPE deinsulation (for 12 min). After the activation of iridium, the impedance decreased to $\sim 0.9 \text{ k}\Omega$. The impedance of the planar iridium electrode showed a capacitor-like frequency dependence, indicating that the current transduction mechanism in this case is capacitive coupling. On the other hand, the impedance of the planar AIROF electrode showed resistive behaviour for the frequency range from 50 Hz to 50 kHz . The impedances converged at a frequency range over 50 kHz , which indicates the effect of PBS impedance. The results indicate that the planar AIROF electrode fabricated using the hybrid deinsulation method (laser deinsulation followed by 2 min of OPE) (Yoo et al., 2012b) shows resistive behaviour and provides much lower impedance.

Cyclic voltammograms for the planar iridium electrode fabricated via laser ablation followed by 2 min of OPE and the planar AIROF electrode, measured in PBS solution, are illustrated in Fig. 10. The voltammogram for the planar iridium electrode exhibited an approximately rectangular shape, which is expected for an electrode presenting a double-layer capacitive coupling transduction mechanism. However, the voltammogram for the planar AIROF electrode showed main current peaks at 0.25 V and -0.21 V , corresponding to reversible Ir^{3+} and Ir^{4+} redox reactions, respectively. The CSCC was $3.5 \text{ mC}/\text{cm}^2$ for the planar iridium electrode and $10 \text{ mC}/\text{cm}^2$ for the planar AIROF electrode. The much higher charge storage capacity of the planar AIROF electrode is attributed to its Faradaic transduction mechanism.

Fig. 11(a) shows the Utah electrode array tips fabricated through laser deinsulation using 100 pulses with a fluence of $1500 \text{ nJ}/\text{cm}^2$ on iridium (left) and 500 pulses with a fluence of $700 \text{ nJ}/\text{cm}^2$

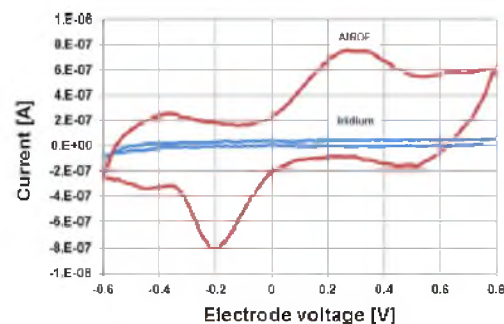


Fig. 10. Cyclic voltammograms for the planar iridium and AIROF electrodes (area of the active region = $70,600 \mu\text{m}^2$). The electrode voltage was measured with respect to the Ag/AgCl reference electrode.

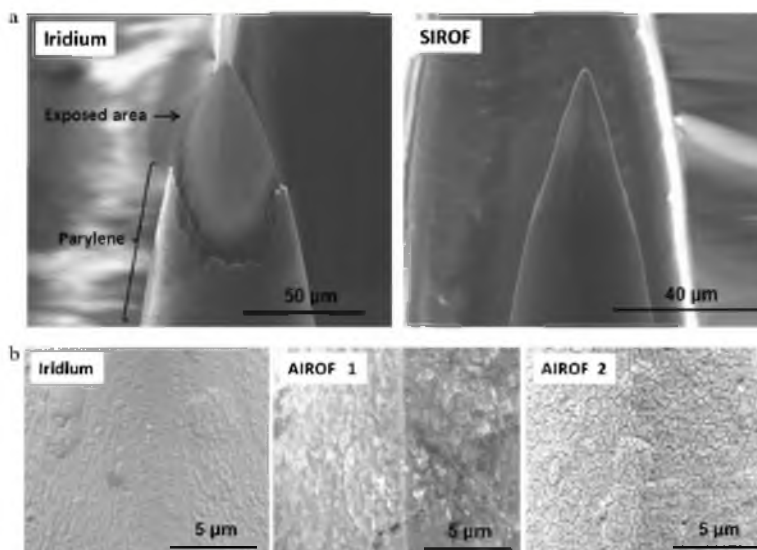


Fig. 11. (a) SEM images of laser-deinsulated Utah electrode array tips with iridium film (left) and SIROF (right). (b) SEM images of an as-deposited iridium film (left), AIROF activated using rectangular pulses with levels of -0.8 and 0.95 V (centre), and AIROF activated using rectangular pulses with levels of -0.85 and 0.95 V (right).

on SIROF (right). The laser-ablated electrode array tip produced using a high fluence (100 pulses and a fluence of 1500 mJ/cm^2) showed a distinctive boundary line between the exposure area and Parylene, and the deinsulated iridium surface looked clean. On the

other hand, the laser-ablated electrode array tip generated using a low fluence (500 pulses with a fluence of 700 mJ/cm^2) exhibited an indistinct boundary and insufficiently etched Parylene on the sidewall of the tip. A low laser fluence of 700 mJ/cm^2 was used to prevent fractures in the SIROF, which resulted in nonuniform removal of Parylene and, thus, a high impedance value as well as large variation between electrode tips. Fig. 11(b) shows SEM images of the as-deposited iridium film (left), AIROF activated using rectangular pulses with levels of -0.8 and 0.95 V (centre), and AIROF activated using rectangular pulses with levels of -0.85 and -0.95 V (right). The morphological change in the AIROF fabricated via the activation of iridium film on Utah electrode array tips for different bias conditions was similar to that for the planar electrodes.

Bode plots of the impedance of the AIROF Utah electrode are presented in Fig. 12(a). The geometrical surface area of the electrode tip with an exposure of $60 \mu\text{m}$ was calculated to be approximately $6000 \mu\text{m}^2$, assuming that the tip was identical to a cone (Negi et al., 2010a). The impedance of the AIROF UEA tip was $\sim 3 \text{ k}\Omega$ for the frequency range of 10^1 to 10^5 Hz. The behaviour of the AIROF UEA tip characterised through EIS and CV was similar to that of the planar AIROF electrode. The CSCc calculated using CV was $\sim 16 \text{ mC/cm}^2$, which agrees well with the value reported in the literature (Cogan, 2008).

4. Conclusions

The characteristics of AIROF-coated UEA tips deinsulated via laser ablation were investigated. Unlike UEA tips produced using SIROF, UEA tips with Ir can be deinsulated using a high laser fluence to achieve a low electrochemical impedance value and high charge storage capacity. The results indicate that laser deinsulation of electrode tips with iridium film and subsequent activation of the iridium film represents a suitable method for the fabrication of high-performance silicon-based implantable devices.

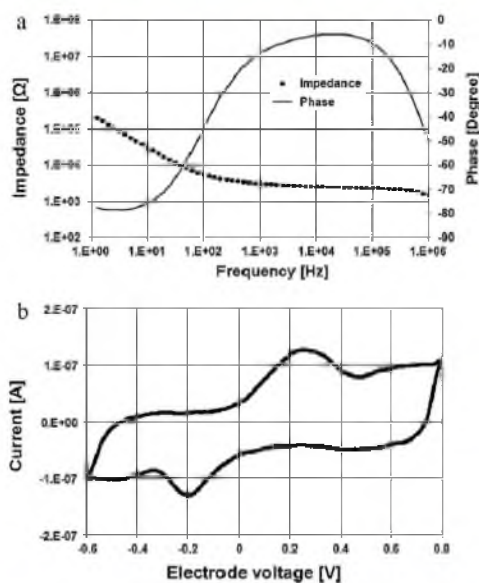


Fig. 12. EIS (a) and CV (b) of the AIROF Utah microelectrode (geometric surface area $\approx 6000 \mu\text{m}^2$).

Acknowledgements

This work was supported by the WCU (R31-2008-000-10026-0) and Bio-imaging Research Program at GIST and DARPA award N66001-06-C-4056 and NIH (1R01NS064318-01A1). Sample fabrication, laser deinsulation, and film characterisation were performed in the Utah Nanofabrication Laboratory and Surface and Nanoimaging Laboratory of the University of Utah. We would like to thank Dr. Brian van Devener for assistance in collecting XPS and SEM data, and we also appreciate the help of the UEA production team with the electrode arrays. Sandeep Negi has a financial interest in the company Blackrock Microsystems, which develops and produces implantable neural interfaces and electrophysiological equipment and software.

References

- Agnew WF, McCreery DB. *Neural prostheses: fundamental studies*. Englewood Cliffs, NJ: Prentice Hall; 1990.
- Anderson DJ, Najafi K, Tanghe SJ, Evans DA, Levy KI, Heike JF, et al. Batch fabricated thin-film electrodes for stimulation of the central auditory system. *IEEE Trans Biomed Eng* 1989;36:693–704.
- Bhandari R, Negi S, Rieth L, Normann RA, Solzbacher F. A novel method of fabricating convoluted shaped electrode arrays for neural and retinal prostheses. *Sens Actuators A: Phys* 2008; 145–146:123–30.
- Bhandari R, Negi S, Rieth L, Solzbacher F. A wafer-scale etching technique for high aspect ratio implantable MEMS structures. *Sens Actuators A: Phys* 2010;162:130–6.
- Brannon JH, Lankard JR, Baise AI, Burns F, Kaufman J. Excimer laser etching of polyimide. *J Appl Phys* 1985;58:2136–43.
- Campbell PK, Jones KE, Huber RJ, Houch KW, Normann RA. A silicon-based, three dimensional neural interface: manufacturing processes for an intra cortical electrode array. *IEEE Trans Biomed Eng* 1991;38(38):758–68.
- Cogan SF. Neural stimulation and recording electrodes. *Annu Rev Biomed Eng* 2008; 10:275–308.
- Cogan SF, Cuzzellian AA, Agnew WF, Yuen TGH, McCreery DB. Over-pulsing degrades activated iridium oxide films used for intracortical neural stimulation. *J Neurosci Methods* 2004; 137:141–50.
- Fortin JB, Lu TM. A model for the chemical vapor deposition of poly(para-xylene) (Parylene) thin films. *Chem Mater* 2002;14:1945–9.
- Gottesfeld S, McIntyre JDE. Electrochromism in anodic iridium oxide films. *J Electrochem Soc* 1979;126:742–50.
- Hochberg LR, Serruya MD, Friehs GM, Mukand JA, Saleh M, Caplan AH, et al. Neuronal ensemble control of prosthetic devices by a human with tetraplegia. *Nature* 2006;442:164–71.
- Johnson FF, Hensch LL. An in vitro analysis of metal electrodes for use in the neural environment. *Brain Behav Evol* 1977; 14:23–45.
- Jui-Mei H, Rieth L, Normann RA, Tathireddy P, Solzbacher F. Encapsulation of an integrated neural interface device with Parylene-C. *IEEE Trans Biomed Eng* 2009;56:23–9.
- Kodintsev IM, Trasatti S, Rubel M, Wlcekowski A, Kaulther N. X-ray photoelectron spectroscopy and electrochemical surface characterization of iridium(IV) oxide + ruthenium(IV) oxide electrodes. *Langmuir* 1992;8:283–90.
- Kuper S, Brannon J. Ambient gas effects on debris formed during KrF laser ablation of polyimide. *Appl Phys Lett* 1992;60:1633–5.
- Liu K, Nickolov Z, Oh J, Noh HM. KrF excimer laser micromachining of MEMS materials: characterization and applications. *J Micromech Microeng* 2012;22:015012.
- Lueh GE, Bak MJ, Salzman M, Schmidt EM. Parylene as a chronically stable, reproducible microelectrode insulator. *IEEE Trans Biomed Eng* 1977;BME-24:121–8.
- Mozota J, Conway BE. Modification of apparent electrocatalysis for anodic chlorine evolution on electrochemically conditioned oxide films at iridium anodes. *J Electrochem Soc* 1981; 128:2142–9.
- Musaev D, Scott P, Wrobel J, Wolf J, Kruger M. UV laser ablation of Parylene films from gold substrates. *J Mater Sci* 2011;46:183–7.
- Negi S, Bhandari R, Rieth L, Solzbacher F. Effect of sputtering pressure on pulsed-DC sputtered iridium oxide films. *Sens Actuators B: Chem* 2009; 137:370–8.
- Negi S, Bhandari R, Rieth L, Solzbacher F. In vitro comparison of sputtered iridium oxide and platinum-coated neural implantable microelectrode arrays. *Biomed Mater* 2010a;5:015007.
- Negi S, Bhandari R, Rieth L, Wagenen RW, Solzbacher F. Neural electrode degradation from continuous electrical stimulation: comparison of sputtered and activated iridium oxide. *J Neurosci Methods* 2010b;8–17.
- Normann RA. Technology insight: future neuroprosthetic therapies for disorders of the nervous system. *Nat Clin Pract Neurol* 2007;3:444–52.
- Pickup FG, Birss VI. A model for anodic hydrous oxide growth at iridium. *J Electroanal Chem Interf* 1987;220:83–100.
- Reibler LS, Lefko JL, Brummer SB. Activated Ir: An electrode suitable for reversible charge injection in saline solution. *J Electrochem Soc* 1983; 130:731–3.
- Scharze T, Hesse L, Lau C, Greve N, Haberer W, Kammer S, et al. An optically powered single-channel stimulation implant as test system for chronic biocompatibility and biostability of miniaturized retinal vision prostheses. *IEEE Trans Biomed Eng* 2007;54:983–92.
- von Metzner RP, Lass N, Rulher P, Stieglitz T. Diffusion-limited deposition of Parylene C. *J Micromech Syst* 2011; 20:239–50.
- Yoo J-M, Sharma A, Tathireddy P, Rieth LW, Solzbacher F, Song J-I. Excimer-laser deinsulation of Parylene-C coated Utah electrode array tips. *Sens Actuators B: Chem* 2012a; 166–167:777–86.
- Yoo J-M, Song J-I, Tathireddy P, Solzbacher F, Rieth LW. Hybrid laser and reactive ion etching of Parylene-C for deinsulation of a Utah electrode array. *J Micromech Microeng* 2012b;22:105035.

CHAPTER 6

REDUCTION OF IRIIDIUM OXIDE FILM FOR LASER DEINSULATION OF UTAH ELECTRODE ARRAY

This Chapter will be submitted to Biosensors and Bioelectronics, 2013. Authors are Je-
Min Yoo, Prashant Tathireddy, Loren W Rieth, Jong-In Song and Florian Solzbacher.

6.1 Abstract

Tip deinsulation of Parylene-C coated Utah electrode array (UEA) is typically performed by a reactive ion etching using aluminum foil mask. However, it has limitations resulting in nonuniform impedance ($\sigma > 0.5 \text{ M}\Omega$) of the exposed tip and the time-consuming process of aluminum poking on the array. Laser ablation can be an alternative to deinsulate electrode tips; however, the sputtered deposited iridium oxide film (SIROF) on the UEA tip is mechanically weak for high laser fluence ($> 1 \text{ J/cm}^2$) which causes damage of the film. In this paper, a partially deoxidized SIROF by annealing under $210 \text{ }^\circ\text{C}$ in forming gas (98% Ar and 2% H_2) was used to get a highly tolerable film to damage by laser. The deinsulated electrode surfaces were characterized by scanning electron microscope, atomic force spectroscopy, X-ray diffraction, X-ray photoelectron spectroscopy, and electrochemical analysis (electrochemical impedance spectroscopy, cyclic voltammetry, and potential transient). The results suggest that the laser ablation on partially deoxidized SIROF is promising for deinsulation of UEAs.

6.2 Introduction

Utah electrode array (UEA) is one of the major implantable electrodes that is based on silicon microfabrication technology. It is insulated using a biocompatible Parylene-C on the inactive areas to protect both the electrode sites and the neural tissues [1, 2]. The insulated electrodes require a removal of the Parylene from the active electrode tips to record neural signals or stimulate neurons. The deinsulation of implantable electrodes is an issue due to drawbacks of existing methods. The heating or high voltage methods usually lead to breakdown near the tips or poor adhesion of Parylene [3]. The wet etching is not adaptable because of the chemical inertness of

Parylene-C. In recent years, a method of diffusion-limited deposition (DLD) of Parylene-C was reported that allows uncovered electrode sites on neural probes [4]; however, the process is complex and hard to apply in electrodes with complicated electrode geometries such as Utah slanted electrode array (USEA). The deinsulation of Parylene-C coated UEA tips is conventionally performed by a reactive ion etching (RIE) using aluminum foil mask as etching mask [5]. However, the poking of an aluminum foil mask on electrode array is a time-consuming process and the impedance of electrodes within the UEA has a large deviation ($\sigma > 0.5 \text{ M}\Omega$) due to the nonuniformity of the tip exposure. The laser deinsulation technique is an alternative to get over the limitations in the RIE method [6, 7]. However, a sputter deposited iridium oxide film (SIROF) is easily damaged at high laser fluences ($> 1 \text{ J/cm}^2$). Even if low laser fluence can be used to prevent film damages of iridium oxide, it can cause a nonuniform exposure of the electrode tip and potential biocompatibility problems from the carbon residue redeposited around the exposed area [8]. The mechanically weak property of as-deposited SIROF is an obstacle to directly use the laser ablation on the film.

Iridium oxide (IrO_x) film is deoxidized under a certain annealing condition by breaking its bonds, as expressed in equation (1).



It is reported that IrO_2 is easily reduced even at low temperatures when it is exposed to low pressure, and the thermodynamic behavior of the deoxidized IrO_2 film as a relationship between temperature and environmental oxygen-pressure was studied [9, 10]. Environmental gas affects the deoxidization phenomenon; for example, iridium oxide

film is easily reduced under a forming gas (5% H₂ in Ar) at temperatures ranging from 100 °C to 300 °C [11]. The oxygen reduced iridium oxide film gives rise to iridium on top of the film, which is the hardest, densest, and the most corrosion-resistant metal. The film can be highly tolerable to damage induced by laser due to its physical properties [8].

Titanium (Ti) is widely used as an adhesion layer in thin film microfabrication technology. However, the property can be easily changed to an oxide by plasma oxidation during the sputter process, such as a reactive deposition of SIROF using O₂ plasma on top of the Ti film [12]. On the other hand, the possibility cannot be ruled out that an oxidation by oxygen diffusion from IrO_x to the underneath adhesion layer of Ti is due to the high reactivity of titanium with oxygen under high temperature [13].

In this work, we first investigated the deoxidization phenomenon of SIROF by an annealing process under forming and nitrogen gases that was characterized by thermogravimetric analysis (TGA), X-ray diffraction (XRD), scanning electron microscopy (SEM), and atomic force microscope (AFM). The diffusion of oxygen from SIROF to Ti film by the annealing process was analyzed by X-ray photoelectron spectroscopy (XPS). Planar SIROF electrodes deinsulated by laser ablation were fabricated and characterized by electrochemical techniques (electrochemical impedance spectroscopy, cyclic voltammetry, and potential transient). Based on the optimized annealing and films structure from the test of planar electrodes, UEAs of a partially deoxidized IrO_x film with a diffusion barrier Ir between Ti and SIROF were implemented using laser deinsulation and characterized.

6.3 Material and Methods

To investigate the influence of temperature and environmental gas on deoxidization of SIROF, TGA (TA Q500) was performed under nitrogen and forming gas (2% H₂ and 98% Ar). The temperature was scanned from 30 °C to 1000 °C at the heating rate of 15 °C/minute. The weight of IrO_x powder that was extracted from SIROF on silicon substrate was 3.3 mg for nitrogen gas and 2.7 mg for forming gas. SIROF was deposited on *p*-type (100) Si wafers by a pulsed DC sputter deposition system (TMV Super Series SS-40C-IV Multi Cathode Sputtering System) in Ar and O₂ plasma with each flow rate of 100 sccm and at the RF power of 100 W and the pressure of 10 mTorr. The deposition rate was 10 nm/minute. Crystallization and the intensity of Ir after deoxidization by different annealing temperature (410, 310, 220, and 210 °C) were examined by XRD using Cu K α radiation. Ti (100 nm) / Ir (80 nm) / SIROF (700 nm) film stacks on silicon wafer were used to follow the same film stacks of the test structure that is described later. Ti acts as an adhesive layer and was deposited by DC sputter in Ar with a flow rate of 150 sccm at a chamber pressure of 20 mTorr and sputtering power of 50 W for 10 minutes. Ir is a barrier layer to protect a diffusion of oxygen into Ti from SIROF and deposited by pulsed DC sputter in Ar with a flow rate of 100 sccm and at the power of 100 W and the pressure of 10 mTorr for 10 minutes. SIROF film was deposited as same condition described above. Annealing (Lindberg Annealing Furnace) was performed for 45 minutes under the forming gas flow of 2.5 slpm to improve the adhesion and form Ohmic contact between the deposited films and substrate. The dimensions of the analyzed samples were 1 cm \times 1 cm square. Chemical and elemental analysis of the deinsulated spots was performed using XPS (Kratos Axis Ultra DLD) to

examine the reduced SIROF. The monochromatic X-ray source, Al $K\alpha$, was used and the beam spot size was $110 \times 110 \mu\text{m}^2$ for a small scan region.

Planar test electrodes were prepared on heavily doped p-type Si wafer ($\rho = 0.01 \sim 0.05 \Omega\text{-cm}$) to investigate the electrochemical performance. Ti (100nm) / SIROF (700nm) and Ti (100 nm) / Ir (80 nm) / SIROF (700 nm) on doped Si wafer were deposited using a sputter system the same as above. LOR 7B (MicroChem) and positive photoresist (Shipley Microposit S-1813) were used to pattern the metal films by a lift-off technique [14]. Parylene film (6 μm) was deposited by chemical vapor deposition using a Paractech 3000 Labtop deposition system. To improve the chemical adhesion between the Parylene and the underneath film, 0.5% Silquest A-174 silane was used. The Parylene film was removed from the active area by the KrF laser system (Optec MicroMaster Excimer Laser) having a wavelength of 248 nm [15]. Utah electrode arrays were fabricated using a particular metallization of Ti (100 nm) / Ir (100 nm) / SIROF (700 nm) structure and Parylene insulator material was removed by laser as used in the planar test electrode. The fabrication process of the UEAs and laser deinsulation technique are described in detail elsewhere [7, 16, 17].

The electrochemical impedance spectroscopy (EIS), cyclic voltammetry (CV), and potential transient analysis were performed in a phosphate buffered saline (PBS) solution at a pH of 7.4 to determine the impedance, cathodal charge storage capacity (CSC_c), and charge injection capacity (CIC). The CSC_c was calculated from the time integral of the cathodic current in a cyclic voltammetry for a water window range of potential (-0.6 ~ 0.9 V) versus Ag|AgCl and the CIC was calculated by multiplying stimulation current and pulse width at which the maximum negative polarization reaches

water reduction potential. The EIS and CV were acquired using a commercial electrochemical test system (Gamry Instruments) and potential transient analysis was done with a STG 2008 stimulus generator (Multi-Channel Systems MCS GmbH) and recorded with an oscilloscope. More details of electrochemical measurements are given elsewhere [18, 19].

6.4 Results and Discussion

Figure 6.1 shows the TGA of IrO_x by nitrogen and forming gas. The weight loss is 14.2 % and 15.3 % for nitrogen and forming gas, respectively. Theoretical loss is $\sim 14.3\%$ for O_2 reduction of IrO_2 and it highly matches to the loss values from TGA. Oxygen desorption starts at 893 °C for nitrogen; however, it starts at 180 °C for forming gas. H_2 in forming gas is regarded as the factor to accelerate the reduction of oxygen from IrO_x .

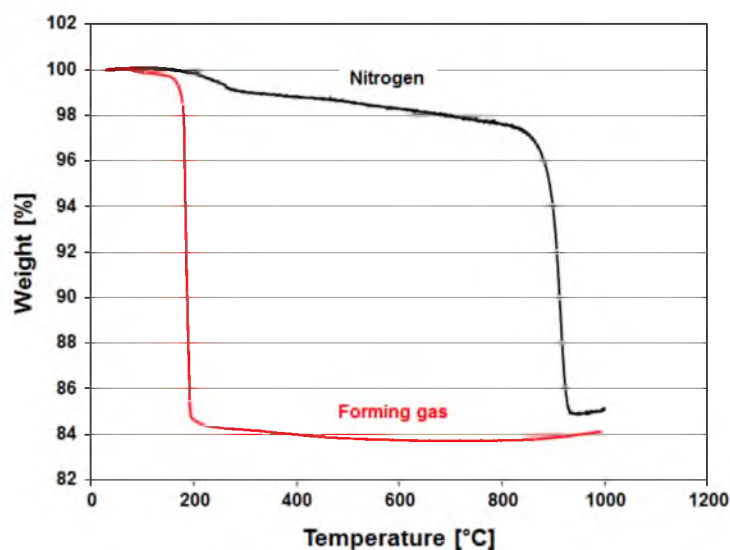


Fig. 6.1. TGA of IrO_x by nitrogen and forming gas.

Figure 6.2 shows the XRD of as-deposited SIROF (left) and annealed SIROF (right) according to four different annealing temperatures (410, 310, 220 and 210 °C). An IrO₂ (101) peak was prominent and Ir (111) appeared in the as-deposited SIROF, as shown in Figure 6.2 (a). However, the IrO_x peaks disappeared and only metallic Ir peaks were detected, as presented in Figure 6.2 (b). When the annealing temperature was 410 °C, which is close to the conventional annealing temperature in UEA process [7], the intensity of the Ir (111) peak was highest but it decreased when lowering annealing temperature to 210 °C. This suggests the amount of oxygen reduction in SIROF is more as the annealing temperature is higher. There was no deoxidization when the temperature was below 210 °C.

Figure 6.3 is SEM images (upper) and AFM images (bottom) of (a) as-deposited SIROF, (b) annealed SIROF, and (c) laser ablated annealed SIROF. The film was annealed at 410 °C, and illuminated by laser for $\sim 1.6 \text{ J/cm}^2$ and 100 pulses. The morphology is dendritic in as-deposited SIROF, as shown in Figure 6.3 (a); however, it is changed to a granular after annealing and laser ablation on the surface, as in Figure 6.3 (b) and (c). The root mean square roughness (R_{rms}) of as-deposited SIROF is 24 nm. However, it becomes 62 nm after annealing and 65 nm after laser ablation. The surface of the SIROF is smoother through heat treatment by laser energy, as shown in Figure 6.3 (c) [7].

Figure 6.4 is mechanically scratched Ti/SIROF films on silicon substrate after annealing at 410 °C in forming gas. The regions of three colors, blue (1), silver (2), and dark gray (3), were disclosed after the scratch, as shown in Figure 6.4 (a). Imaging XPS data were taken at the binding energy of the Ir 4f peak (60.3 eV) for the scratched sample,

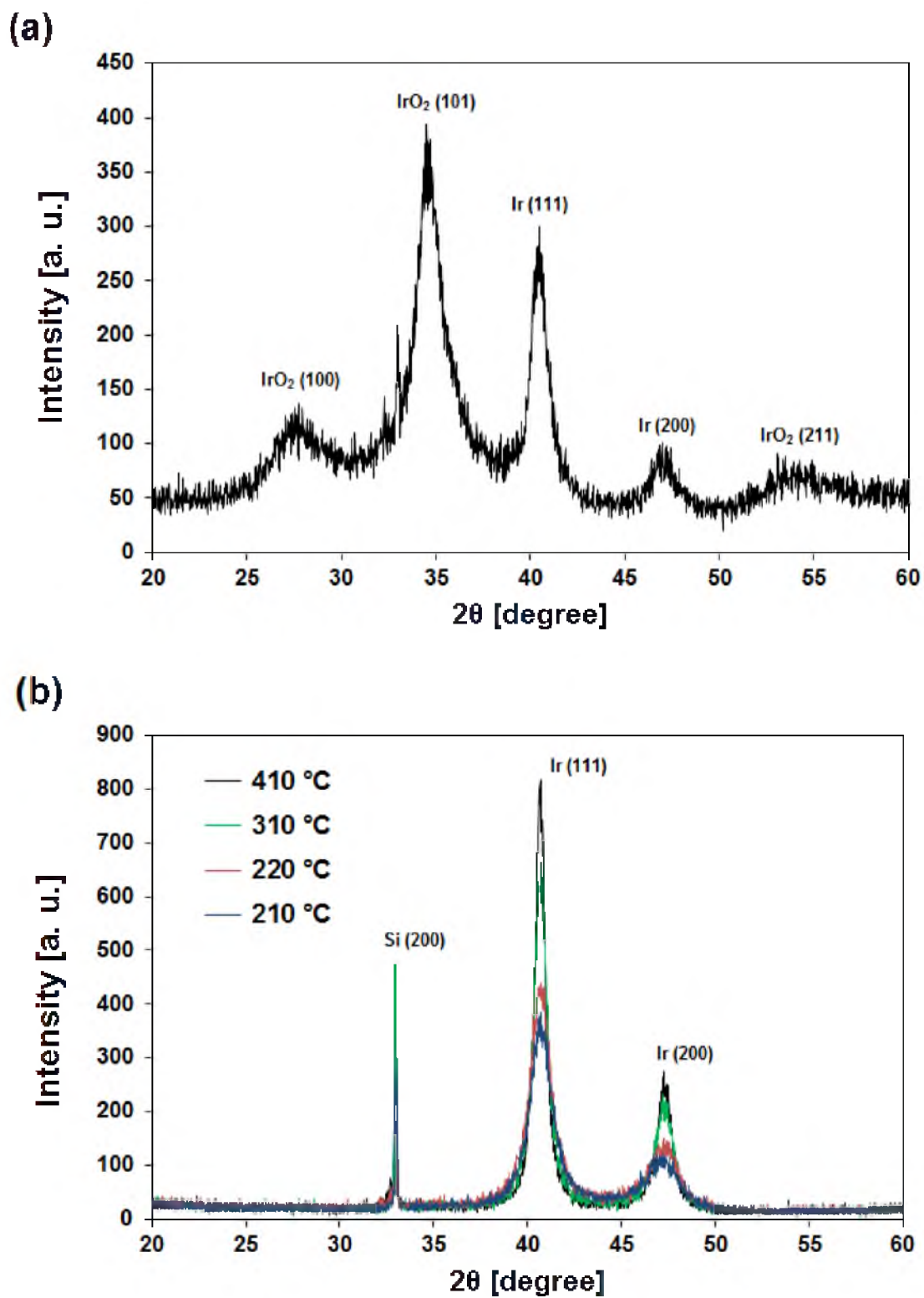


Fig. 6.2. XRD spectra of (a) as-deposited SIROF and (b) annealed SIROF according to four different temperatures (410, 310, 220, and 210 °C).

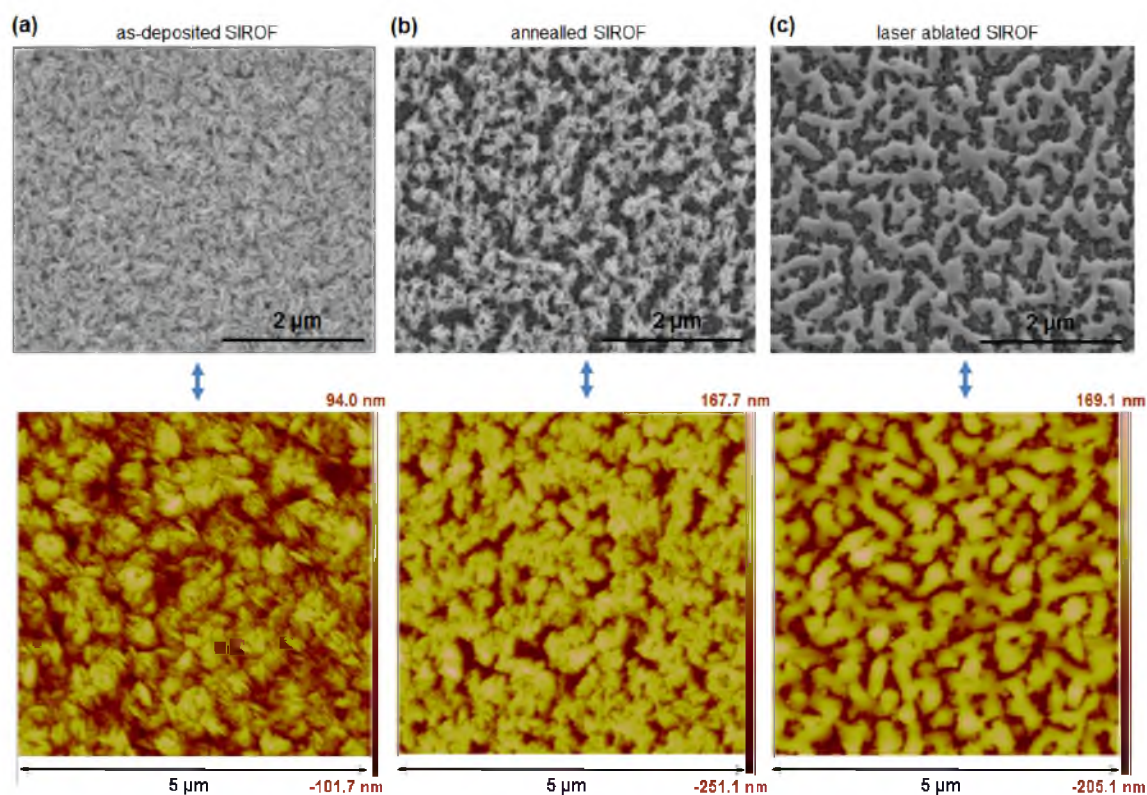


Fig. 6.3. SEM images (upper) and AFM images (bottom) of (a) as-deposited SIROF, (b) annealed SIROF, and (c) laser ablated annealed SIROF.

as presented in figure 6.4 (b). The scratched region is well matched between both figures. The SIROF film was removed by the scratch as dark imaging spots (1). Spot (2) is brighter than (3) which means there is more Ir concentration in (2). Figure 6.5 is XPS of (a) spots (1), (b) spots (2), and (c) spots (3) in Figure 6.4. The atomic concentration of Ti 2p and O 1s was 26.8 % and 45.4 %. The broad peaks are regarded as the two convoluted peaks of Ti and Ti in TiO_2 , which reflects the metallic titanium oxide, as illustrated in Figure 6.5 (a). Figure 6.5 (b) and (c) show the pure Ir peaks scanned from spots (2) and (3), respectively. The XPS of the silver region having pure Ir in Figure 6.4 would be evidence of reduced SIROF by a diffusion of oxygen from SIROF to Ti, as presented in Figure 6.5

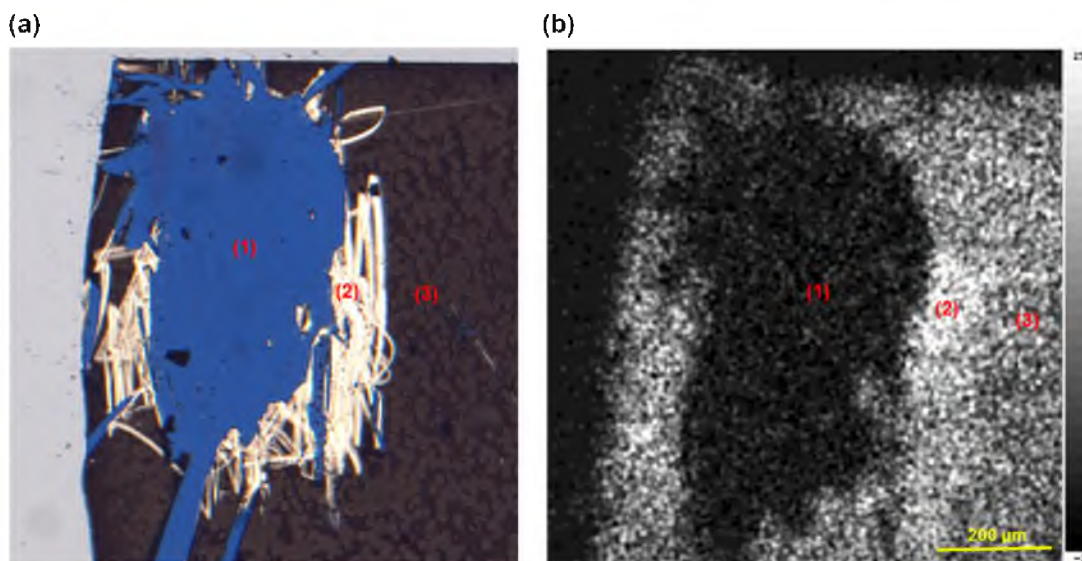


Fig. 6.4. Optical image of Ti/SIROF films on Si substrate after mechanically scratching is presented in (a). Three colors were disclosed as blue (1), silver (2) and dark gray (3). (b) is the imaging XPS for Ir 4f peak of the sample same to Figure 6.4 (a). Spots (1), (2) and (3) in Figure 6.4 (b) match to the numbers in Figure 6.4 (a).

(b). The XPS of the dark gray region as presented in Figure 6.5 (c) is regarded as deoxidized SIROF by annealing in forming gas.

The backscattered SEM image of a laser deinsulated hole with 300 μm diameter and the electrochemical analysis of planar electrodes are presented in Figure 6.6. The planar electrodes structured with Ti/Ir/SIROF annealed at 210 $^{\circ}\text{C}$ and insulated Parylene were exposed to 100 laser pulses with the fluence of 1.6 J/cm^2 and treated by a reactive ion etching (RIE) using an inductively coupled oxygen plasma for 2 minutes [15]. The 2-minute RIE decreases the carbon residue redeposited around the exposed area. There was no damage of films by the laser for all planar electrodes that have deoxidized SIROFs by annealing. The impedances of planar electrodes with different film stacks at particular annealing temperatures, Ti/SIROF at 410 $^{\circ}\text{C}$, Ti/Ir/SIROF at 410 $^{\circ}\text{C}$, and Ti/Ir/SIROF at 210 $^{\circ}\text{C}$, were quite a similar level at 1 kHz as 1.6, 1.4, and 1.5 $\text{k}\Omega$, respectively, but they

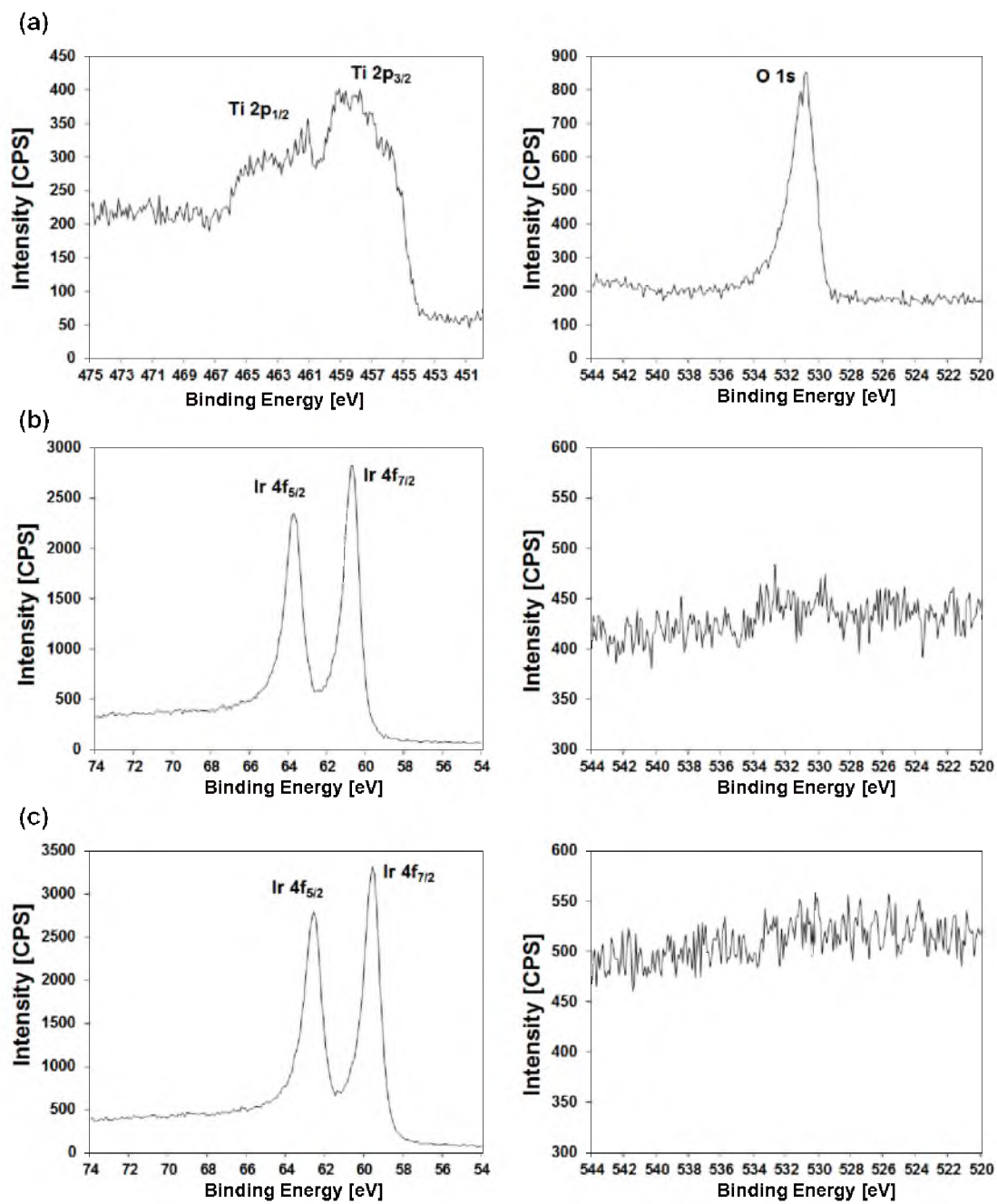
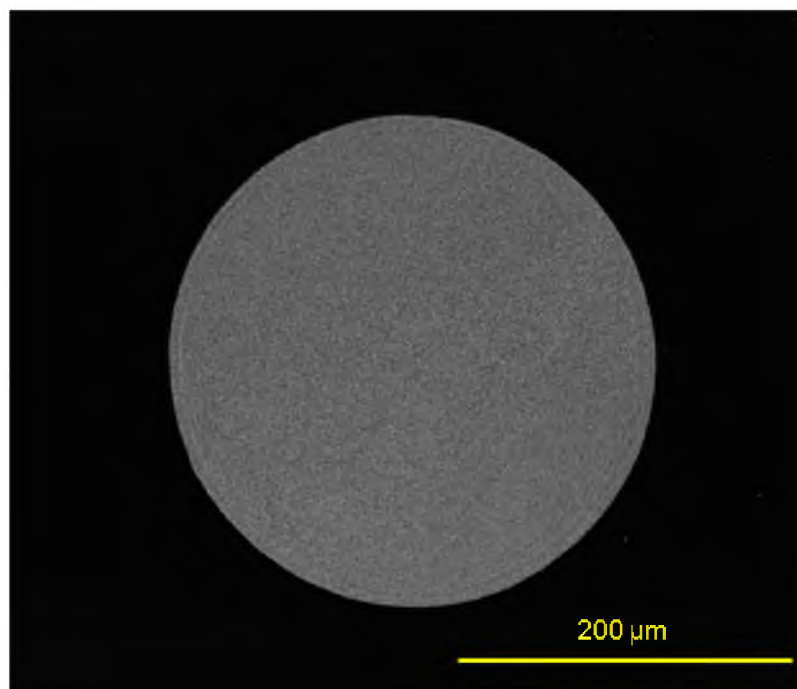


Fig. 6.5. X-ray photoemission spectra of (a) spots (1), (b) spots (2), and (c) spots (3) in Figure 6.4.

(a)



(b)

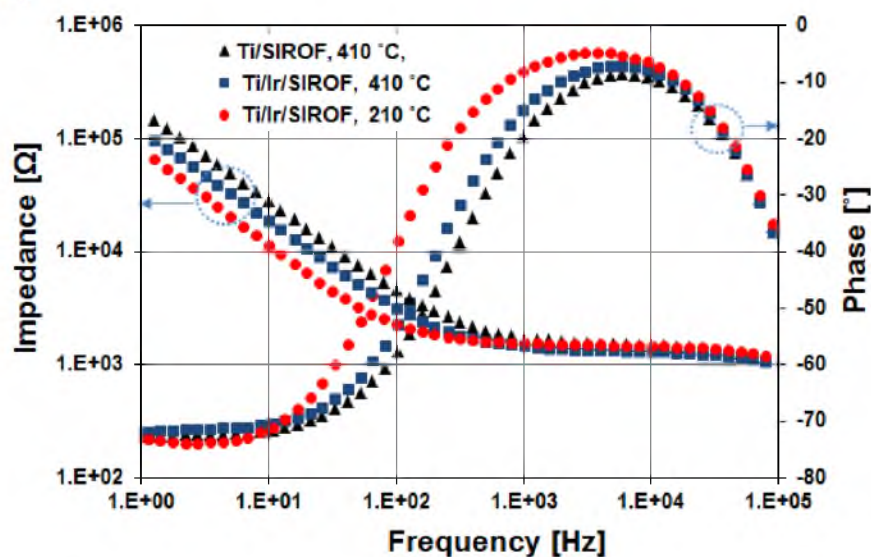


Fig. 6.6. Electrochemical analysis of planar electrodes is presented by (a) backscattered SEM image of laser deinsulated hole with $300\ \mu\text{m}$ diameter, (b) Bode plot of different film stacks at particular annealing temperature (Ti/SIROF at $410\ ^\circ\text{C}$, Ti/Ir/SIROF at $410\ ^\circ\text{C}$ and Ti/Ir/SIROF at $210\ ^\circ\text{C}$), (c) cyclic voltammograms of the same samples as (b), and (d) potential transient of two different structures (Ti/Ir/SIROF at $210\ ^\circ\text{C}$ and Ti/SIROF at $410\ ^\circ\text{C}$).

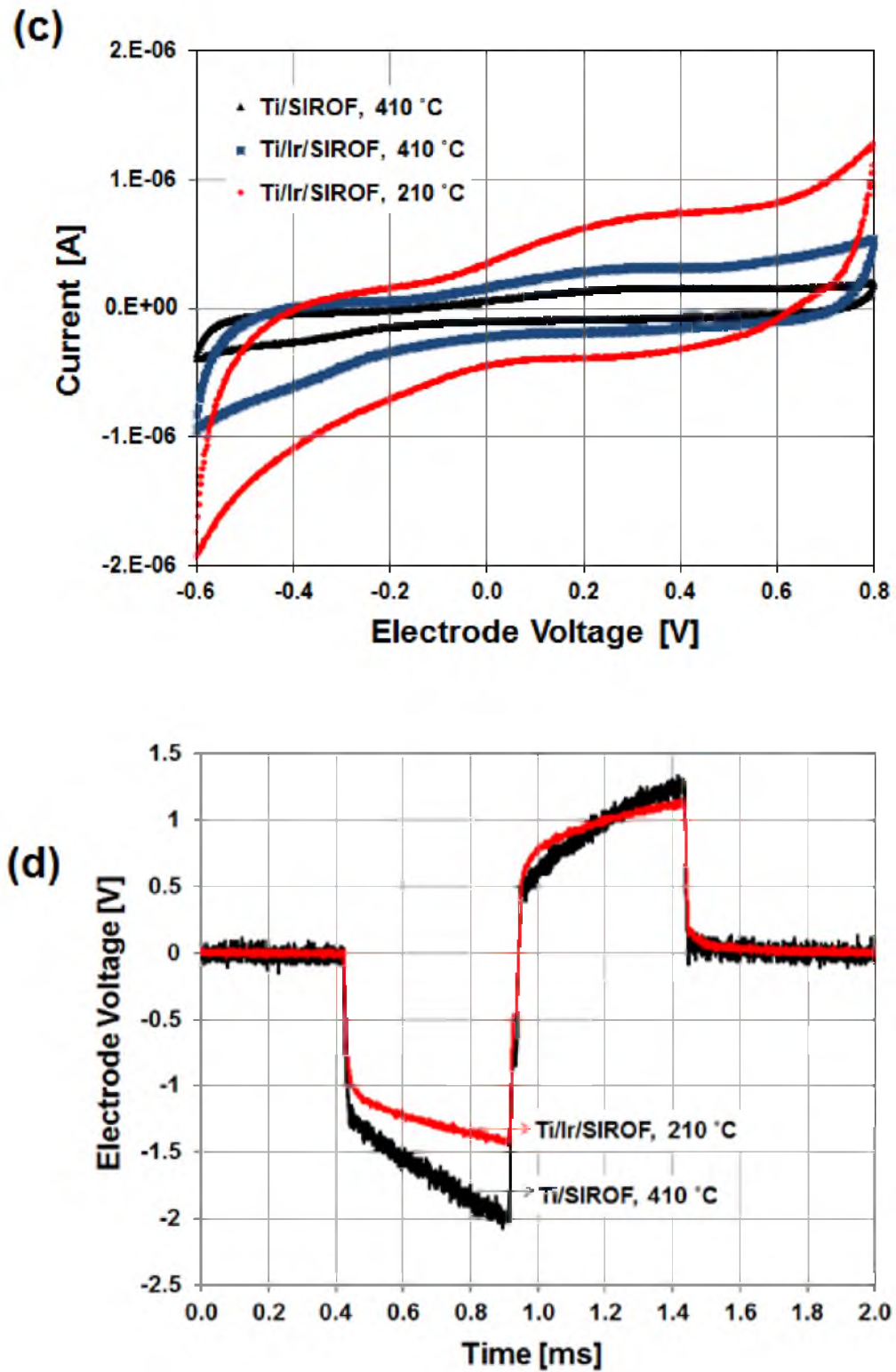


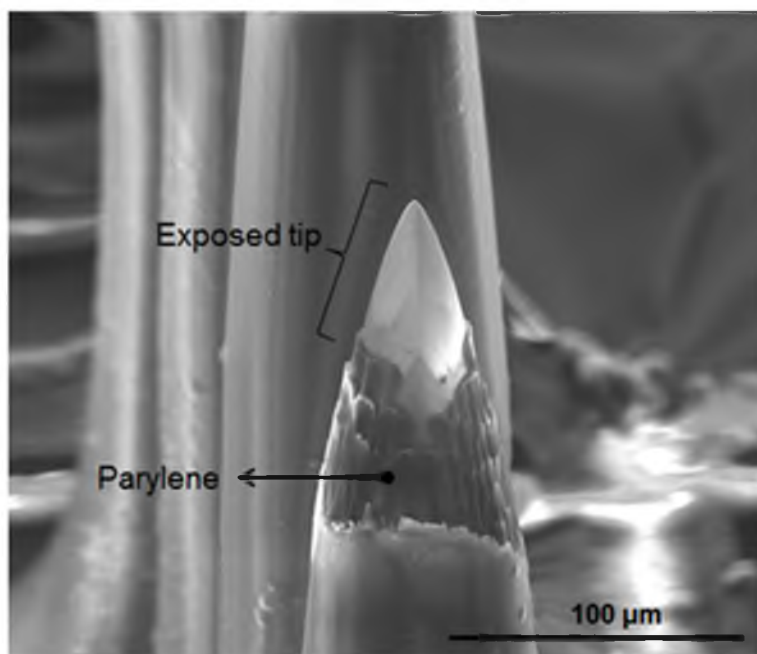
Fig. 6.6. Continued

were different impedances, 4.6, 3.2, and 2.3 k Ω , respectively, at 100 Hz and capacitive behavior for the frequency range from 1 to 500 Hz, as shown in Figure 6.6 (b). The impedances converged at a frequency range over 500 Hz, indicating the effect of PBS impedance. Cyclic voltammograms were measured in PBS, and no well-defined reduction and oxidation peaks are shown in Figure 6.6 (C), though the charge is Faradaic involving the reversible Ir³⁺/Ir⁴⁺ couple, as reported elsewhere [19]. The CV curve of Ti/Ir/SIROF annealed at 210 °C has a significantly larger internal area than that of Ti/SIROF annealed at 410 °C, or Ti/Ir/SIROF annealed at 410 °C, indicating the first sample has higher CSC than others. CSC_c measured from CV is a quantity of charge available at near equilibrium condition. The CSC_c was 5.8 mC/cm² for Ti/SIROF structure annealed at 410 °C; on the other hand, it was 12.6 mC/cm² and 24.8 mC/cm² for Ti/Ir/SIROF annealed at 410 °C and Ti/Ir/SIROF annealed at 210 °C, respectively. There are two factors that influence the charge storage performance according to CSC_c values. Ir that is deposited between Ti and SIROF is as a barrier layer to protect a plasma oxidation of Ti during the process of sputter deposition or a diffusion of oxygen into Ti from SIROF due to its high oxidation property, based on XPS data. Annealing temperature also effects the capacity because the amount of Ir on the reduced SIROF is lower as the annealing temperature is lower, based on the XRD analysis. Charge injection capacity also follows this rule. Potential transients were measured to compare different electrode potentials with 800 μ A and 500 μ s biphasic current pulse, as illustrated in Figure 6.6 (d). The polarization across the electrode-electrolyte interface is lower in Ti/Ir/SIROF annealed at 210 °C (\sim 0.4 V) than Ti/SIROF annealed at 410 °C (\sim 0.7 V). It

means that the charge injection required to deliver a stimulation pulse is higher in the first sample than the second sample. CIC derived from potential transient has practical importance compared with CSC due to its measure with high-frequency stimulation pulses with high current density. The values were 0.6, 0.9, and 1.4 mC/cm^2 for the electrodes of Ti/SIROF annealed at 410 °C, Ti/Ir/SIROF annealed at 410 °C, and Ti/Ir/SIROF annealed at 210 °C, respectively. The last sample has the highest capacity of charge injection which is consistent with the CSC analysis.

Figure 6.7 (a) shows the SEM image of a laser deinsulated UEA tip using 1.6 J/cm^2 fluence and 120 pulses which has the Ti/Ir/SIROF film structure annealed at 210 °C, as used in the planar electrode. The electrode was highly resistant against damage by the laser and showed a distinctive boundary line between the exposure area and Parylene, though there was uneven removal of Parylene by nonuniform laser power. Figure 6.7 (b), (c), and (d) show the impedance, CSC_c , and CIC values of UEAs with Ti/Ir/SIROF film structure annealed at 210 °C as a function of their tip exposure fabricated by the laser deinsulation and 2-minute RIE etching. The solid lines are a trend line with the equations, $y = 0.0817e^{-0.028x}$, $y = 91.525e^{-0.019x}$, and $y = 1.0246e^{-0.005x}$ for Figure (b), (c), and (d), respectively. The electrode impedance values were below 0.1 $\text{M}\Omega$ for tip exposures of $\sim 10 \mu\text{m}$ and approaches $\sim 2 \text{k}\Omega$ as the tip exposures were increased beyond $\sim 100 \mu\text{m}$. CSC_c which was measured with a slow-sweep rate (50 mV/s) cyclic voltammogram has higher R^2 values (0.86) than that of impedance at 1 kHz (0.58) or CIC (0.33) which suggests high-frequency current/voltage pulses employed for neural stimulation result in more deviation of measured values. It is regarded that the limited diffusion rate of charge carriers, and the nonuniform geometry and deinsulated area of each electrode tips affects

(a)



(b)

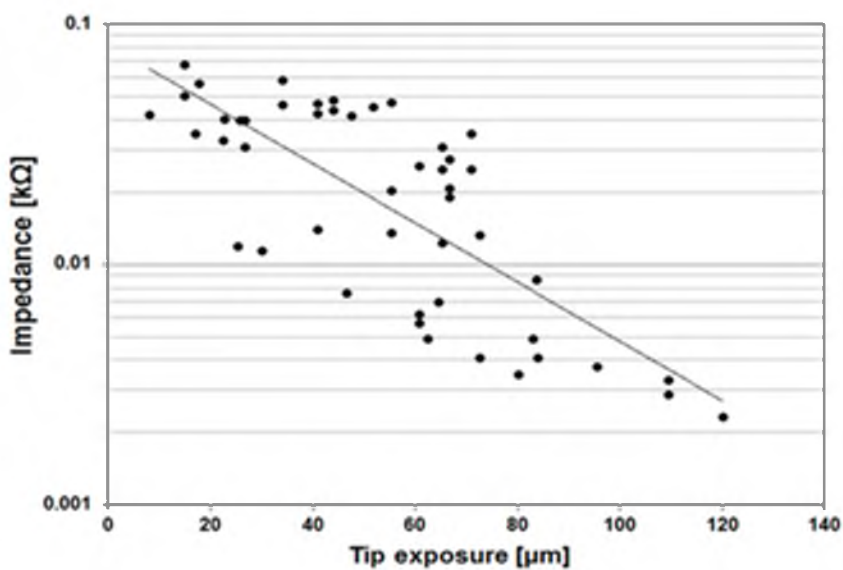
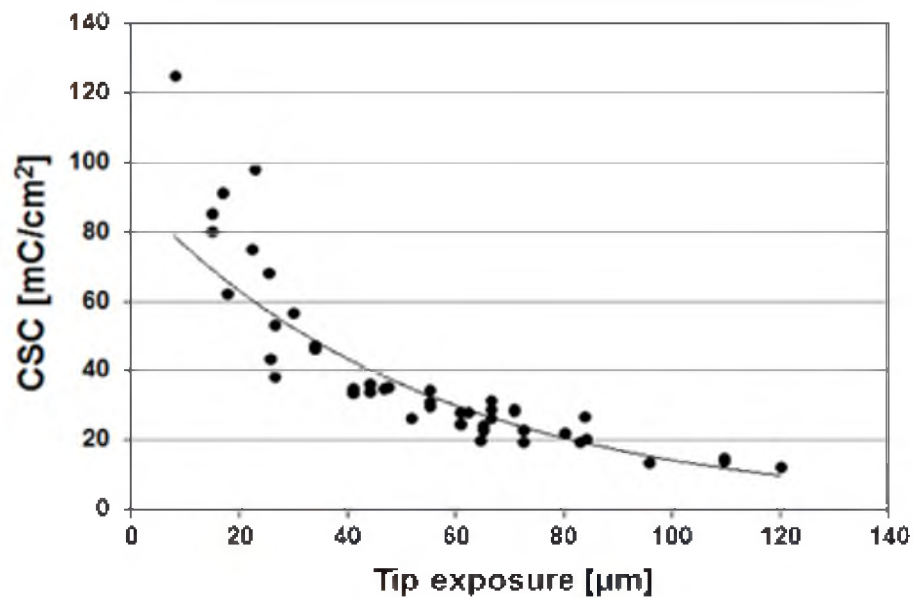


Fig. 6.7. Electrochemical analysis of 3D UEA tip is presented by (a) SEM image of laser deinsulated Utah electrode array tip, and (b) impedance, (c) CSC_c and (d) CIC values of UEAs with Ti/Ir/SIROF film structure annealed at 210 °C as a function of their tip exposure fabricated by the laser deinsulation. The solid lines are a trend line with the equations, $y = 0.0817e^{-0.028x}$, $y = 91.525e^{-0.019x}$ and $y = 1.0246e^{-0.005x}$ for Figure (b), (c), and (d), respectively.

(c)



(d)

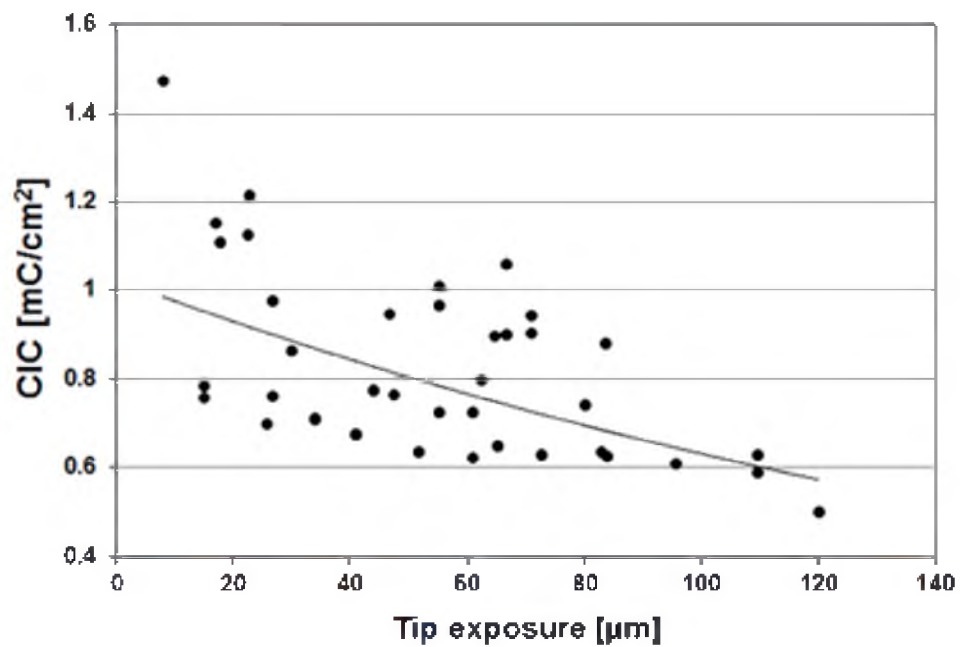


Fig. 6.7. Continued

the variation [18]. The CSC_c and CIC values decreased as the tip exposure increased, which is due to larger potentials by the edge and the tip of the exposed area in a smaller size of electrodes. Measured values are available to neural stimulation and recording application, although the deviation of impedances and CIC values from the trend line is rather high.

6.5 Conclusions

We have demonstrated partially deoxidized iridium oxide film for laser deinsulation of UEAs. The reduced film has a high electrochemical performance using lower anneal temperature to secure more remaining IrOx film. The Ir film as a diffusion barrier of oxygen from SIROF to Ti also contributes to keep it from a deterioration of film property. The results indicate that the laser ablation on partially deoxidized SIROF is suitable for deinsulation of UEAs.

6.6 References

- [1] R. A. Normann, "Technology Insight: future neuroprosthetic therapies for disorders of the nervous system," *Nat Clin Pract Neuro*, vol. 3, pp. 444-452, 2007.
- [2] K. Cheung, "Implantable microscale neural interfaces," *Biomedical Microdevices*, vol. 9, pp. 923-938, 2007.
- [3] G. E. Loeb, M. J. Bak, M. Salcman, and E. M. Schmidt, "Parylene as a Chronically Stable, Reproducible Microelectrode Insulator," *Biomedical Engineering, IEEE Transactions on*, vol. BME-24, pp. 121-128, 1977.
- [4] R. P. von Metzen, N. Lass, P. Ruther, and T. Stieglitz, "Diffusion-Limited Deposition of Parylene C," *Microelectromechanical Systems, Journal of*, vol. 20, pp. 239-250, 2011.
- [5] H. Jui-Mei, L. Rieth, R. A. Normann, P. Tathireddy, and F. Solzbacher, "Encapsulation of an Integrated Neural Interface Device With Parylene C," *Biomedical Engineering, IEEE Transactions on*, vol. 56, pp. 23-29, 2009.
- [6] E. M. Schmidt, M. J. Bak, and P. Christensen, "Laser exposure of Parylene-C insulated microelectrodes," *Journal of Neuroscience Methods*, vol. 62, pp. 89-92, 1995.
- [7] J.-M. Yoo, A. Sharma, P. Tathireddy, L. W. Rieth, F. Solzbacher, and J.-I. Song, "Excimer-laser deinsulation of Parylene-C coated Utah electrode array tips," *Sensors and Actuators B: Chemical*, vol. 166-167, pp. 777-786, 2012.
- [8] J.-M. Yoo, "KrF laser deinsulation method for AIROF coated Utah electrode array," *Journal of Neuroscience Methods*, 2013.
- [9] S. Y. CHA and H. C. LEE, "Deoxidization of Iridium Oxide Thin Film," *Japanese Journal of Applied Physics*, vol. 38, pp. L1128-L1130, 1999.
- [10] S. Y. KWEON, S. K. CHOI, W. S. YANG, S. J. YEOM, and J. S. ROH, "Thermal Stability and Electrical Properties of SrBi₂Ta_{2-x}Nb_xO₉/IrO_x Capacitors with Pt Top Electrode," *Japanese Journal of Applied Physics*, vol. 40, p. 5275, 2001.
- [11] Y. Sato, M. Yanagida, H. Yamanaka, and H. Tanigawa, "Reflectance and Structure Changes of Iridium Oxide Films by Reduction," *Journal of The Electrochemical Society*, vol. 136, pp. 863-866, 1989.
- [12] G. P. Burns, I. S. Baldwin, M. P. Hastings, and J. G. Wilkes, "The plasma oxidation of titanium thin films to form dielectric layers," *Journal of Applied Physics*, vol. 66, pp. 2320-2324, 1989.

- [13] G. Lutjering and J. J. C. Williams, *Titanium*: Springer, 2007.
- [14] S. Negi, R. Bhandari, L. Rieth, and F. Solzbacher, "Effect of sputtering pressure on pulsed-DC sputtered iridium oxide films," *Sensors and Actuators B: Chemical*, vol. 137, pp. 370-378, 2009.
- [15] J.-M. Yoo, J.-I. Song, P. Tathireddy, F. Solzbacher, and L. W. Rieth, "Hybrid laser and reactive ion etching of Parylene-C for deinsulation of a Utah electrode array," *Journal of Micromechanics and Microengineering*, vol. 22, p. 105036, 2012.
- [16] R. Bhandari, S. Negi, L. Rieth, and F. Solzbacher, "A wafer-scale etching technique for high aspect ratio implantable MEMS structures," *Sensors and Actuators A: Physical*, vol. 162, pp. 130-136, 2010.
- [17] P. K. Campbell, K. E. Jones, R. J. Huber, K. W. Horch, and R. A. Normann, "A silicon-based, three-dimensional neural interface: manufacturing processes for an intracortical electrode array," *Biomedical Engineering, IEEE Transactions on*, vol. 38, pp. 758-768, 1991.
- [18] S. F. Cogan, "Neural Stimulation and Recording Electrodes," *Annual Review of Biomedical Engineering*, vol. 10, pp. 275-309, 2008.
- [19] S. Negi, R. Bhandari, L. Rieth, and F. Solzbacher, "In vitro comparison of sputtered iridium oxide and platinum-coated neural implantable microelectrode arrays," *Biomedical Materials*, vol. 5, p. 015007, 2010.

CHAPTER 7

CONCLUSIONS AND FUTURE WORK

7.1 Conclusions and Contributions

The goal of the research described in this dissertation was to develop a laser deinsulation process of Parylene-C encapsulated Utah electrode arrays. The conventional deinsulation method [1] that uses dry etching (RIE) in an oxygen plasma has some limitations, such as large impedance variation ($\sigma > 0.5 \text{ M}\Omega$) in tip impedance, difficulty in controlling the tip exposure (especially for $< 40 \text{ }\mu\text{m}$), inability to deinsulate UEAs with complex geometries, and low throughput associated with Al foil poking and subsequent etching. Laser deinsulation demonstrated a smaller variation in tip impedance ($\sigma < 0.2 \text{ M}\Omega$) and well-controlled tip exposure ($\sigma < 0.3 \text{ }\mu\text{m}$), and the ability to deinsulate electrodes with different lengths.

There are several challenges for the laser ablation technique, such as a carbon residue remaining around the deinsulated site on UEA [2], and damage to the electrode material underneath the Parylene-C encapsulation [3, 4]. The problem of carbon debris was mitigated by using a hybrid deinsulation method that combines laser ablation and O_2 RIE. To decrease damage of the electrode material, laser deinsulation of Parylene-C from metallic iridium films, or reduced sub-oxide IrO_x films, were investigated. Also, the subsequent electrochemical activation of the iridium film was optimized to get low impedance and high charge injection activated iridium oxide film (AIROF) coatings.

Electrodes fabricated using this process showed a low tip impedance ($\sim 3 \text{ k}\Omega$ at 1 kHz) and high CSC ($\sim 15 \text{ mC/cm}^2$) for $60 \text{ }\mu\text{m}$ exposed tips. The partially deoxidized sputter deposited iridium film (SIROF) was devised and verified to achieve laser tip deinsulation with significantly less damage to the metallization. These electrodes had high electrochemical performance (median impedance $\sim 25 \text{ k}\Omega$, $\text{CSC}_c \sim 40 \text{ mC/cm}^2$, and $\text{CIC} \sim 0.8 \text{ mC/cm}^2$) for a $40 \text{ }\mu\text{m}$ exposed tip. A detailed description of the achievements from this work and the conclusions drawn are presented in following subsections.

7.1.1 Excimer-Laser Deinsulation of Parylene-C Coated Utah Electrode Array Tips

The use of laser deinsulation for Parylene coated planar and 3D microelectrodes was investigated by optimizing the laser parameters, such as fluence and number of pulses. The ablation threshold to etch Parylene was a fluence of $\sim 250 \text{ mJ/cm}^2$. The damage threshold of SIROF annealed at $375 \text{ }^\circ\text{C}$ in forming gas (98% Ar and 2% H_2) for 45 minutes was larger than 1000 mJ/cm^2 for the planar test structures. Especially, thicker SIROF films ($1.1 \text{ }\mu\text{m}$) showed higher resistance to damage (film fracturing) for the laser fluences of 1680 mJ/cm^2 . XPS analysis verified that the Parylene was removed, although there was carbon residue in the ablated area. After laser ablation, only the roughness of active electrode, SIROF, was changed without any chemical state alternation.

The laser deinsulation conditions developed with planar test structures were then applied to UEAs, with the complex 3D geometries and sharp electrode shanks. The removal of Parylene from electrode tips was uneven, which resulted from the spatial nonuniformity of laser power and the various oblique angles between the beam and the surface of the electrode tip. However, there was good repeatability for the open area of

the tips under the same deinsulation condition. There was a trade-off relation between laser fluence and number of pulses. With higher fluences, less number of pulses are needed for a specific exposure due to the higher ablation rate of parylene. The impedance values according to tip exposure of laser deinsulated UEA have a large variation ($\sigma > 0.5$ M Ω), so that the trend line was not highly matched to the data points because of the carbon redeposition on active tip surface after laser ablation. However, the electrode tip exposures larger than 100 μm had impedances of a few tens of k Ω , which is the normal target impedance value for neural interface applications. The benefits in achieving controlled deinsulation for electrodes suggested that the excimer laser ablation warranted addition research as a method to deinsulate UEAs.

7.1.2 Hybrid Laser and Reactive Ion Etching of Parylene-C for Deinsulation of a Utah Electrode Array

A hybrid method of etching Parylene-C using a combination of laser ablation and the O₂ RIE was investigated to decrease the electrode impedance and increase its charge injection by removing the carbonaceous residue. XPS analysis on the SIROF surface after the hybrid laser and O₂ RIE verified that the residual carbon produced by laser ablation of Parylene was significantly removed by subsequent O₂ RIE even for only a 1-minute etching.

In order to investigate the effects of the hybrid laser and plasma etching on the performance of electrodes with an especially small tip exposure for better selectivity, electrodes with two different tip exposures, 11 ~ 13 μm and 17 ~ 19 μm , were fabricated and characterized. The impedance value was a few M Ω immediately after laser ablation. After 1 minute of the oxygen plasma etching, the median impedance value of the two

electrode groups decreased from $\sim 4.6 \text{ M}\Omega$ to $\sim 0.7 \text{ M}\Omega$ and its standard deviation also decreased from $\sim 0.8 \text{ M}\Omega$ to $\sim 0.2 \text{ M}\Omega$. The median impedance value and its standard deviation saturated to $\sim 0.15 \text{ M}\Omega$ and $\sim 0.03 \text{ M}\Omega$ after 8 minutes etching time. The deviation of impedance values of Utah electrodes deinsulated by the hybrid method was significantly less than that of the values deinsulated by only laser.

7.1.3 Excimer Laser Deinsulation of Parylene-C on Iridium for Use in an Activated Iridium Oxide Film Coated Utah Electrode Array

The selection of submaterial underneath the Parylene-C encapsulation is critical for laser deinsulation because the high laser fluence can easily damage the submaterial during removal of the Parylene. The use of high laser fluences ($> 1.5 \text{ J/cm}^2$) is desirable because it reduces the redeposition of carbon by-products on the laser ablated region [5]. Consequently, a durable submaterial with high ablation threshold ($> 1.9 \text{ J/cm}^2$) allows less carbon debris with no damage. Iridium was chosen as the submaterial due to its excellent physical and mechanical properties, improving its stability to high laser irradiation.

The damage on sputter deposited iridium and iridium oxide films (as-deposited) according to different laser power was investigated and verified by SEM analysis. The iridium was not significantly damaged by laser irradiation, using conditions where relatively low carbon residue was observed. The laser deinsulation was then implemented to deinsulate Parylene coated metallic iridium films on silicon substrates. The deinsulated Ir then was activated by electrochemical activation (AIROF). A degree of damage of AIROF during activation process was investigated by varying the cathodic activation voltage (from - 0.8 to - 0.95 V) with fixing the anodic voltage of 0.95 V versus Ag|AgCl.

When the cathodic voltage was - 0.8 V, there was no degradation of film. However, a crack of iridium oxide started to appear at the cathodic voltage of - 0.85 V. The degradation including the crack and delamination of film was becoming severe for more negative cathodic voltage. The AIROF activated using pulse levels of - 0.8 and 0.95 V had a stable film morphology.

When using higher fluence with less pulses (1500 mJ/cm² fluence, 100 pulses) on iridium, the boundary line between exposure area and Parylene was distinctive in laser deinsulated UEA. On the other hand, lower fluence with more pulses on SIROF active electrode film (700 mJ/cm², 500 pulses) had insufficient Parylene etching on the sidewall of tip and the boundary was not clear. This causes the nonuniform exposure in the deinsulated area, and results in impedance variations between electrode tips. In this regard, the laser ablation of Parylene-C on iridium films was performed using high fluence with less number of pulses to decrease carbon residue and achieve complete removal of Parylene on the sidewall of the electrode tip. The median impedance of the AIROF UEA tip was ~ 3 k Ω for 60 μ m exposure. The CSC_c calculated by CV was ~ 16 mC/cm² which agrees well with values in the literature [6], and indicates good deinsulation performance.

7.1.4 Reduction of Iridium Oxide Films for Laser Deinsulation of Utah Electrode Array

As-deposited sputtered iridium oxide films (SIROF) are easily damaged by high laser fluences (> 1 J/cm²). Though use of low laser fluence for deinsulation can prevent film damage, it can cause a nonuniform exposure of the electrode tip and potential biocompatibility problems by the carbon residue redeposited around the exposed area.

The poor mechanical properties of as-deposited SIROF are an obstacle to the direct use of laser ablation for this electrode material. A process to partially reduce the IrO_x layer in a Ti/Ir/IrO_x (adhesion/diffusion barrier/electrode material) was developed, as the partially reduced IrO_x could tolerate significantly more laser irradiation. The ablation threshold of reduced SIROF ($> 1500 \text{ mJ/cm}^2$) was much higher than that of as-deposited SIROF ($< 700 \text{ mJ/cm}^2$).

In the thermogravimetric analysis (TGA) of SIROF, reduction started at 893 °C in a pure nitrogen atmosphere. In a forming gas atmosphere, a dramatically lower temperature of 180 °C was found to cause reduction of the deposited SIROF. X-ray diffraction analysis (XRD) of SIROF after annealing with forming gas verified that the amount of oxygen reduction in SIROF increased as annealing temperature increased, and there was no deoxidization when the temperature was below 210 °C. The reduced SIROF provided a fracture resistance to laser power. However, less reduction by lower anneal temperature ($\sim 220 \text{ }^\circ\text{C}$) was desirable for a high electrochemical performance because it secured more remaining IrO_x film. XPS analysis verified that there was an oxygen diffusion from SIROF to Ti during the annealing process. The Ir diffusion barrier between SIROF to Ti layers prevents the reduction of IrO_x through consumption of oxygen from this film by the Ti adhesion, which has a dramatically higher affinity for oxygen. The electrode showed high electrochemical performance with median $\sim 25 \text{ k}\Omega$ impedance, $\sim 40 \text{ mC/cm}^2 \text{ CSC}_c$, and $\sim 0.8 \text{ mC/cm}^2 \text{ CIC}$ for 40 μm exposed tips. These results suggest that the laser ablation on partially deoxidized SIROF with a diffusion barrier Ir was suitable for deinsulation of UEAs.

7.1.5. Contributions

This dissertation makes contributions in several areas:

- Chapter 3 of the dissertation has contributed to achieve the laser ablation process to deinsulate the 3D tips of Parylene encapsulated Utah electrode arrays (UEAs). Using a prototyping technique in laser deinsulation presented, one can easily implement the method to remove encapsulation polymer at the tips on microelectrode arrays. Also, the labor, time, and cost required for tip deinsulation can be minimized.
- In Chapter 4, the critical issue of carbon debris in excimer laser ablation of Parylene was settled by a hybrid deinsulation method using a combination of laser ablation and O₂ RIE. Utah electrodes with fine tip exposures were developed by the hybrid deinsulation method to increase the selectivity for stimulating or recording a small population of neuron.
- In Chapter 5, an AIROF microelectrode array that resists damage from laser irradiation was developed through laser deinsulation of Parylene-C on iridium and subsequent activation of iridium film. That approach minimizes carbon residue and complete removal of Parylene on the sidewall of the electrode tip using high fluence ($> 1.5 \text{ J/cm}^2$) with less number of pulses to improve tip reproducibility.
- In Chapter 6, a partially deoxidized SIROF Utah electrode array was developed to acquire damage resistant films with good electrochemical performance (low impedance and high CIC). We are able to understand the thermodynamical and electrochemical characteristics of iridium oxide for its application to laser deinsulation.

7.2 Future Work

In this study, laser deinsulation processes for the UEA, and the resulting electrochemical properties of the electrodes relevant to stimulation and recording of neural signals were investigated. The laser tip deinsulation of UEA is highly recommended for future studies in several areas, such as the following:

1. The use of ultrashort pulsed laser (picosecond or femtosecond) to increase the ablation efficiency (higher etch rate) while minimizing heat damage to substrate. The very short laser pulses could provide the sample patterning of high precision and lower ablation threshold than the nanosecond laser used in this study [7]. These results could be beneficial to the general area of micromachining polymer materials.
2. Even if the laser deinsulated electrode tips look clean, the residue of carbon still remains around the ablation site. Investigating the use of a helium shield gas system could be useful to minimize the carbon debris during the laser ablation process. The effects of this residue on biocompatibility, tip impedance/CIC, and encapsulation lifetime also need to be elucidated.
3. The SIROF in this study is not pure iridium oxide but it contains a mixture of oxide, sub-oxide, and metallic phases as reported in [8]. Stimulation pulses within the water window can lead to further activation of iridium with subsequent “lift-off” of the activated film by too much stimulation. The effects of long-term *in-vivo* stimulation and recording and degradation of SIROF for chronic implantation application also need to be further studied.

4. The parameters of the activation of iridium for AIROF was based on the method reported in [9]. Among many parameters of the activation pulse signal for the growth of AIROF, including anodic/cathodic voltage, ramp-up rate, dwell time, and number of pulses, the cathodic voltage was analyzed in detail because it is one of the most critical parameters for tuning the film growth rate. However, the tuning of other parameters, such as using slow ramp-up rate instead of rectangular pulse needs to be investigated to decrease the delamination of AIROF.
5. Foreign body reactions are a limiting factor for long-term use of all chronically implanted microelectrodes and may well be exacerbated by residual degradation products that are less inert than the parent polymer. The tips in this study do look quite clean just after laser deinsulation and the electrochemical measurements offered acceptable values as neural interface, However, it would be useful to have data on the integrity of the insulation and tip exposure and impedance after penetrating membranes such as epineurium and dura mater as an *in-vivo* experiment. It would be even better to have some comparative recording data from neural tissue.
6. A charge injection material with capacitive coupling mechanism is ideal for neural stimulation because no chemical change occurs to either the tissue or the electrode. As an alternative to iridium oxide, there are various emerging materials, such as conducting polymers and carbon nanotubes (CNT), which have the capacitive charging mechanism. Conducting polymers, such as polyethylenedioxythiophene (PEDOT), cannot serve as a substrate for laser

deinsulation due to their soft mechanical property with the ablation threshold comparable to Parylene-C. CNTs are one of the candidates to replace the SIROF for the laser ablation technique due to its expected high ablation threshold with extraordinary mechanical (50 ~ 300 GPa of the tensile strength) and electrical properties ($\sim 5 \times 10^{-8} \Omega \cdot \text{m}$ of the electrical resistivity) for a multiwalled carbon nanotube (MWNT). CNTs are the one of the strongest and stiffest materials resulting from the covalent sp^2 bonds formed between the individual carbon atoms. The charge injection capacity of CNT is around 1-1.6 mC/cm^2 , far better than bare Pt and comparable to iridium oxide with a wide electrochemical operational window (2.5 V) [10, 11]. If several issues, for example, an adhesion problem or removal of catalytic seed material like Fe, can be solved, CNTs could be a strong candidate electrode material for electrode sites in Utah electrode array.

7.3 References

- [1] H. Jui-Mei, L. Rieth, R. A. Normann, P. Tathireddy, and F. Solzbacher, "Encapsulation of an Integrated Neural Interface Device With Parylene C," *Biomedical Engineering, IEEE Transactions on*, vol. 56, pp. 23-29, 2009.
- [2] J. D. Weiland, D. J. Anderson, C. C. Pogatchnik, and J. J. Boogaard, "Recessed electrodes formed by laser ablation of parylene coated, micromachined silicon probes," in *Engineering in Medicine and Biology Society, 1997. Proceedings of the 19th Annual International Conference of the IEEE*, vol.5, pp. 2273-2276, 1997.
- [3] Y. Terasawa, H. Tashiro, A. Uehara, T. Saitoh, M. Ozawa, T. Tokuda, *et al.*, "The development of a multichannel electrode array for retinal prostheses," *J Artif Organs*, vol. 9, pp. 263-6, 2006.
- [4] O. Musaev, P. Scott, J. Wrobel, J. Wolf, and M. Kruger, "UV laser ablation of parylene films from gold substrates," *Journal of Materials Science*, vol. 46, pp. 183-187, 2011.
- [5] K. Liu, Z. NiCkolov, J. Oh, and H. M. Noh, "KrF excimer laser micromachining of MEMS materials: characterization and applications," *Journal of Micromechanics and Microengineering*, vol. 22, p. 015012, 2012.
- [6] S. F. Cogan, "Neural Stimulation and Recording Electrodes," *Annual Review of Biomedical Engineering*, vol. 10, pp. 275-309, 2008.
- [7] A. A. Serafetinides, M. I. Makropoulou, C. D. Skordoulis, and A. K. Kar, "Ultra-short pulsed laser ablation of polymers," *Applied Surface Science*, vol. 180, pp. 42-56, 2001.
- [8] S. Negi, R. Bhandari, L. Rieth, and F. Solzbacher, "Effect of sputtering pressure on pulsed-DC sputtered iridium oxide films," *Sensors and Actuators B: Chemical*, vol. 137, pp. 370-378, 2009.
- [9] C. Yoonsu, O. C. Seong, R. H. Shafer, and M. G. Allen, "Highly inclined electrodeposited metal lines using an excimer laser patterning technique," in *Solid-State Sensors, Actuators and Microsystems, 2005. Digest of Technical Papers. TRANSDUCERS '05. The 13th International Conference on*, Vol. 2, pp. 1469-1472, 2005.
- [10] K. Wang, H. A. Fishman, H. Dai, and J. S. Harris, "Neural stimulation with a carbon nanotube microelectrode array," *Nano Lett*, vol. 6, pp. 2043-8, Sep 2006.
- [11] T. D. Nguyen-Vu, H. Chen, A. M. Cassell, R. J. Andrews, M. Meyyappan, and J. Li, "Vertically aligned carbon nanofiber architecture as a multifunctional 3-D neural electrical interface," *IEEE Trans Biomed Eng*, vol. 54, pp. 1121-8, Jun 2007.